MEASUREMENTS OF WHITE LINES IN TRANSITION METALS AND ALLOYS USING ELECTRON ENERGY LOSS SPECTROMETRY

Thesis by
Douglas Harvey Pearson

In Partial Fulfillment of the Requirements
for the Degree of
Doctor of Philosophy

California Institute of Technology
Pasadena, California
1992
(Defended September 30, 1991)

For Mom

Acknowledgements

It is a pleasure to thank the people who have contributed to my education.

First, I would like to thank my advisor, Professor Brent Fultz, for his guidance and support through my years at Caltech. His cheerful nature and enthusiasm for science provided a friendly and motivating atmosphere that greatly facilitated this work.

I would also like to thank Dr. Channing Ahn for generously sharing with me his expertise in electron microscopy and energy loss spectrometry.

In addition, my sincere thanks goes to Professor Gabriel Kojoian for inviting me to participate in his undergraduate research programs, and to Professor James Seal for his insightful answers to my questions in research and academics. Their guidance and encouragement through my undergraduate and graduate years have helped me immensely.

I would also like to thank Professor Peter Rez for providing a copy of the Hartree-Slater computer code used in this work and for many interesting discussions on the topic of energy loss near edge structure.

I am also grateful to Carol Garland for her technical assistance.

Most of all, I would like to thank my mother for everything. None of this would have been possible without her.

This work was supported by the United States Department of Energy under contract DE-FG03-86ER45270. The transmission electron microscopy facility was supported by the National Science Foundation under grant DMR-8811795. The Gatan 666 parallel EELS spectrometer was acquired through an equipment grant from Caltech's Program in Advanced Technologies, supported by Aerojet, General Motors, and TRW.

Abstract

This thesis addresses the interpretation of the peaks known as "white lines" found at the onsets of the L_2 and L_3 absorption spectra of 3*d* and 4*d* transition metals and alloys. These peaks arise from excitations of 2*p* core electrons to unoccupied outer *d* states at transition metal atoms. Recent work has suggested that differences in white line intensities observed between pure transition metals and associated compounds may be used to infer changes in the occupancies of the corresponding *d* states local to a given atom species. These prior studies, however, have focused on compounds of only a few transition metals. A systematic investigation of the relationship between white line intensity and *d*-state occupancy for 3*d* and 4*d* transition metals had not yet been done.

In this work an experimental analysis of the white lines for the 3*d* and 4*d* transition metals was carried out using electron energy loss spectrometry (EELS), and a linear decrease in white line intensity with increasing *d* state occupancy was found for both transition series. These results suggest that the intensities of the white lines reflect the occupancies of the outer *d* states in 3*d* and 4*d* transition metals, which are known to increase linearly with atomic number. In addition, these empirical correlations provide a straightforward method for measuring changes in 3*d* or 4*d* state occupancy.

In an application of this work, $L_{2,3}$ spectra were measured for a number of binary copper alloys, Fe-Co alloys of varying composition, and several binary nickel alloys. Significant changes in the intensities of the white lines were observed in some cases. Changes in 3*d* occupancies inferred from these measurements were in agreement with other measurements and density-of-states calculations from the literature where available.

Table of Contents

List of Figures

List of Tables

Chapter 1 Introduction

This chapter serves as an introduction to the thesis. In §1.1 a review of recent work on the interpretation of white lines in the L_2 and L_3 absorption spectra of transition metals is presented. In §1.2 a description of electron energy loss spectrometry (EELS) in the transmission electron microscope is presented. Further remarks and an outline of the remainder of the thesis are presented in §1.3.

1.1 White Lines in L_2 and L_3 Absorption Spectra

Some of the most distinctive features observed in the x-ray absorption spectra and electron energy loss spectra of transition metals are the peaks known as "white lines" found at the onsets of the L_2 and L_3 absorption edges. These peaks, which are quite intense for the early transition metals and diminish in intensity toward the right of each transition series, were first correctly interpreted by Mott (1949) as being due to excitations of $2p$ core electrons in an atom to unoccupied d-like states above the Fermi level. The peaks have been called white lines because they were originally observed as overexposed regions on the photographic film originally used to record x-ray absorption spectra (Veldkamp, 1935).

Absorption spectra may be measured using either electron energy loss spectrometry (EELS) or x-ray absorption spectrometry (XAS). In a typical energy loss experiment in a transmission electron microscope, one directs a monoenergetic beam of electrons through a specimen and subsequently analyzes their energy distribution. An incident electron that promotes an excitation in the sample must suffer an equal energy loss, and the recorded energy loss spectrum therefore displays peaks and edges corresponding to the various types of excitations.

As an example, the $L_{2,3}$ absorption edge for elemental nickel obtained with EELS is shown in Figure 1.1. A one-electron description for this excitation process is shown schematically in Figure 1.2. In the one-electron picture of the $L_{2,3}$ edge, an incident electron excites a $2p_{1/2}$ or a $2p_{3/2}$ core electron in an atom to an unoccupied state above the Fermi level. It is assumed that the presence of the resulting core hole has no effect on the other electrons in the atom. Because of spin-orbit splitting, the energy of the $2p_{3/2}$ electrons lies above that of the $2p_{1/2}$ electrons, and the associated L_3 edge therefore occurs at an energy loss lower than that of the L_2 edge.

Since the $2p$ core electrons are essentially atomiclike, the dipole selection rules (Gasiorowicz, 1974, for example) favor excitations to final states with s and d character. As illustrated in Figure 1.2, transition metals may possess a large density of d-like states above the Fermi level, yielding white lines of proportionate intensity. In addition, since the $2p$ electrons are atomiclike and the outer d states are rather tightly bound to a given atom, the intensities of the white lines are expected to reflect the unoccupied d-like density of states *local* to that atom species. Neglecting the white lines, the edge appears as somewhat of a step function due to the spin-orbit splitting of the initial $2p_{1/2}$ and $2p_{3/2}$ states. The relative heights of the steps reflect the 2:1 ratio of the numbers of initial states (four $2p_{3/2}$ electrons and two $2p_{1/2}$ electrons).

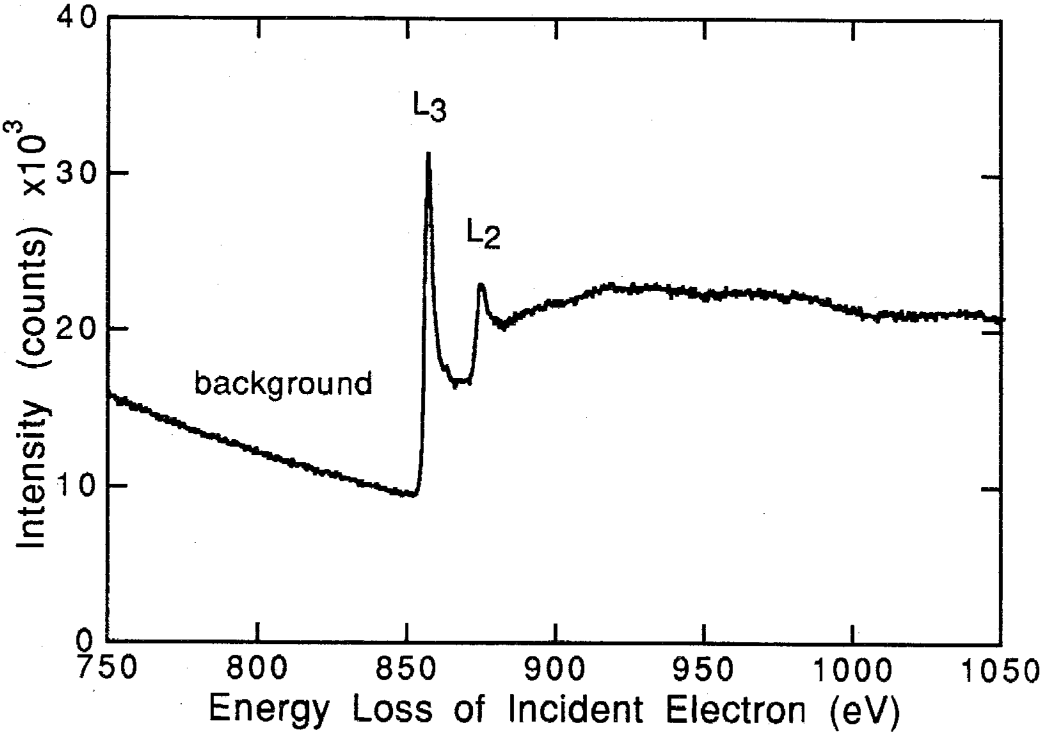

Figure 1.1. $L_{2,3}$ absorption edge for Ni metal obtained by EELS. White lines are found at the onsets of the L_3 and L_2 edges.

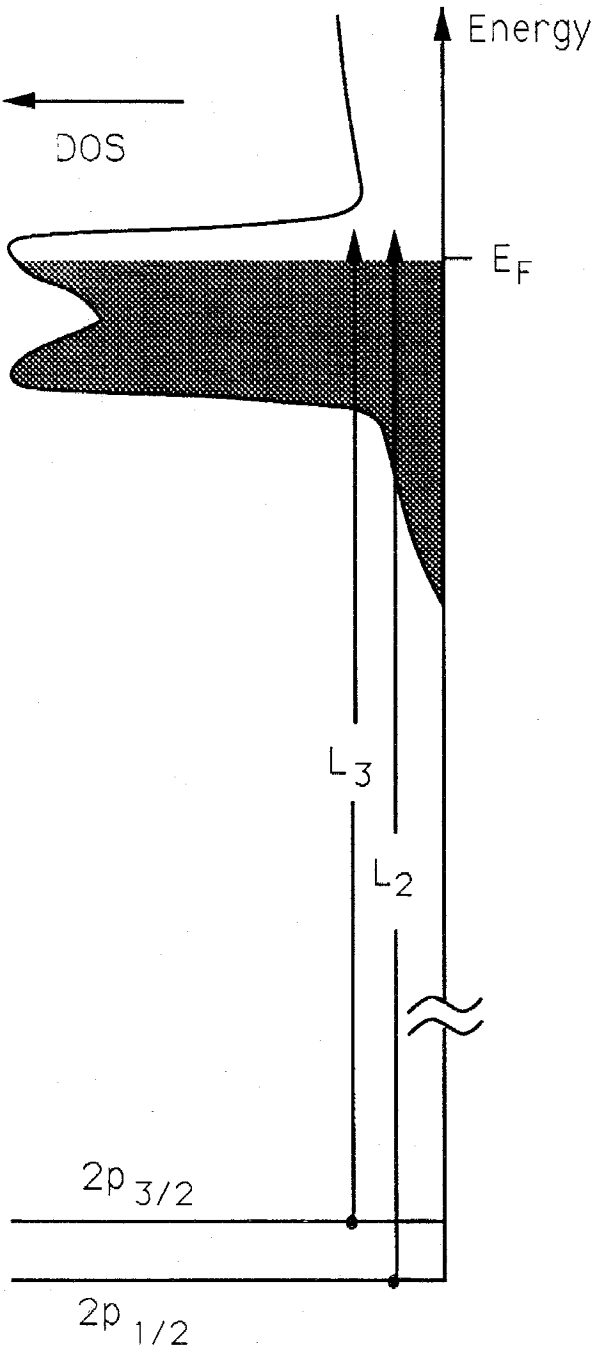

Figure 1.2. One-electron picture of the excitations that yield the L_3 and L_2 absorption edges.

A number of x-ray absorption studies based on the one-electron approximation have attempted to relate changes in white line intensities observed during compound formation to changes in the occupancies of the corresponding outer *d* states. Lytle et al. (1979) compared L_3 white line intensities for a number of iridium, platinum, and gold compounds with those of the respective pure metals and concluded that the differences in the white line intensities reflected changes in the occupancies of the local 5*d* states that were due to compound formation. In a similar study, Horsley (1982) compared the sum of the normalized L_3 and L_2 white line intensities observed in several platinum and iridium compounds with those observed in pure metals. The changes in the total normalized white line intensity were found to correlate with changes in the number of 5*d* holes determined from band structure calculations. Mansour et al. (1984) extended this work by establishing a proportionality between the total normalized white line intensity and the number of 5*d* holes from band structure calculations for pure platinum metal. He then used this proportionality to correlate changes in the total normalized white line intensity to changes in the number of 5*d* holes in a platinum catalyst. Using a similar approach, Sham (1985, 1987) and Sham et al. (1989) determined changes in the occupancies of the outer *d* states for a number of gold, palladium, and nickel compounds.

In other studies Brown et al. (1977) and Mattheiss and Dietz (1980) included spin-orbit splitting in tight-binding band structure calculations for platinum metal and found that the unoccupied 5*d* states were of the j=5/2 character. They concluded that the L_3 absorption edge should therefore show a white line, while the L_2 edge should not, since dipole selection rules require $2p_{3/2}$ electrons to couple to both $d_{5/2}$ and $d_{3/2}$ states, and $2p_{1/2}$ electrons to couple only to (filled) $d_{3/2}$ states. These predictions were largely consistent with experimental observations. In an application of this work, Morrison et al. (1985) used EELS to investigate the angular momentum character of the unoccupied 3*d* states local to Fe atoms in FeGe alloys. Pease et al. (1986) conducted a similar experimental study on the unoccupied 3*d* states local to Cr atoms in a CrAu alloy.

Other studies have focused on the ratio of the L_3 white line intensity to the L_2 white line intensity for the early 3*d* transition metals. As discussed by Thole and van der Laan (1987), a 2:1 ratio reflecting the relative numbers of initial states is expected since the spin-orbit splitting in the 3*d* band is small compared to the band width. Leapman and Grunes (1980), however, pointed out that the observed ratios did not follow the expected 2:1 value for the early 3*d* transition metals. Zaanen et al. (1985) showed that these anomalous ratios could be partially explained by atomic multiplet effects. Specifically, they showed that the multiplet structure of the excited atom may result in overlapping transitions from $2p_{1/2}$ and $2p_{3/2}$ states for the early 3*d* metals where the spin orbit splitting is small. Atomic multiconfigurational calculations of Waddington et al. (1986) agreed with these results, thus questioning the applicability of using L_3 and L_2 white lines to probe the total angular momentum character of the final 3*d* states for the early 3*d* transition metals. In addition, Stern and Rehr (1983) have questioned the general use of the one-electron approximation itself and have suggested that many-body effects under the influence of the core hole may be significant in interpreting the structure at absorption edges. They have shown, however, that the many-body problem reduces to a one-electron problem for transitions to an initially empty shell or for transitions that fill a shell.

This review of previous work suggests that there is evidence that the white lines of absorption spectra may be useful in obtaining information about the occupancy of the outer *d* states at transition metal atoms, but that the interpretation is not straightforward and is not completely understood. In spite of the considerable amount of previous work, an experimental study encompassing the pure metals of the 3*d* and 4*d* transition series to investigate systematically the relationship between white line intensity and *d*-state occupancy had not been undertaken. Such a study was the main thrust of this thesis. As the present work focuses on the analysis of absorption spectra obtained by EELS, a review of this technique is presented in the following section.

1.2 Transmission Electron Energy Loss Spectrometry (EELS)

Electron energy loss spectrometry (EELS) has evolved considerably since the early energy loss measurements of electrons reflected from the surfaces of copper and other metals by Rudberg (1930). Today, electron energy loss spectrometers are commonly attached to transmission electron microscopes and are used, for example, in chemical microanalysis, in determining radial distribution functions in solids through the analysis of extended energy loss fine structure (EXELFS), and in obtaining density of states information by interpreting the fine structure (near edge structure) found at absorption edges . More detailed information on these topics may be found in the recent books by Egerton (1986) and Disko et al. (1991). In addition, EELS has recently been used outside its conventional implementation for the *in-situ* characterization of semiconductor surfaces during growth by molecular-beam epitaxy (Atwater and Ahn, 1991).

A typical configuration of an EELS spectrometer attached to a TEM is shown schematically in Figure 1.3. A detailed description of EELS instrumentation used in this work will be given in Chapter 3. As shown in the diagram, an incident electron beam of well-defined energy, typically 100 keV to 300 keV, passes through a sample, through the imaging optics of the microscope, and into an energy loss spectrometer. Some of the incident electrons will pass through the sample unscattered, some will be elastically scattered, and some will be inelastically scattered (will suffer an energy loss). The spectrometer may be thought of as a "magnetic prism," which bends the electron beam via the Lorentz force, $\mathbf{F} = -e\, \mathbf{v} \times \mathbf{B}$, where $-e$ is the charge on the electron, $\mathbf{v}$ is its velocity, and $\mathbf{B}$ is the magnetic field. For $\mathbf{v}$ initially perpendicular to $\mathbf{B}$ as shown in Figure 1.4, electrons of a given energy follow a circular trajectory of radius R. Equating the Lorentz force to the centripetal force, $F = mv^2/R$, one finds that $R = eB/mv$. Thus, electrons with relatively lower velocities, hence lower kinetic energies, undergo larger deflections. The electrons are therefore spatially separated according to energy and may be counted with an appropriate detection system. If the detector is positioned to accept electrons that traverse roughly one fourth of the circular orbit, the spectrometer is called a 90° prism spectrometer.

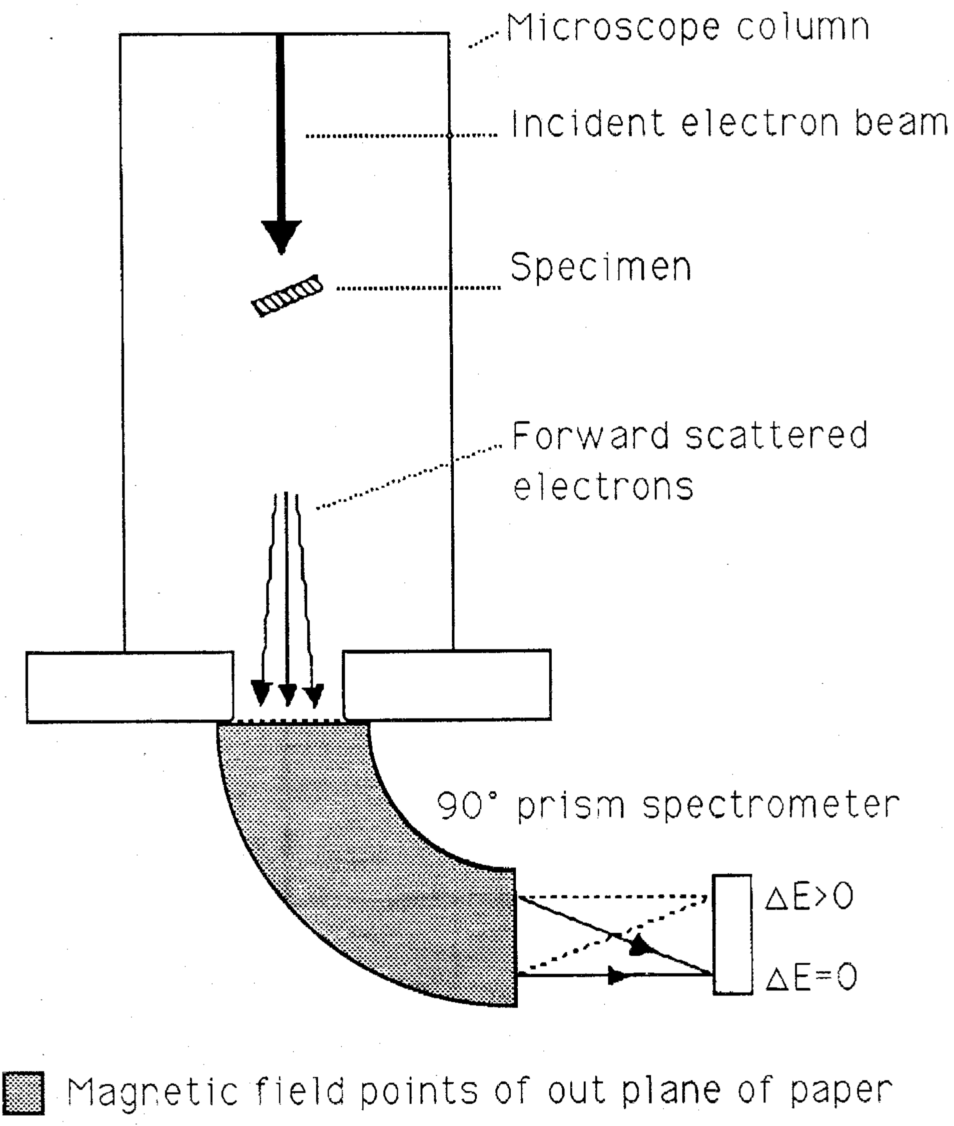

Figure 1.3. Schematic of an energy loss spectrometer attached to a transmission electron microscope.

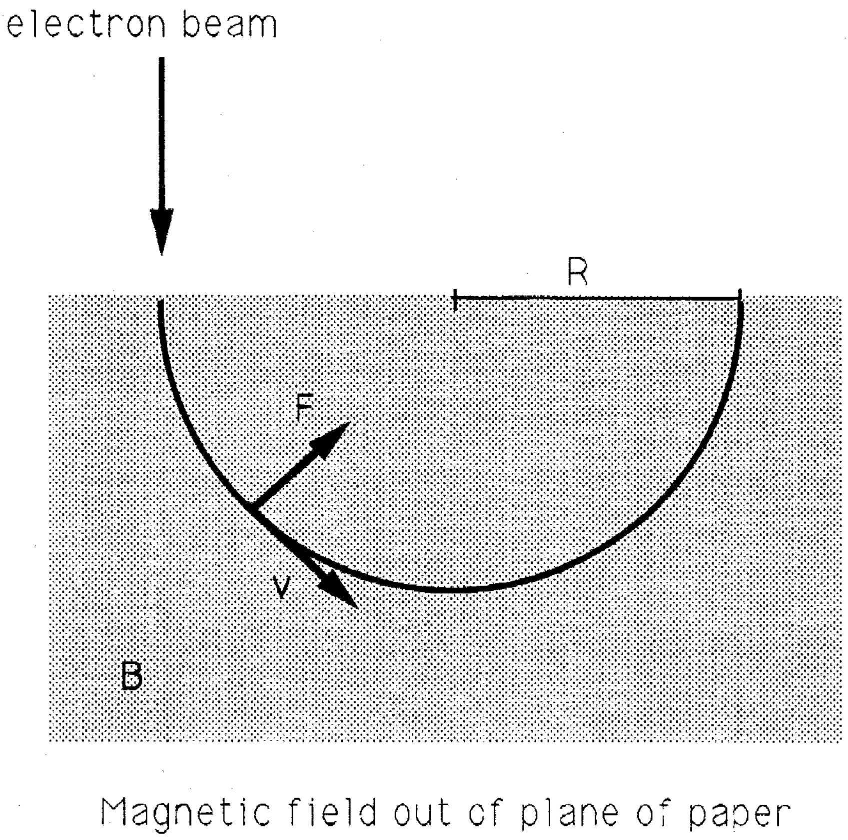

Figure 1.4. Trajectory of an electron passing through a constant magnetic field oriented perpendicular to its velocity.

To illustrate some of the features typical of energy loss spectra, consider the energy loss spectrum shown in Figure 1.5 obtained from a thin polycrystalline specimen of Ni metal. As the recorded intensity encompasses a wide dynamic range, a change in the detector sensitivity of approximately 1000 is used when acquiring spectra. This gain change is seen as an abrupt step in the spectrum, in this case, near an energy loss of 375 eV. The energy loss region from 0 eV to approximately 50 eV is commonly called the "low loss" region, and contains the most intense part of the spectrum. At zero energy loss, one finds the "zero loss" peak, with a full width at half maximum (FWHM) of perhaps a few eV or less, depending upon the energy distribution of the incident electron beam. This peak is associated with unscattered electrons, elastically scattered electrons, and phonon scattered electrons for which the corresponding energy losses are less than the instrumental resolution. Immediately following the zero loss peak is the portion of the low loss region dominated by excitations of plasmons (plasma oscillations) and excitations of valence/conduction electrons to unoccupied states above the Fermi level. In this case a plasmon peak is observed at approximately 23 eV. At an energy loss of 68 eV is the Ni $M_{2,3}$ absorption edge, where the spectroscopic notation refers to the excitations of Ni $3p_{1/2}$ and $3p_{3/2}$ electrons to states above the Fermi level. Finally, at an energy loss of 855 eV is the Ni $L_{2,3}$ absorption edge, caused by excitations of Ni $2p_{1/2}$ and $2p_{3/2}$ core electrons to states above the Fermi level as described in the previous section.

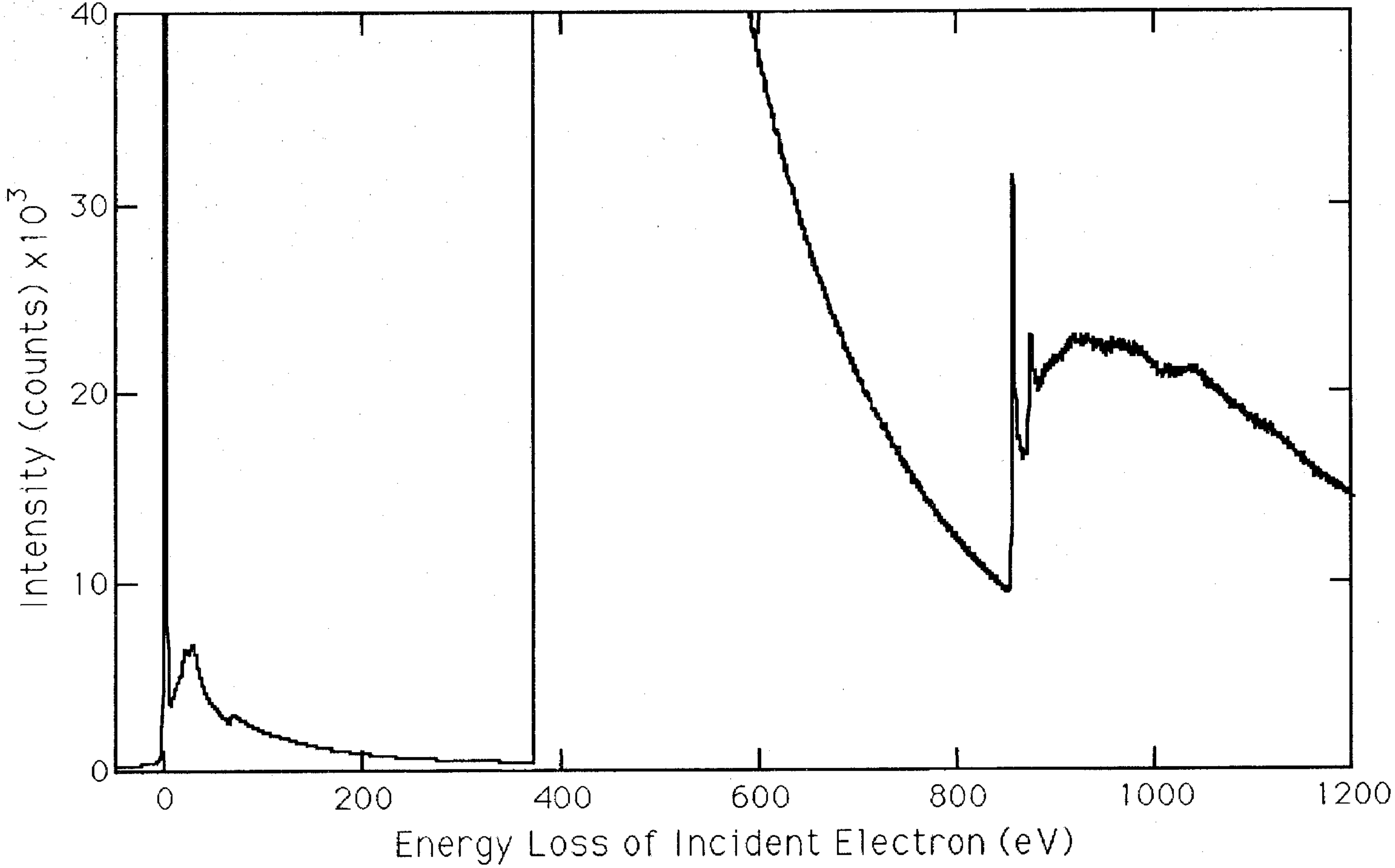

Figure 1.5. Energy loss spectrum for Ni metal. The discontinuity at 375 eV is due to a change in the detector gain. The maximum of the zero loss peak is not shown as scaled.

In general, metals will possess low loss features similar to those shown in Figure 1.5. The specific absorption edges present, however, as well as the energies at which they occur will depend upon the chemical composition of the sample under examination. In addition, the shapes of the edges can depend somewhat on the presence of multiple inelastic scattering, as it is likely in that some incident electrons will undergo more than one energy loss event. This effect can largely be removed from the spectra, however, using deconvolution techniques described in Chapter 2.

1.3 General Remarks and Outline

The aims of the work reported in this thesis were twofold. The first was to investigate the quantitative relationship between the intensities of the white lines and the occupancies of the corresponding outer *d* states at transition metal atoms. An experimental analysis of the energy loss spectra for the pure 3*d* and 4*d* transition metals was performed, and the relative intensities of the white lines were found to decrease linearly in a manner consistent with the linear filling of the 3*d* and 4*d* bands. This result made possible the second aim, which was to investigate changes in the intensities of the white lines that were due to alloying and solid state phase transformations with the goal of inferring changes in the occupancies of the outer *d* states.

A variety of transition metal alloys were investigated in the latter work. A number of binary copper alloys were chosen for study since, in pure form, copper has no white lines because of its full 3*d* band. The presence of any white lines at the copper $L_{2,3}$ edge that are due to a depletion of 3*d* electrons as a result of alloying would then be easily observed. In addition, Fe-Co alloys of varying composition were examined. The charge transfer effects in Fe-Co that were due to alloying had been studied by other researchers in our group using Mössbauer spectrometry, providing results with which to compare the EELS measurements. Measurements on several nickel alloys were also performed.

The remainder of the thesis is outlined as follows. In Chapter 2 the inelastic scattering of fast electrons and methods of removing multiple inelastic scattering from spectra are briefly reviewed. In Chapter 3 EELS instrumentation and experimental procedures are described. In Chapter 4 the analysis of the white lines from spectra of the 3*d* and 4*d* transition metals is presented which provides, given certain assumptions, an empirical procedure for measuring changes in the occupancies of the outer *d* states at transition metal atoms. Atomic Hartree-Slater calculations of the white line intensities are presented for comparison. In Chapter 5, $L_{2,3}$ absorption spectra for the various alloys are presented, and changes in the *d* state occupancy local to copper atoms are inferred from the data. These measurements are compared to other measurements as well as density of states calculations from the literature where available. The measurements are also discussed in terms of the heats of formation of the alloys. A summary of the results is presented in Chapter 6, and absorption spectra for the pure 3*d* and 4*d* transition metals are presented in Appendix 1.

References for Chapter 1

Atwater, H. A., and Ahn, C. C., Appl. Phys. Lett. 58 (3), 269 (1991).

Brown, M., Peierls, R. E., and Stern E. A., Phys. Rev. B 15 (2), 738 (1977).

Disko, M. M., Ahn, C. C., and Fultz, B., eds., Applications of Transmission EELS in Materials Science, The Metallurgical Society, Inc., Warrendale, PA, in press (1992).

Egerton, R. F., Electron Energy-Loss Spectroscopy in the Electron Microscope, Plenum Press, New York and London (1986).

Gasiorowicz, S., Quantum Physics, J. Wiley, New York, p. 351 (1974).

Horsley, J. A., J. Chem. Phys., 76 (3), 1451 (1982).

Leapman, R. D., and Grunes, L. A., Phys. Rev. Lett. 45 (5), 397 (1980).

Lytle, F. W., Wei, P. S. P., Greegor, R. B., Via, G. H., and Sinfelt, J. H., J. Chem. Phys. 70 (11), 4849 (1979).

Mansour, A. N., Cook, J. W., and Sayers, D. E., J. Phys. Chem. 88, 2330 (1984).

Mattheiss, L. F., and Dietz, R. E., Phys. Rev. B 22 (4), 1663 (1980).

Morrison, T. I., Brodsky, M. B., and Zaluzec, N.J., Phys. Rev. B 32 (5), 3107 (1985).

Mott, N. F., Proc. R. Soc. Lond. 62, 416 (1949).

Pease, D. M., Bader, S. D., Brodsky, M. B., Budnick, J. I., Morrison, T. I., and Zaluzec, N. J., Phys. Lett. 114a (8,9), 491 (1986).

Rudberg, E., Proc. R. Soc. London A127, 111 (1930).

Sham, T. K., Phys. Rev. B 31 (4), 1903 (1985).

Sham, T. K., Solid State Comm. 64 (8), 1103 (1987).

Sham, T. K, Tan, K. H., Yiu, Y. M., Physica B 158, 28 (1989).

Stern, E. A., and Rehr, J. J., Phys. Rev. B 27, 3351 (1983).

Thole, B. T. and van der Laan, G., Europhys. Lett. 4 (9), 1083 (1987).

Veldkamp, J., Physica 2, 25 (1935).

Waddington, W. G., Rez, P., Grant, I. P., and Humphreys, C. J., Phys. Rev. B 34 (3), 1467 (1986).

Zaanen, J., Sawatzky, G. A., Fink, J., Speier, W., and Fuggle, J. C., Phys. Rev. B 32 (8), 4905 (1985).

Chapter 2 Electron Scattering in the Electron Microscope

In this chapter the scattering of fast electrons as it pertains to electron energy loss spectrometry is discussed. In §2.1 the inelastic scattering of electrons by atoms is briefly reviewed. The discussion largely follows that of Egerton (1986). Methods of removing the unwanted multiple inelastic scattering from energy loss spectra are discussed in §2.2.

2.1 Scattering of Electrons by Atoms

Consider the scattering of a fast electron by an atom. The kinematics of the scattering process is illustrated in Figure 2.1. As indicated, a fast electron suffers an inelastic collision with an atom and is deflected by an angle θ from its original path. The wave vectors of the electron before and after the collision are given by $\mathbf{k}_0$ and $\mathbf{k}_1$ respectively, and the change in wave vector is given by

$$\mathbf{q} = \mathbf{k}_0 - \mathbf{k}_1. \tag{2.1}$$

It is customary to assume that the scattering is symmetric in the azimuthal angle, such that Figure 2.1 has rotational symmetry about $\mathbf{k}_0$. In that case the vector notation may be dropped and the scattering process may be described in terms of the scalar wave numbers and the angle θ.

To establish the relationship between energy loss and the scalar wave numbers note that conservation of energy gives $W_b - E = W_a$, where W_b and W_a are the total energies of the electron before and after the collision, and E is the energy loss. This gives

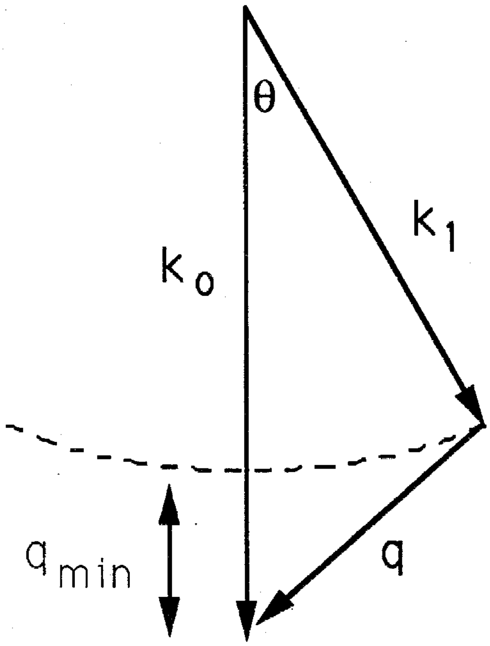

Figure 2.1. Scattering kinematics for an electron inelastically scattered by an atom.

$$[(m_o c^2)^2 + \hbar^2 k_o^2 c^2]^{1/2} - E = [(m_o c^2)^2 + \hbar^2 k_1^2 c^2]^{1/2}, \qquad (2.2)$$

which reduces to

$$k_1^2 = k_o^2 - \frac{2\gamma m_o E}{\hbar^2} + \frac{E^2}{(\hbar c)^2}, \qquad (2.3)$$

where $\gamma = (1 - v^2/c^2)^{-1/2}$. It is worthwhile to note that Equation 2.3 is independent of the scattering angle, and therefore all scattered wave vectors of the same length represent inelastic events with the same energy loss. In Figure 2.1 this means that there is a minimum value of q, q_{min}, for a given energy loss. In addition, once a given energy loss has been specified, θ uniquely determines q and vice versa. Therefore, there is also a maximum value of q, q_{max}, determined by the maximum scattering angle for which electrons will be collected by the spectrometer, which is in turn governed by the microscope/spectrometer geometry. This maximum scattering angle is commonly called the collection angle, β. Thus, the scattered intensity is a function of both q and E, which are independent aside from E specifying a value of q_{min}.

In an ionizing collision, the incident electron scatters from an atom through the Coulomb interaction and excites the atom from an initial state, $|i\rangle$, to a final state, $|f\rangle$. In an energy loss experiment, such scattered electrons are collected over a range of q and are analyzed according to energy (or energy loss). The intensity represented in an energy loss spectrum as function of collection angle and energy loss is given by (Egerton, 1986):

$$I(E, \beta) = N\, I_t(\beta)\, \frac{d\sigma}{dE}(E, \beta). \tag{2.4}$$

In this expression N is the number of atoms per unit area in the sample illuminated by the incident beam, $I_t(\beta)$ is the total number of electrons collected by the spectrometer through some collection angle β, and $d\sigma/dE$ is an energy-differential cross section per atom for electrons collected through β and scattered into an energy element dE about an energy loss E, i.e., a cross section per unit energy.

The evaluation of $d\sigma/dE$ was first performed by Bethe (1930) and subsequently reviewed in detail by Inokuti (1971). In the first Born approximation, which assumes that the potential acts as a weak perturbation to the incident fast electron, $d\sigma/dE$ is given by (in SI units)

$$\frac{d\sigma}{dE} = \frac{8\pi\hbar^2}{a_o^2\, m_o^2\, v^2} \int_{q_{min}}^{q_{max}} \frac{1}{q^3}\, \left| \langle f | e^{i\mathbf{q}\cdot\mathbf{r}} | i \rangle \right|^2 dq, \tag{2.5}$$

where $\mathbf{r}$ is the position vector of the incident electron, a_o is the Bohr radius, m_o is the rest mass of the electron, and v is the speed of the incident electron. The matrix element is evaluated over the coordinates of all the atomic electrons. In the derivation of this expression, it is assumed that only one scattering event occurs. In addition, the sum over all energy-degenerate initial and final states is implicitly assumed in Equation 2.5. Furthermore, $\langle f|$ is considered a continuum wave function normalized per unit energy, i.e.,

$$\int_0^\infty | \langle f_E | f_{E'} \rangle |^2 r^2 \, dr = \delta (E-E'), \qquad (2.6)$$

and Equation 2.5 is therefore dimensionally correct.

Although Equation 2.5 is derived solely from atomic scattering considerations, calculations based upon it reproduce the overall edge shapes observed in the energy loss spectra of solids for the excitations of atomiclike core electrons quite well. Leapman et al. (1980) calculated the *K, L,* and *M* ionization cross sections for a number of elements in the one-electron approximation using Hartree-Slater wave functions and found good agreement with observed spectra. Similar calculations by Ahn and Rez (1985) were also in good agreement with observed spectra.

Equation 2.5 may also be generalized and used in calculations of the fine structure at ionization edges that is due to solid state effects. In this case it is customary to replace the sum over the degenerate, continuum (final) states with a density of final states representative of the solid (Manson, 1978). As the core (initial) electron states are filled, only the density of final states need be considered. This generalization gives

$$\frac{d\sigma}{dE} = \frac{8 \pi \hbar^2}{a_o^2 \, m_o^2 \, v^2} \; n(E) \int_{q_{min}}^{q_{max}} \frac{1}{q^3} \, | \langle f \, | e^{i\mathbf{q}\cdot\mathbf{r}} | \, i \rangle |^2 \, dq. \qquad (2.7)$$

In Equation 2.7, the wave functions are those appropriate to the solid, and the units for n(E) again make the equation dimensionally correct.

Using this expression Weng et al. (1989) calculated the near-edge structure at the *K* and *L* absorption edges of a number of compounds with substantial accuracy. The one-electron, initial-state wave functions were obtained from Hartree-Slater calculations, while the density of states and final-state wave functions were obtained from pseudoatomic-orbital band-structure calculations. In similar work Müller et al. (1982) calculated the fine structure at the *K*, *L*, and *M* edges for some of the 3*d* and 4*d* transition metals using a linearized, augmented, plane-wave method. The results were in good agreement with observed spectra as well.

As mentioned, these expressions are based upon the assumption that the incident electron undergoes one inelastic scattering event. In practice, however, some incident electrons are likely to suffer more than one inelastic scattering event. Processing techniques for removing the effects of this multiple, inelastic scattering from energy loss spectra are discussed in the next section.

2.2 Multiple Inelastic Scattering

Contrary to the single scattering process described in the previous section, there is a significant probability that an incident electron will suffer more than one energy loss event. The likelihood of multiple inelastic-scattering processes increases with specimen thickness. This effect is observed as a replication of the low-loss behavior following the threshold of an absorption edge. Two approximate deconvolution methods are widely used to retrieve the single scattering contribution from energy loss spectra: the Fourier-log method and the Fourier-ratio method. Both methods were used in this study.

The Fourier-log method, originated by Burge and Misell (1968) and Misell and Jones (1969) and later improved upon by Johnson and Spence (1974), assumes that the scattering events are independent and follow a Poisson statistical distribution in their order of scattering. These authors have shown that the measured intensity in an energy loss spectrum, I(E), can be written as

$$I(E) = Z(E) * [\delta(E) + \frac{1}{I_0} S(E) + \frac{1}{2!\, I_0^2} S(E) * S(E) + \ldots], \quad (2.8)$$

where Z(E) represents the zero loss peak, δ(E) is a delta function, S(E) is the single scattering contribution, I_0 is the incident-beam intensity, and * denotes a convolution. The approach is to take the Fourier transform of both sides of Equation 2.8, in which case the convolutions become multipications and the term in brackets can be summed as an exponential series to yield

$$S'(e) = I_0 \ln \left\{ \frac{I'(e)}{Z'(e)} \right\}. \quad (2.9)$$

Here, the primes denote the Fourier transform. In principle, taking the inverse Fourier transform of Equation 2.9 retrieves the single scattering contribution unbroadened by the instrumental resolution, but in practice the inverse transform contains considerable noise. The noise may be avoided, however, by reconvoluting with a Gaussian of width equal to that of the zero-loss peak (Johnson and Spence, 1974). The result is a deconvoluted (single scattering) spectrum uncorrected for the instrumental broadening of the zero-loss peak.

Regarding practical applications of the deconvolution, it is necessary to remove any gain changes in the spectra (see Figure 1.4) by suitably scaling the low-loss region. The high-energy region of the core-loss data must then be extrapolated to zero in order to minimize any discontinuity effects in the inverse transform. Following the deconvolution, the core-loss edge may be isolated from the preceding background by fitting a power-law function to a 50-100 eV region of the background and extrapolating it under the core-loss edge (Egerton, 1986). This function is then subtracted from the deconvoluted core-loss edge.

The Fourier-ratio method (Egerton and Whelan, 1974), which was also used in this study, amounts to treating the low-loss region as an "instrument function" for the core-loss absorption edge. In this method one first removes the pre-edge background intensity from the edge and then smoothly extrapolates the high-energy region of the core-loss edge to zero in order to minimize discontinuity effects. One then takes the Fourier transform of the core-loss region, divides by the Fourier transform of the low-loss region, and takes the inverse transform to obtain the single scattering contribution to the core-loss intensity. Noise problems may again be avoided by reconvoluting with a Gaussian of width equal to that of the zero-loss peak.

Both methods have advantages. The Fourier-log method is generally useful since it deconvolutes the entire energy loss spectrum, low loss as well as core loss. The Fourier-ratio method, however, cannot provide a single scattering spectrum for the low-loss region since the low-loss region is, by definition, the "instrument function." This method does, however, have the advantage that the low-loss spectrum and core-loss spectrum may be obtained separately, reducing data-acquisition times. This option is particularly useful when the core-loss edge of interest occurs at very large energy losses. The Fourier-ratio method was used to deconvolute spectra for the *4d* transition metals for just this reason. When applied to the same data, both methods yield the same results (Egerton et al. 1985).

It should be noted that both of these methods are, however, approximate, since the scattered intensity is a function of both energy loss and scattering angle. Deconvoluting with respect only to energy implicitly assumes that essentially all of the scattered electrons have been collected, but in practice this is not the case, as the collection angle is limited by the microscope/spectrometer geometry. It is therefore useful to know how large the collection angle should be to make the applications of these deconvolution routines justifiable.

A rough indication of the appropriate collection angle may be obtained by examining Equation 2.5. Differentiating with respect to q, thus removing the integral, yields a double-differential cross section, $d^2\sigma/dEdq$, which is a function of both q and E. This double-differential cross section can be expressed as a function of scattering angle, θ, rather than q, by noting from Figure 2.1 that

$$q^2 = k_o^2 + k_1^2 - 2k_o k_1 \cos\theta. \qquad (2.10)$$

Neglecting the matrix element for the moment, one finds for small angles

$$\frac{d^2\sigma}{dEd\Omega} \propto \frac{1}{(\theta^2 + \theta_E{}^2)^2}, \tag{2.11}$$

where $d\Omega$ is a solid angle element and θ_E is the "characteristic scattering angle" given by (Bethe, 1930):

$$\theta_E = \frac{E}{2E_o}, \tag{2.12}$$

where E_o is the incident-beam energy. It is worthwhile to note that θ_E is the classical scattering angle in "billiard-ball" collisions. Thus, for a given energy loss, E, the angular distribution of scattered electrons is the square of a Lorentzian of half-width θ_E. Equation 2.11, however, describes only single scattering. To describe double scattering, this expression should be convoluted with itself, as all the electrons represented in this distribution are themselves sources for subsequent scattering. Higher orders of multiple scattering are obtained through successive convolutions of Equation 2.11. Therefore, to apply the deconvolution procedures described safely, the collection angle should be considerably larger than θ_E.

In a more detailed calculation, Stephens (1980), using a Monte Carlo technique, estimated the fractional error by which double inelastic scattering would be oversubtracted in an angle-independent deconvolution for 80 keV incident electrons. The results indicated that error would be less than 10% for energy losses up to 1600 eV, using a collection angle equal to the characteristic angle of 10 mrad.

In a more recent study, Egerton and Wang (1989) estimated that the error in removing double scattering by angle-independent deconvolution would be less than 10% for edge energies below 5 keV, given a collection angle of 10 mrad and 100 keV incident electrons. It is worthwhile to note that in this case the collection angle is less than half of the characteristic angle of 25 mrad.

Another assumption implicit in these deconvolution procedures is that the sample is of uniform thickness. Johnson and Spence (1974) estimated the error in an angle-independent deconvolution that was due to a wedge-shaped sample of nominal thickness t with slightly decreasing thickness. They found that compared to a sample of uniform thickness t, double inelastic scattering would be slightly undersubtracted in a wedge sample with a small thickness variation.

In summary, when applying angle-independent deconvolution procedures, one should prepare samples as uniformly thin as possible and choose collection angles considerably larger than the characteristic scattering angle, θ_E. The fractional errors in removing multiple scattering should then be less than 10%.

The actual determination of the collection angle depends on whether the data are obtained in image mode or diffraction mode. The situation for image mode is illustrated schematically in Figure 2.2. Although the lens configuration shown is considerably oversimplified, one can see that the collection angle is dependent upon the presence of an

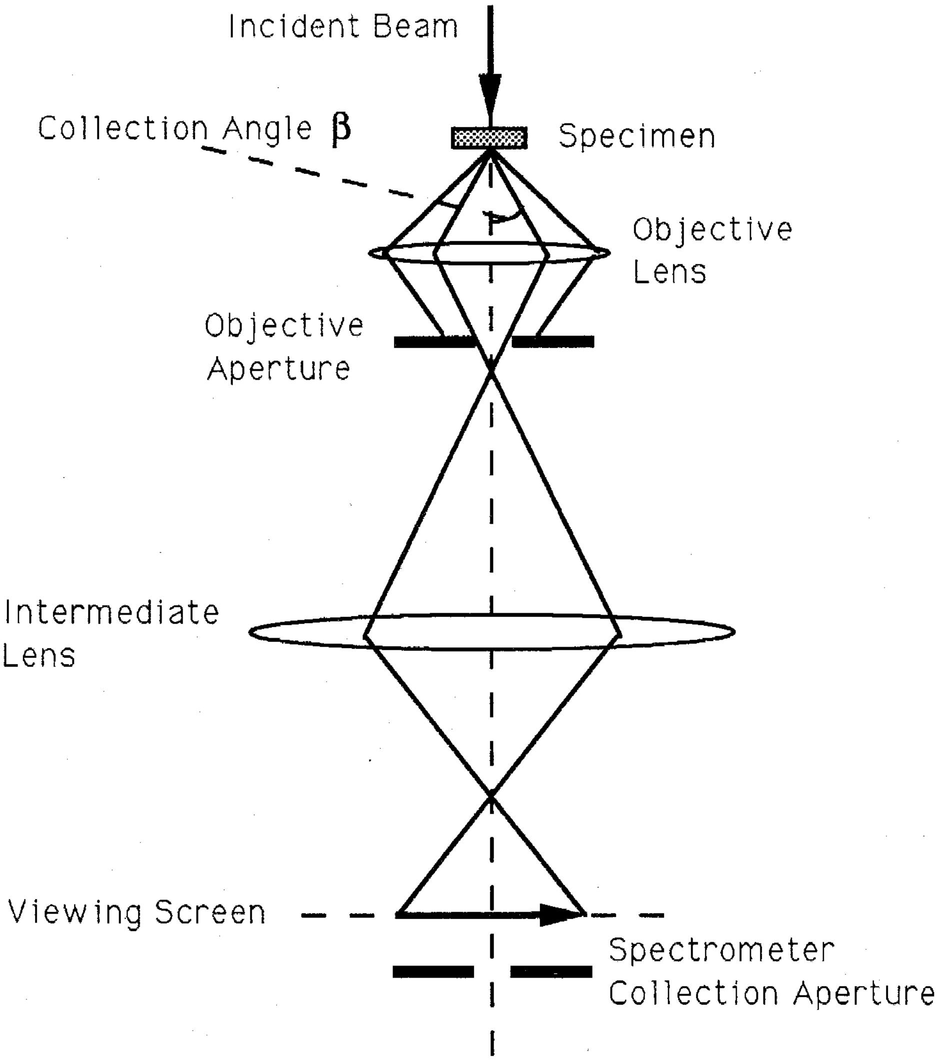

Figure 2.2. Collection-angle geometry for energy loss spectra collected in a transmission electron microscope in image mode.

objective aperture placed at the back focal plane of the objective lens. In the complete absence of an objective aperture, the collection angle will be determined by some other physical limiting feature of the microscope. For the Philips EM 430 microscope used in this study, this physical limitation is the differential pumping aperture situated near the first projector lens (Philips Electronics, 1991). In addition, as shown in Figure 2.2, electrons that originate from the region of the sample whose image intersects the spectrometer collection aperture will be collected by the spectrometer.

In diffraction mode, the situation is somewhat simpler since a diffraction pattern is projected onto the viewing screen with an effective camera length chosen by the operator. As illustrated in Figure 2.3, the collection angle is simply determined by the width of the spectrometer aperture and the camera length. The maximum collection angle attainable in diffraction mode is considerably smaller than that attainable in image mode, however. At the shortest camera length setting of 80 mm on the Philips EM 430, a collection aperture of 5 mm yields a collection angle of approximately 31 mrad, whereas in image mode the maximum collection angle is well over 100 mrad.

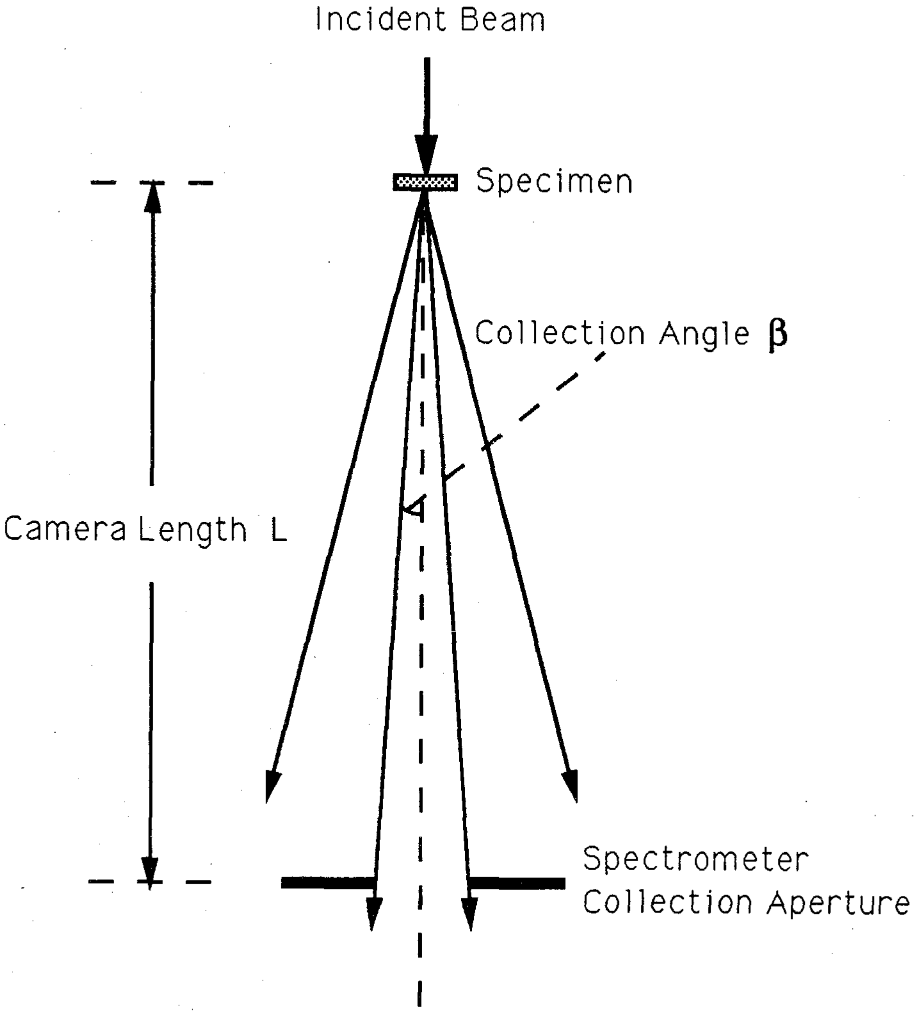

Figure 2.3. Collection-angle geometry for energy loss spectra collected in a transmission electron microscope in diffraction mode.

References for Chapter 2

Ahn, C. C..and Rez, P., Ultramicroscopy 17, 105 (1985).

Bethe, H. A., Ann. Phys. 5, 325 (1930).

Burge, R. E. and Misell, D. L., Phil. Mag. 18, 251 (1968).

Egerton, R. F. and Cheng, S. C., 43rd Ann. Proc. Electron Microsc. Soc. Amer., eds. G. W. Bailey, San Francisco Press, San Francisco, pp. 389-399 (1985).

Egerton, R. F., Electron Energy Loss Spectroscopy in the Electron Microscope, Plenum, New York and London, pp. 129-228 and 246-255 (1986).

Egerton, R. F. and Whelan, M. J., Phil. Mag. 30, 739 (1974).

Egerton, R. F. and Wang, Z. L., Ultramicroscopy 32, 137 (1989).

Inokuti, M., Rev. Mod. Phys. 43, 297 (1971).

Johnson, D. W. and Spence, J. C. H., J. Phys. D 7, 771 (1974).

Leapman, R. D., Rez, P., and Mayers, D. F., J. Chem. Phys. 72(2), 1232 (1980).

Manson, S. T., in Topics in Applied Physics, Vol. 26, ed. M. Cardona and L. Ley, Springer-Verlag, New York, pp. 135-163 (1978).

Misell, D. L., and Jones, A. F., J. Phys. A 2, 540 (1969).

Müller, J. E., Jepsen, O., and Wilkins, J. W., Solid State Comm. 42(5), 365 (1982).

Philips Electronics, Private communication with Irene Piscopo (May, 1991).

Stephens, A. P., Ultramicroscopy 5, 343 (1980).

Weng, X., Rez, P., and Sankey, O. F., Phys. Rev. B 40(8), 5694 (1989).

Chapter 3 Instrumentation and Experimental Procedures

In this chapter the experimental procedures and instrumentation used in this study are discussed. The sample preparation methods are described in §3.1. Routine characterization methods are described in §3.2. The energy loss data acquisition and processing methods are described in §3.3.

3.1 Sample Preparation

Transmission electron microscopy samples of elemental transition metals and various alloys were required for this study. The alloys CuZr, $Cu_{10}Zr_7$, CuTi, CuPd, CuAu, Ni_3Al, Ni_3V, and Fe-Co (of varying composition) were prepared from elemental metals of at least 99.99% purity either by induction melting on a water cooled silver hearth in an argon atmosphere or by arc melting on a water cooled copper hearth in an argon atmosphere. The resulting ingots were inverted and remelted several times to ensure homogeneity. The mass losses after melting were negligible, so the chemical compositions of the alloys were assumed to be those of the respective stoichiometric compounds.

Thin alloy foils were then prepared by quenching molten droplets of the alloys between copper disks using an Edmund Buhler Ultra Rapid Quencher, shown schematically in Figure 3.1 The apparatus is operated by levitating and melting a small piece of the ingot (~ 150 mg) in a purified argon atmosphere, using a 2.2 MHz radio frequency (RF) power supply connected to a conically shaped copper coil. When the current to the coil is removed, the molten droplet falls, triggering a detector, which causes

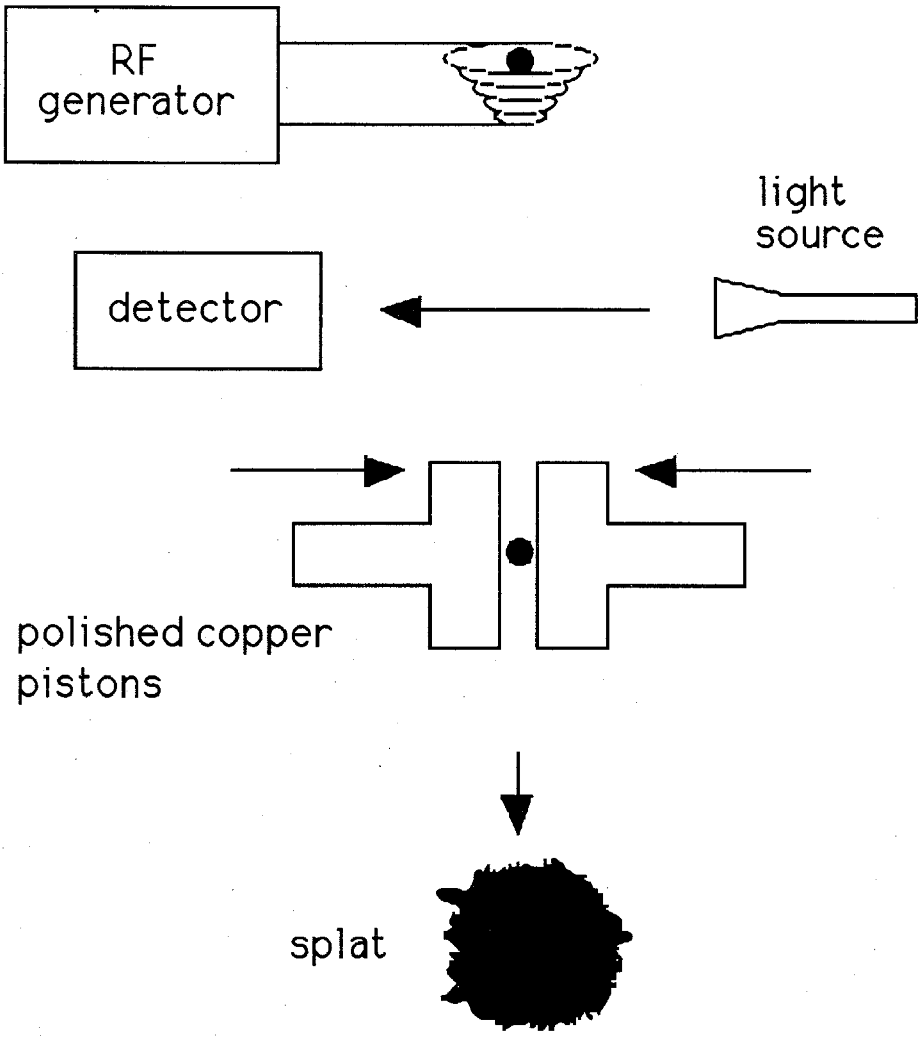

Figure 3.1. Illustration of the rapid quenching apparatus.

two polished Cu pistons to accelerate toward each other. The pistons smash the droplet as it falls, rapidly quenching it into a foil approximately 50 μm in thickness, commonly called a "splat." Depending upon the thermal conductivity of the sample and the resulting thickness of the splat, quench rates of 10^6 °K/sec are attainable. In addition to the alloys mentioned, a CuPt alloy was prepared directly in the rapid quencher. Wires of the pure metals were twisted together, levitation-melted, and immediately rapidly quenched.

For energy loss analysis in the TEM, electron transparent samples less than about 100 nm in thickness were required. A number of preparation techniques were used to prepare these samples. For many of the elemental transition metals, disks 3 mm in diameter were cut from pure, thin foils and were then electrochemically polished with a Fishione jet electropolisher, using appropriate chemical solutions. In other cases, pure metal films less than 100 nm in thickness were prepared by thermal evaporation, electron-beam evaporation, and direct-current ion sputtering onto single-crystal NaCl substrates. The resulting films were then floated off the substrates in water and picked up with Cu TEM grids.

Electrochemical thinning was used to prepare TEM samples from most of the alloy foils. An acceptable chemical thinning solution was not found for CuPt, however, so this sample was first mechanically thinned to a thickness of approximately 5 microns on a VCR Dimpler and was then ion-milled with a VCR dual-gun argon ion-mill to its final thickness. The TEM sample-preparation techniques used for the various metals and alloys are summarized in Table 3.1.

Metal or Alloy	TEM Sample-Preparation Technique
Ti	40 nm thin film sputtered between 15 nm Cr buffers to prevent oxidation.
V	Thin film by sputtering
Cr	Thin film by sputtering (see Ti)
Fe	Thin foil polished at 10°C 20% perchloric acid, 80% acetic acid
Co	Thin CoFe foil polished at 10°C 20% perchloric acid, 80% acetic acid
Ni	Thin foil polished at 10°C 20% perchloric acid, 80% acetic acid
Cu	Thin foil polished at -30°C 33% nitric acid, 67% methanol
Zr	Thin foil polished at -30°C 5% perchloric acid, 95% methanol
Nb	Thin foil polished at -10°C 20% sulfuric acid, 80% methanol
Mo	Thin foil polished at -10°C 20% sulfuric acid, 80% methanol
Ru	Thin film by electron-beam evaporation

Table 3.1. TEM sample-preparation techniques for metals and alloys.

Metal or Alloy	TEM Sample-Preparation Technique
Rh	Thin film by thermal evaporation
Pd	Thin film by thermal evaporation
Ag	Thin foil polished at 10°C 20% perchloric acid, 80% acetic acid
CuPd	Thin foil polished at 10°C 25% perchloric acid, 75% acetic acid
CuAu	Thin foil polished at 10°C 25% perchloric acid, 75% acetic acid
CuZr	Thin foil polished at -30°C 33% nitric acid, 67% methanol
$Cu_{10}Zr_7$	Thin foil polished at -30°C 33% nitric acid, 67% methanol
CuTi	Thin foil polished at -30°C 33% nitric acid, 67% methanol
CuPt	Thin foil dimpled, then ion-milled
Ni_3V	Thin foil polished at 10°C 10% perchloric acid, 90% acetic acid
Fe-Co	Thin foils polished at -30°C 25% perchloric acid, 75% ethanol

Table 3.1 continued. TEM sample-preparation techniques for metals and alloys.

3.2 Routine Characterization of Alloys

The structures of the rapidly quenched alloy splats were characterized using x-ray diffraction. A General Electric XRD-5 θ-2θ diffractometer (Cr Kα radiation) and a Philips θ-2θ diffractometer (Cu Kα radiation) were used to analyze the $Cu_{10}Zr_7$, Ni_3V, and Fe-Co alloys. An INEL CPS 120 x-ray diffractometer (Co Kα radiation and graphite incident beam monochromator) was used to analyze the CuZr, CuTi, CuPt, CuAu, CuPd, and Ni_3Al alloys. This instrument, shown schematically in Figure 3.2, utilizes a geometry in which the sample, x-ray beam, and detector are all rigidly fixed. The x-ray beam strikes the sample surface at an incident angle, α, and diffracted x-rays are collected in parallel over a 127° range with the large-angle detector. The θ–2θ geometry is shown for a particular set of grain orientations.

For finely grained or amorphous samples these instruments provide powder diffraction patterns such as the one for CuPd shown in Figure 3.3. At room temperature, the equilibrium crystal structure of CuPd is the B2 (ordered bcc) structure. At temperatures above approximately 600°C, however, the structure transforms to a disordered fcc solid solution. The diffraction pattern shown in Figure 3.3 indicates that the disordered fcc structure was obtained as a result of the rapid quenching process. The room-temperature, equilibrium crystal structures and the structures obtained after rapid quenching are summarized in Table 3.2. The equilibrium crystal structure data were taken from Massalski (1990).

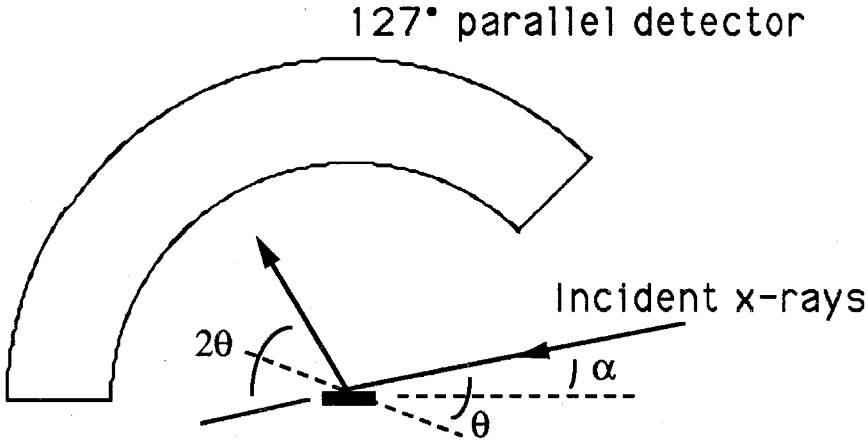

Figure 3.2. Diagram of the parallel-detection x-ray diffractometer.

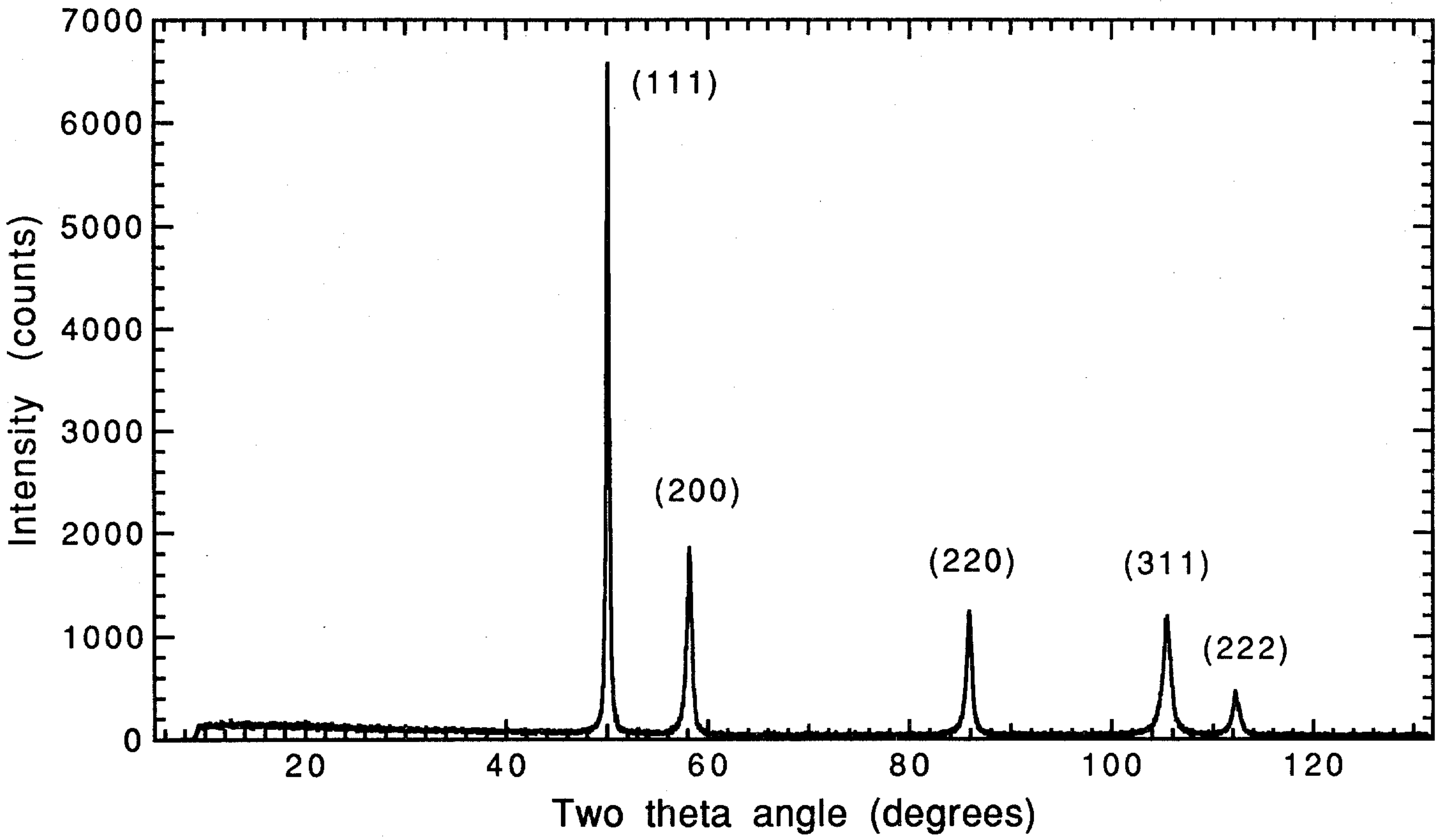

Figure 3.3. X-ray diffraction pattern obtained from rapidly quenched CuPd. The pattern indexes as fcc with hkl indices shown.

Alloy	Equilibrium Structure	As Quenched
$Cu_{10}Zr_7$	orthorhombic ($Ni_{10}Zr_7$ prototype)	amorphous
CuZr	B2 (ordered bcc) (above 715°C)	amorphous
CuPd	B2 (ordered bcc)	fcc
CuAu	$L1_0$ (ordered tetragonal)	fcc
CuPt	$L1_1$ (ordered rhombohedral)	fcc
CuTi	B11 (ordered tetragonal)	amorphous
Ni_3Al	$L1_2$ (ordered fcc)	$L1_2$
Ni_3V	DO_{22} (tetragonal)	fcc
FeCo	B2 (ordered bcc)	bcc
$Fe_{90.6}Co_{9.4}$	bcc	bcc
$Fe_{69}Co_{31}$	bcc	bcc
$Fe_{30}Co_{70}$	bcc	bcc

Table 3.2. Crystal structures for equilibrium and rapidly quenched alloys.

The enthalpies of ordering in Ni_3V and FeCo and the enthalpy of crystallization in $Cu_{10}Zr_7$ were measured with a Perkin-Elmer DSC-4 differential scanning calorimeter. These data were obtained for comparison to electron-transfer measurements as described in Chapter 5.

The DSC apparatus is shown schematically in Figure 3.4. The instrument heats an empty reference crucible (an aluminum pan) at a constant heating rate while adding slightly more or less heat to the crucible containing the sample so as to maintain them at the same temperature. The difference in the heat-flow rates versus temperature (or time) provides the DSC "scan," which shows peaks or valleys when the sample undergoes endothermic or exothermic transformations. The area of the peak (integrated heat flow) gives the total heat of the transformation.

Sample and reference pans were heated under flowing argon gas at a heating rate of 20°C/min. Two DSC scans from 50°C to 600°C were obtained from each sample, the second immediately following the first. The first scan provided the crystallization or ordering treatment. The second scan (on the now transformed sample) provided the "baseline" scan. The second scan was subtracted from the first, isolating the signal that was due to the transformation. The instrument was calibrated for temperature and heat-flow rate using the known melting temperature and heat of fusion of indium.

For illustration, the "difference" scan for the rapidly quenched Ni_3V alloy is shown in Figure 3.5. An exothermic peak is observed beginning

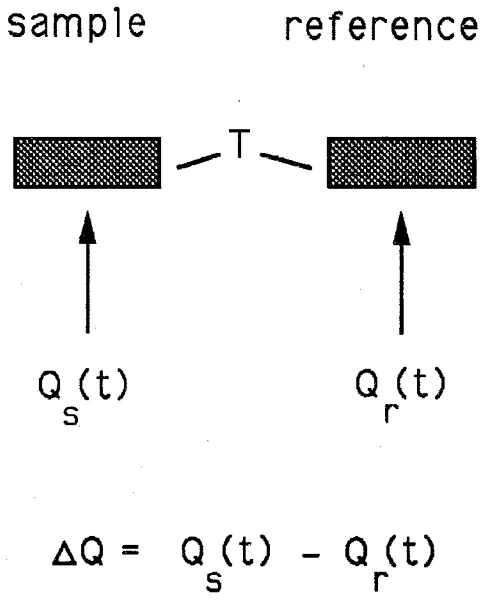

Figure 3.4. Schematic of the DSC sample and reference pan arrangement.

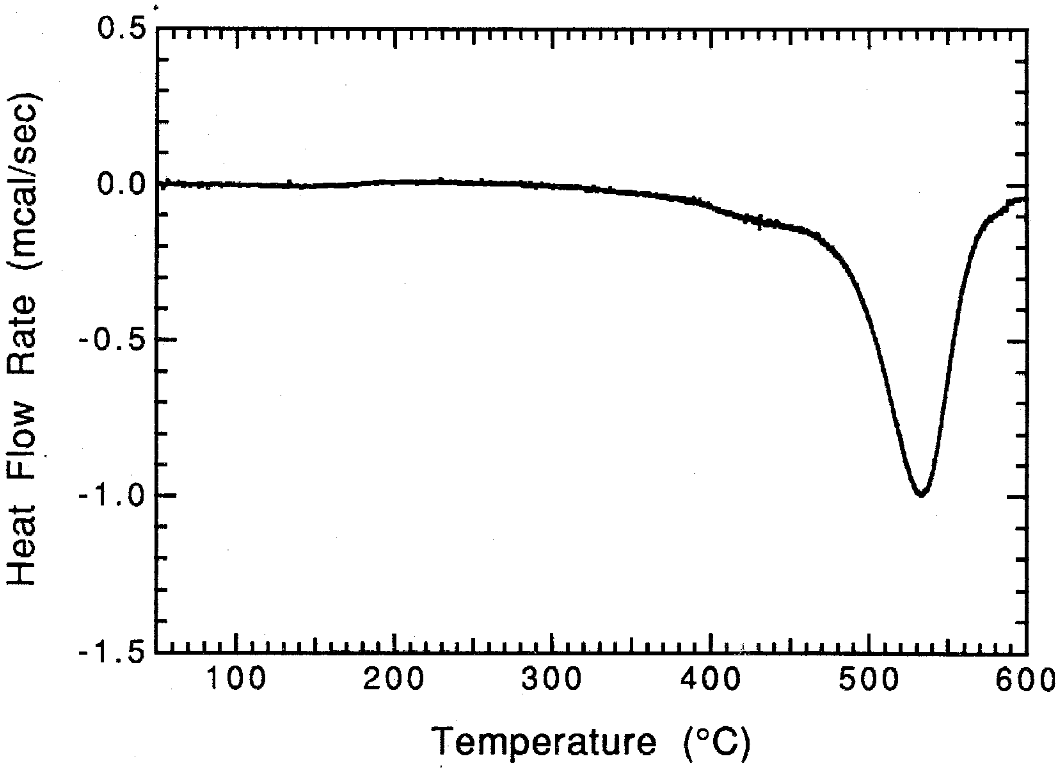

Figure 3.5. DSC "difference" scan obtained from Ni_3V at a heating rate of 20°C/min.

near 400°C, the integrated peak area corresponding to an enthalpy release of approximately 4 kJ/mole.

The TEM used in this study was a Philips EM 430 transmission electron microscope equipped with an EDAX 9900 energy-dispersive x-ray (EDX) analyzer. The computer hardware for the EDAX unit consisted of a PDP-11 computer with a multichannel analyzer. The analysis software was that provided by EDAX. The Philips EM 430 served mainly as an electron source for the energy loss spectrometer. However, it was used to obtain routine structural information from the alloy samples. In addition, the EDAX unit was used to verify chemical compositions of the alloy samples. The alloys were found to be stoichiometric to within the 5% uncertainty in the EDX analysis.

3.3 EELS Data Acquisition and Processing

The experimental equipment central to this study consisted of a Gatan 607 serial-detection electron energy loss spectrometer, which was mounted to the bottom of the optical column of the Philips EM 430 TEM. Later in the study, however, a Gatan 666 parallel-detection electron energy loss spectrometer was also used to obtain data. The Gatan 607, shown schematically in Figure 3.6, is a serial-acquisition spectrometer that incorporates a 90° magnetic prism to separate spatially electrons of different kinetic energies. The spectrometer is equipped with magnetic focusing lenses for maximizing the energy loss signal onto the scintillator/photomultiplier tube detector as well as an electrostatically isolated drift tube for changing the kinetic energy of the electrons by fixed

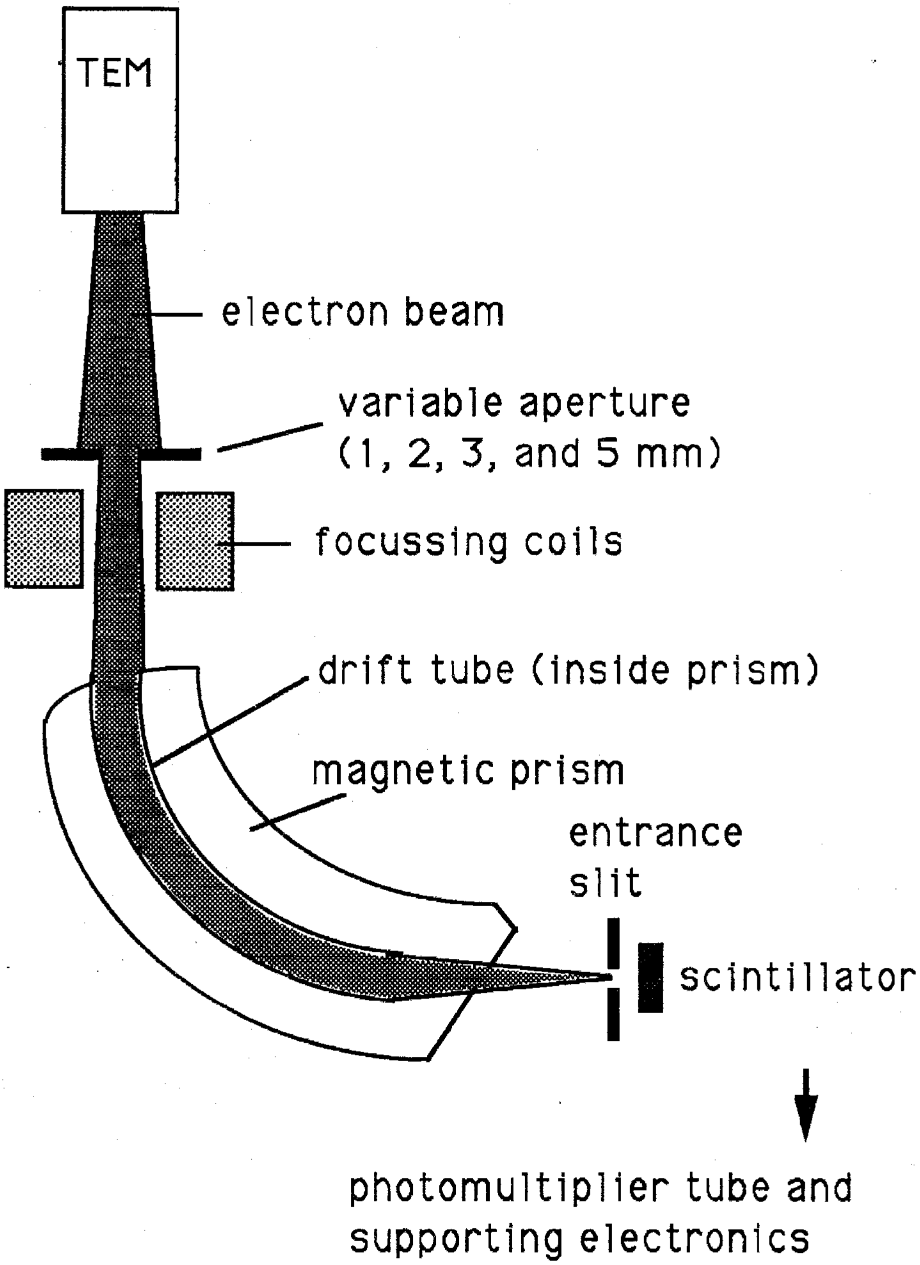

Figure 3.6. Simplified schematic of the Gatan 607 energy loss spectrometer.

offsets for acquiring spectra from different energy loss regions. During operation, the magnetic field strength of the prism is systematically varied to scan electrons of different energies across a fixed entrance slit to the detector.

The Gatan 666 is qualitatively similar in function except that it is a parallel acquisition unit with a detector that consists of a single-crystal yttrium-aluminum garnet (YAG) scintillator, fiber-optically coupled to a linear photodiode array. Instead of scanning the energy loss spectrum across a fixed slit, 1024 channels of data are simultaneously counted and recorded.

The control and acquisition software used in conjunction with the Gatan 607 was supplied by EDAX and implemented on a PDP-11 computer. Control and acquisition software for the Gatan 666 was supplied by Gatan and implemented on a Macintosh II microcomputer. In addition, software from both manufacturers contained various processing routines, some of which were used in this study.

The Gatan 607 spectrometer was used to obtain energy loss spectra from the elemental *3d* transition metals as well as the $Cu_{10}Zr_7$, Ni_3V, and Fe-Co alloys. Electron transparent samples of the *3d* metals were analyzed while operating the TEM in diffraction mode at 200 kV using a camera length of 80 mm and a spectrometer collection aperture of 3mm, yielding a collection angle of approximately 19 mrad. In comparison, the characteristic scattering angle for single scattering described in Chapter 2, is approximately 3 mrad for data collected through 1200 eV. Thus, the data were collected through scattering angles much larger than the characteristic angle. The spectra were collected with a dispersion setting of 0.4 eV/channel, and the energy resolution (FWHM of the zero-loss peak) so obtained was approximately 2.0 eV. These spectra were then transferred to a Digital Equipment Corporation MicroVax II and processed by Fourier-log deconvolution.

The Gatan 666 spectrometer, acquired at a later time during this study, was used to obtain energy loss spectra from the *4d* transition metals as well as from CuZr, CuTi, CuPd, CuAu, CuPt, and Ni_3Al. Electron transparent samples were analyzed in image mode at 200 kV with a spectrometer collection aperture of 3 mm at magnifications of 3560 X to 5070 X. As the Gatan 666 spectrometer can only collect 1024 channels of data simultaneously, the low-loss and core-loss spectra were acquired separately. No objective aperture was used, and the collection angle thus limited by the differential pumping aperture (Philips Electronics, 1991) was approximately 180 mrad. In comparison, the characteristic scattering angle for data collected through 3600 eV is approximately 9 mrad. The dispersion setting used for the *4d* metals was 1.0 eV/channel and provided an energy resolution of approximately 3.0 eV. Data from the alloys were acquired with a dispersion setting of 0.5 eV/channel, providing an energy resolution of approximately 3.0 eV.

Data acquired with the Gatan 666 spectrometer contained artifacts and noise that were due to the response and gain fluctuations of the linear photodiode array detector. These effects were minimized by dividing the data by the response function followed by gain averaging over many data channels (Shuman and Kruit, 1985). The approach was straightforward, but somewhat time consuming. Several spectra were collected for both the low-loss and core-loss regions, each shifted by a few data channels from the previous spectrum. These data were then divided by the response function determined by uniformly illuminating the photodiode array with no sample in place. This response function is shown in Figure 3.7. The individual spectra were then realigned to some common feature in the spectrum and added. This latter step reduces noise by averaging the channel-to-channel gain fluctuations of the detector. The low-loss and core-loss spectra were then transferred to a Macintosh microcomputer and deconvoluted by the Fourier-ratio method. The data collected and processed according to these methods are presented and analyzed in the following two chapters.

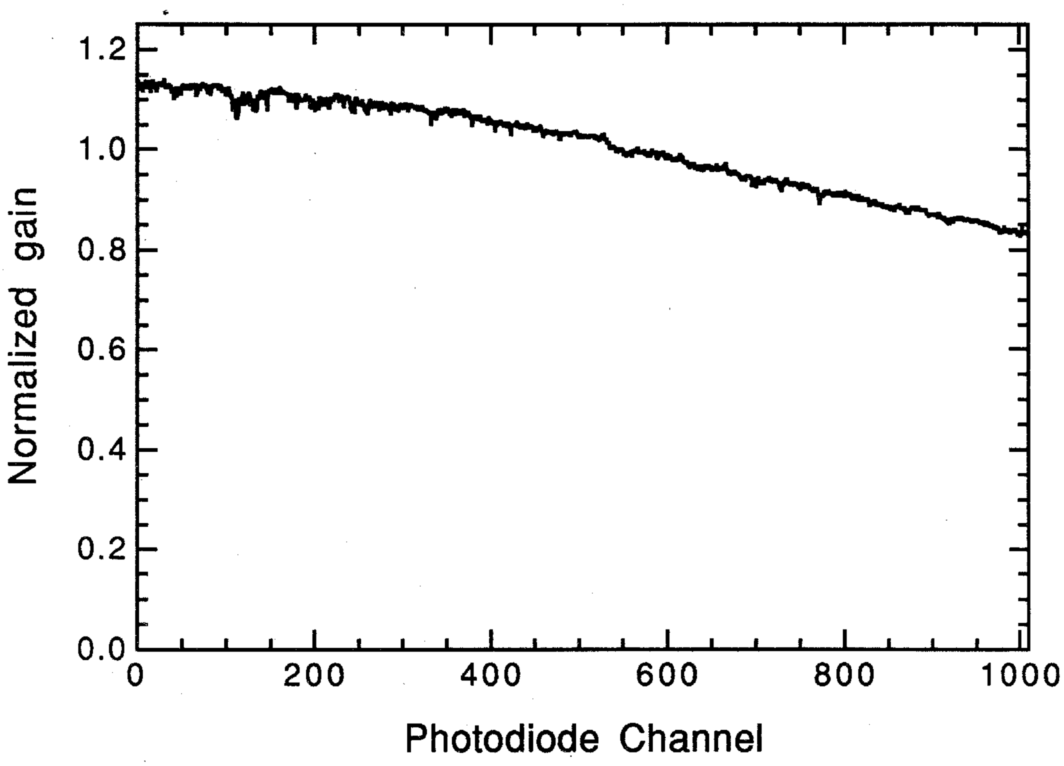

Figure 3.7. Response of the linear photodiode array detector under uniform illumination of 200 keV electrons.

References for Chapter 3

Massalski, T. B., ed., Binary Alloy Phase Diagrams, Vols. 1, 2, and 3., asst. eds. H. Okamoto, P. P. Subramanian, and L. Kacprzak, ASM International, Metals Park, OH (1990).

Philips Electronics, Private communication with Irene Piscopo (May, 1991).

Shuman, H. and Kruit, P., Rev. Sci. Instrum. 56, 231 (1985).

Chapter 4 White Line Analysis and Interpretation

In this chapter the analysis and interpretation of the data are described. In §4.1 the procedure used to isolate and normalize the white line intensity for the 3*d* and 4*d* transition metals is described, and the resulting correlations between normalized white line intensity and outer *d* state occupancy are presented. Atomic Hartree-Slater calculations of the matrix element contributions to these correlations are presented in §4.2. A discussion of these correlations, including their use for measuring changes in outer *d* state occupancy, is presented in §4.3.

4.1 White Lines in 3*d* and 4*d* Transition Metals

In the previous chapter the experimental procedures used to acquire and process the $L_{2,3}$ absorption spectra were described. The deconvoluted $L_{2,3}$ edges for the 3*d* transition metals with pre-edge backgrounds subtracted are shown in Figure 4.1. The corresponding data for the 4*d* transition metals are shown in Figure 4.2. Individual figures for these data are given in Appendix 1. In both figures the spectra have been scaled such that their background intensities are approximately equal in order to illustrate the systematic decrease in white line intensity with the filling of the outer *d* bands.

To establish the numerical proportionality between white line intensity and *d* holes, the white lines were first isolated from the background intensity and normalized. Figure 4.3 for niobium illustrates the method used for analyzing the spectra for the 4*d* transition metals. The background intensity was modeled by step functions since the edge

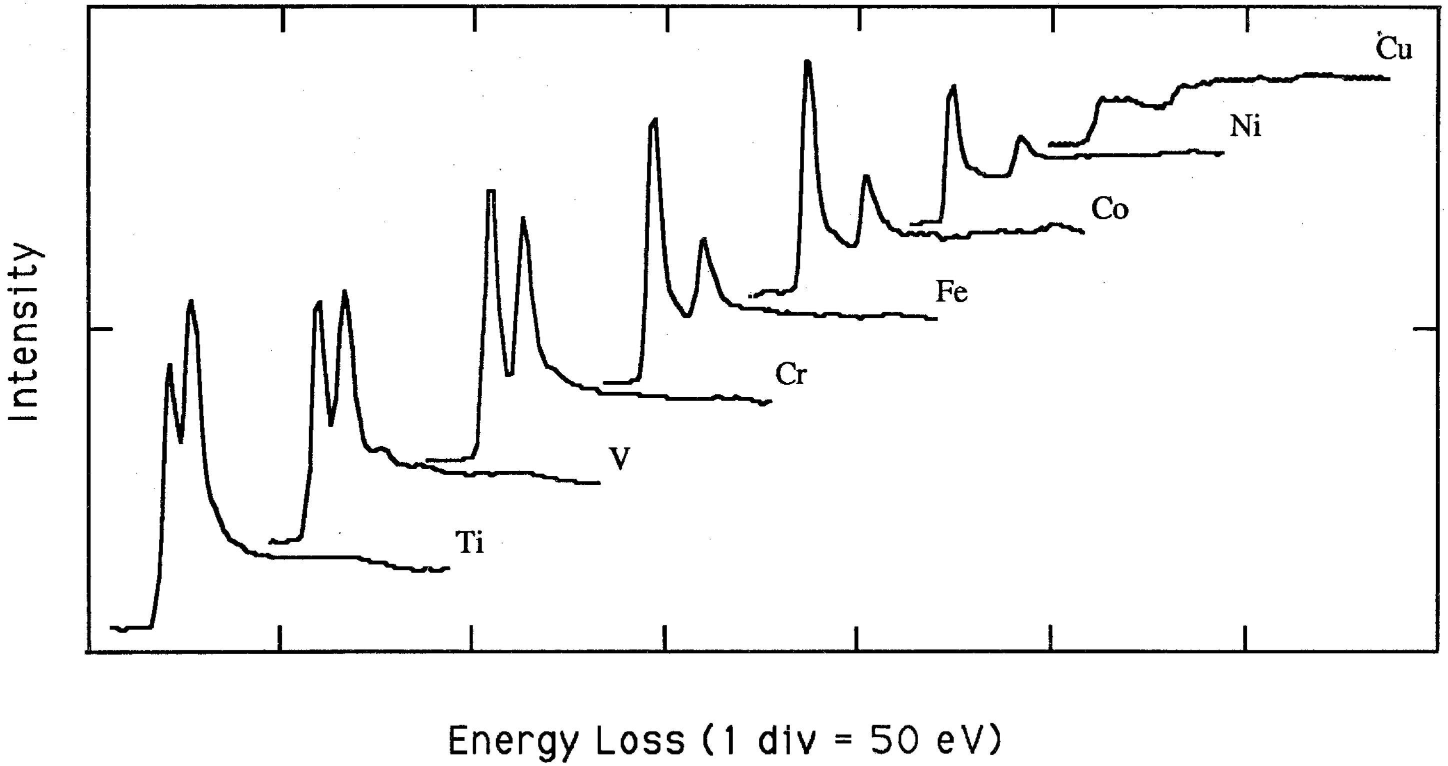

Figure 4.1. Background-subtracted and deconvoluted $L_{2,3}$ edges for the 3*d* transition metals.

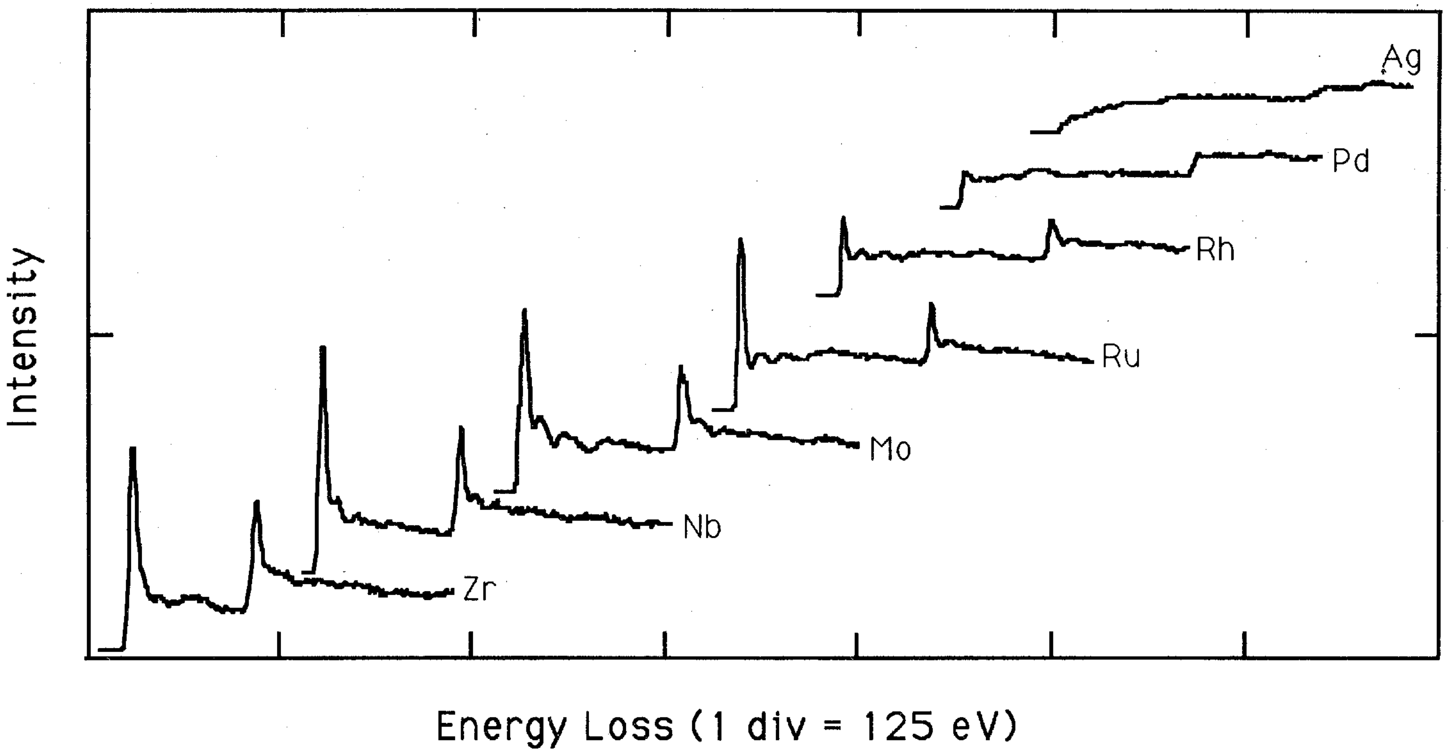

Figure 4.2. Background-subtracted and deconvoluted $L_{2,3}$ edges for the 4*d* transition metals.

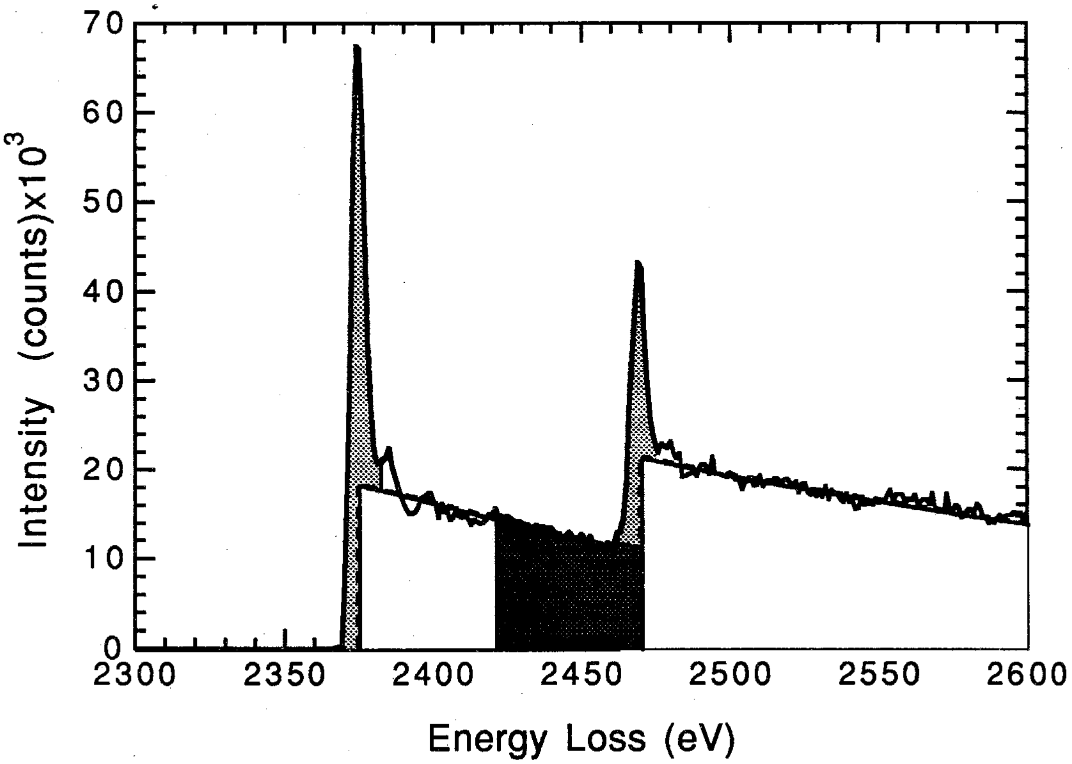

Figure 4.3. $L_{2,3}$ edge for niobium showing the method for isolating and normalizing the white line intensities for the 4*d* transition metals.

shapes for silver, which has no white lines, resemble step functions. A straight line was fit to the background intensity immediately following each white line over a range of approximately 50 eV. This line was then extrapolated into the threshold region and set to zero at energies below that of the white line maximum. The L_2 white line was further isolated by smoothly extrapolating the L_3 background intensity under the L_2 edge. The areas in the white lines were then divided by the area in a normalization window 50 eV in width beginning 50 eV past the L_3 white line onset and summed for each metal as a measure of the number of *d* holes.

This approach is somewhat different from that used in the previous white line studies mentioned in Chapter 1 (Horsley, 1982; Mansour et al., 1984; Morrison et al., 1985). In those studies the white lines were isolated using arctangent functions that connected the zero of intensity at the edge onset to the background immediately following the white line. In addition, those studies normalized the white lines by scaling the background immediately following the white line to unity. This normalization procedure can be somewhat ambiguous, however, when other fine stucture is present at the edge as is the case in some of the 4*d* metals (see Figure 4.2). Normalizing the white lines to the background 50 eV past the edge onset avoids these ambiguities.

A plot of the normalized white line intensity versus 4*d* occupancy is shown in Figure 4.4 The occupancy of the 4*d* states was determined by assuming a valence electron configuration of $4d^{N-1}s^1$, where N is the total number of valence electrons, as this is approximately the configuration in

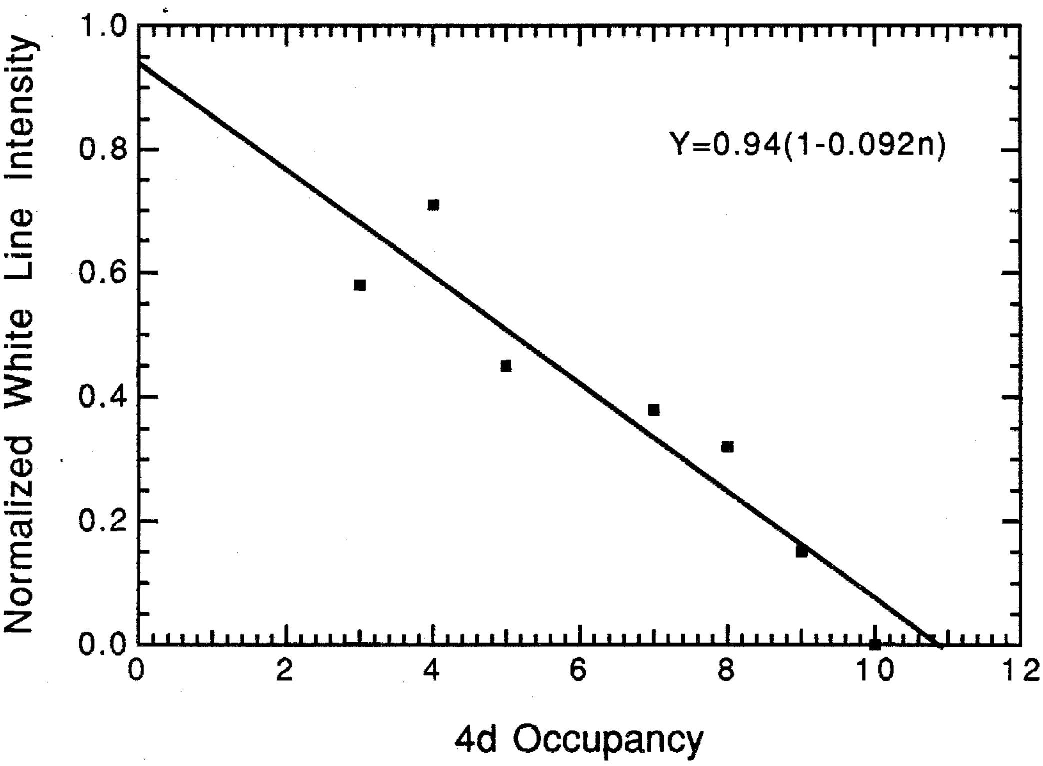

Figure 4.4. Plot of normalized white line intensity versus 4*d* occupancy. The straight line represents a linear fit to the data.

the solid (Pettifor, 1977). A nearly linear correlation was obtained, with a linear fit to the data given by

$$I = 0.094(1-0.092n), \tag{4.1}$$

where I is the normalized white line intensity and n is the *4d* occupancy. That this correlation reflects the *4d* occupancy can be shown by considering the equation given by the linear fit. For this correlation to reflect accurately the occupancy of the *4d* band, it should have a maximum value at n = 0 and should go to zero at n = 10. That is, the correlation should have the form

$$I = K(1-0.1n), \tag{4.2}$$

where K is a constant.

A similar approach was used in the analysis of the *3d* metals and is illustrated for vanadium in Figure 4.5. In this case, the white lines were isolated by modeling the background with a double step function. A straight line was fit to the background immediately following the L_2 white line over a region of approximately 50 eV and was then extrapolated into the threshold region. This line was then modified into a double step of the same slope with onsets occurring at the white line maxima. The ratio of the step heights is chosen as 2:1 in accordance with the multiplicity of the initial states (four $2p_{3/2}$ electrons and two $2p_{1/2}$ electrons). The white line area above this step function was then divided by the area in a

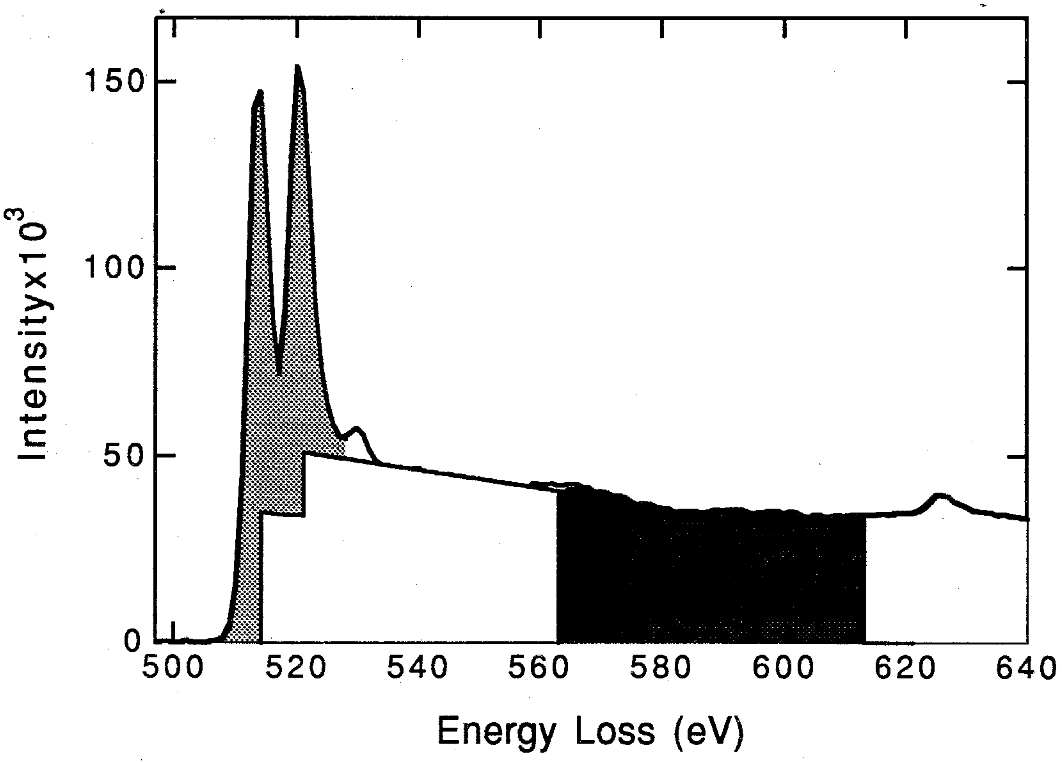

Figure 4.5. $L_{2,3}$ edge for vanadium showing the method for the isolating and normalizing the white line intensities for the *3d* transition metals.

normalization window defined to be 50 eV in width beginning 50 eV past the onset of the *L3* white line. A plot of the normalized white line intensity versus *3d* occupancy assuming a $3d^{N-1}s^1$ valence-electron configuration is shown in Figure 4.6. A nearly linear correlation was obtained, and a least squares fit gave

$$I = 1.06\,(1\text{-}0.094n). \tag{4.3}$$

That the sum of the L_2 and L_3 white line intensities should indeed reflect the number of *d* holes may be seen by considering Equation 2.5. Atomic one-electron calculations by Mattheiss and Dietz (1980) show that the areas A_2 and A_3 under the L_2 and L_3 white lines, respectively, are given by

$$A_3 = K\,R_{2p_{3/2}}\left(\tfrac{2}{5}h_{5/2} + \tfrac{1}{15}h_{3/2}\right) \tag{4.4}$$

$$\text{and} \quad A_2 = K\,R_{2p_{1/2}}\left(\tfrac{1}{3}h_{3/2}\right). \tag{4.5}$$

Here, $h_{3/2}$ and $h_{5/2}$ are the numbers of $j = 3/2$ and $j = 5/2$ *d* holes, $R_{2p_{3/2}}$ and $R_{2p_{1/2}}$ are the radial matrix elements for the excitations of the $2p_{3/2}$ and $2p_{1/2}$ core electrons, and K is a normalization constant. The expressions were evaluated using dipole selection rules while ignoring excitations to outer *s* states, since the matrix elements for these transitions are much smaller than those for excitations to *d* states. In addition, the contributions from the spherical harmonics to the transition strengths

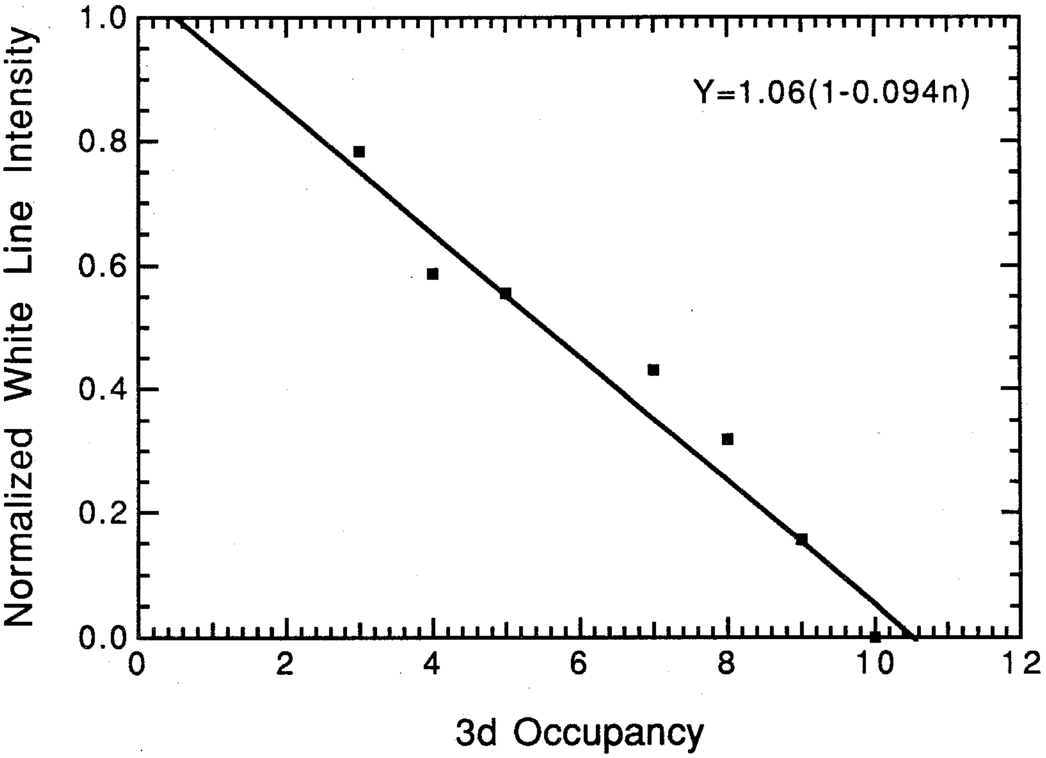

Figure 4.6. Plot of normalized white line intensity versus 3*d* occupancy. The straight line represents a linear fit to the data.

have already been evaluated and account for the coefficients on $h_{3/2}$ and $h_{5/2}$. Taking $R_{2p_{3/2}}$ and $R_{2p_{1/2}}$ to be approximately equal, the sum of the areas under the white lines is given by

$$A_{total} = K\, R_{2p}\, \frac{6}{15} \left(h_{3/2} + h_{5/2}\right) = C\, R_{2p}\, h_{total}. \qquad (4.6)$$

Thus, the total white line area is proportional to the total number of *d* holes.

The correlations in Figures 4.4 and 4.6 are potentially useful for determining changes in outer *d* state occupancy upon alloying or during solid-state phase transformations if corresponding changes in the normalized white line intensity are observed. For example, if an enhancement of 0.05 in the normalized intensity was observed after alloying for a 3*d* metal, the correlation in Figure 4.6 would suggest that about 0.5 electron/atom had left the 3*d* states for that atom species on average. Using Figures 4.4 and 4.6 for such measurements, however, ignores the contribution of the matrix elements to the total intensity. The evaluation of this contribution using atomic one-electron calculations is the subject of the next section.

4.2 Atomic Matrix-Element Calculations

In Figures 4.4 and 4.6 the normalized white line intensity was plotted versus *d*-state occupancy. This normalized intensity, however, is also a function of the radial matrix elements (Equation 4.6) as well as the background intensity to which the white lines are normalized. The significance of these factors should therefore be evaluated before using the correlations in these figures to measure changes in *d* state occupancy.

As mentioned in Chapter 2, atomic, one-electron calculations based on Equation 2.5 have successfully reproduced observed edge shapes for the excitations of core electrons (Manson, 1972; Leapman et al., 1980; Ahn and Rez, 1985). Atomic calculations were therefore also used here to model the normalized white line intensity. Specifically, the calculation involved dividing the white line contribution (excitations to unoccupied 3*d* and 4*d* states) in Equation 2.5 by the background contribution (excitations to continuum states). The initial and final bound states were represented by one-electron wave functions calculated using the Hartree-Slater computer code of Herman and Skillman (Herman and Skillman, 1963). The final continuum wave functions were calculated by directly integrating the Schrödinger equation using the self-consistent potential generated by the Hartree-Slater calculation. These continuum wave functions were then normalized such their amplitude at 40 Bohr radii (essentially infinity) was $\pi^{-1/2}\varepsilon^{-1/4}$ where ε is the continuum energy in Rydbergs (Cowan, 1981). An overview of the calculations, a copy of the continuum wave function code, and typical listings of computer input and output files are given in Appendix 2.

In the limit $q \rightarrow 0$, only dipole transitions contribute to the matrix element in Equation 2.5. At nonzero q, however, higher-order transitions will also contribute. Calculations of $L_{2,3}$ spectra that include these higher order transitions have shown, however, that they become significant only at energies several hundred eV past the edge onset (Leapman et al., 1980;

Okamoto et al., 1991). For this reason, only dipole transitions were considered in the calculations presented here. Furthermore, Equation 2.5 greatly simplifies under these conditions as the matrix element operator is replaced by iq·r. Two straightforward integrations over q and r then determine the total intensity. Since the object of the calculation was to evaluate the *ratio* of the white line to continuum contribution rather than to calculate absolute intensities, the integral over q was ignored. Under these assumptions, the normalized white line intensity is approximately

$$I \approx n_d \frac{|<3d \text{ (or } 4d) | r | 2p > |^2}{\int_{50}^{100} | <\varepsilon d | r | 2p> |^2 \, d\varepsilon}. \tag{4.7}$$

Only transitions to final states with *d* symmetry are shown in this equation, since transitions to states with *s* symmetry were found to be negligible in comparison.

Calculations of the white line matrix elements were carried out using configurations representative of the solid with the addition of a $2p$ core hole (excited-state configuration). The electron removed from the $2p$ was placed in the *d* shell. The resulting configurations were then $2p^5 d^N s^1$. Here, N is the total number of *s* and *d* valence electrons. The continuum matrix elements were also calculated using excited-state configurations. In this case, the Hartree-Slater problem was solved for an ion with a $2p$ core hole, and the continuum wave function was then calculated from the resulting self-consistent potential. In addition, rather than evaluate the denominator of Equation 4.7 by integrating over closely spaced energies from 50 eV to 100 eV, this term was approximated by linear interpolation of the 50 eV and 100 eV matrix elements.

Examples of the calculated wave functions are shown in Figure 4.7 for nickel. Wave functions for the other transition metals are given in Appendix 2. The $2p$ and $3d$ wave functions are those for the atom with the core hole, and the continuum wave function is that for the ion with the core hole. Squares of the matrix elements obtained from these calculations are shown in Figures 4.8 and 4.9. Calculations of the normalized white line intensity using these matrix elements according to Equation 4.7 are shown in Figures 4.10 and 4.11. In the calculations for the $3d$ metals, the continuum window intensity was multiplied by 1.5 to account for the L_2 edge contribution to the experimental normalization windows.

These atomic calculations ignore the fact that the atoms exist in a solid. The effect of the solid may be taken into account approximately by renormalizing the $3d$ and $4d$ wave functions for the various atoms within their appropriate Wigner-Seitz spheres (Hodges et al., 1972). No correction is necessary for the $2p$ wave functions as they already lie well within the Wigner-Seitz radius. White line intensities calculated using these renormalized wave functions are also shown in Figures 4.10 and 4.11. As shown, the magnitude of the correction is small.

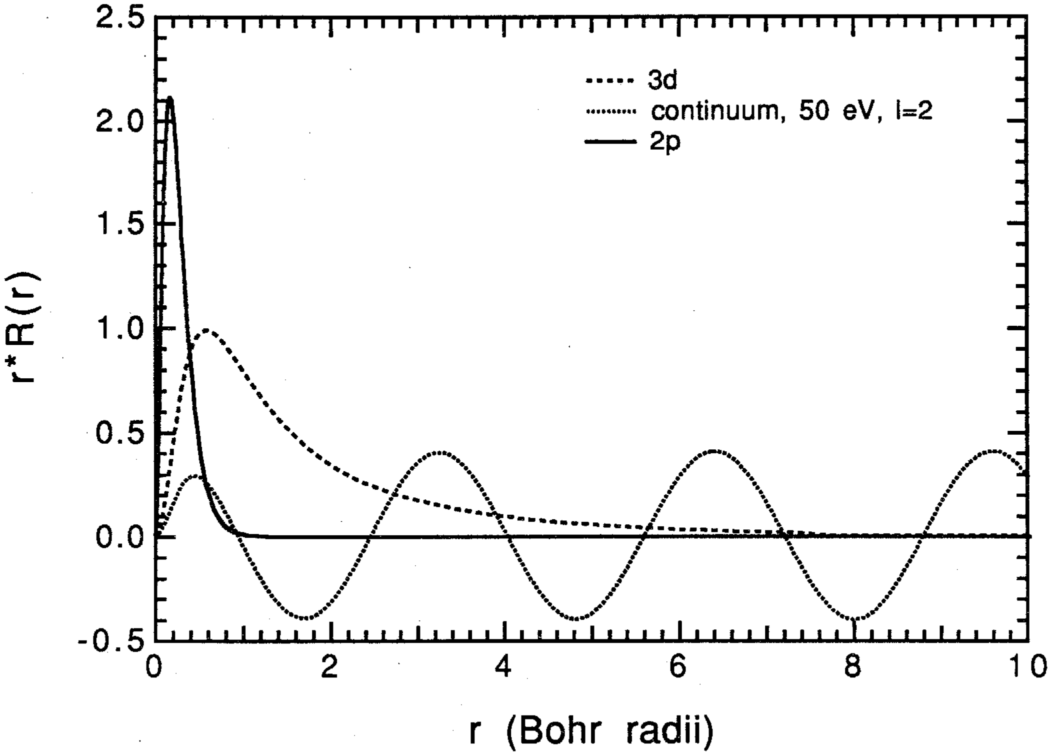

Figure 4.7. Calculated atomic wave functions for nickel.

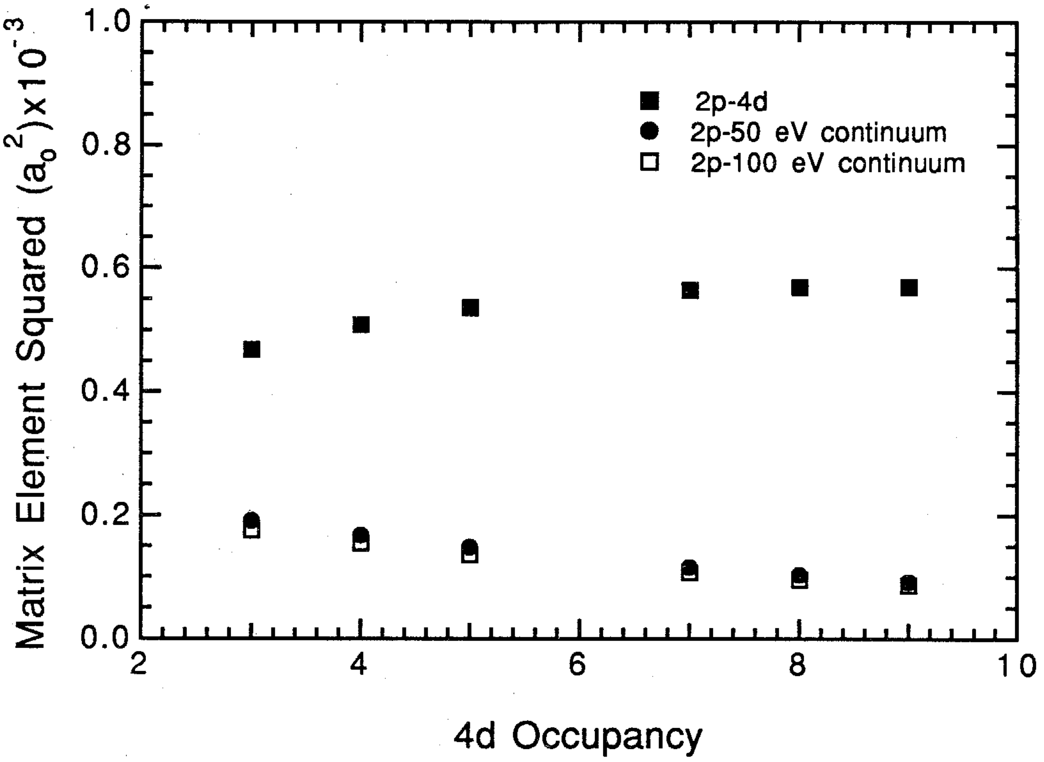

Figure 4.8. Squares of matrix elements for the *4d* transition metals.

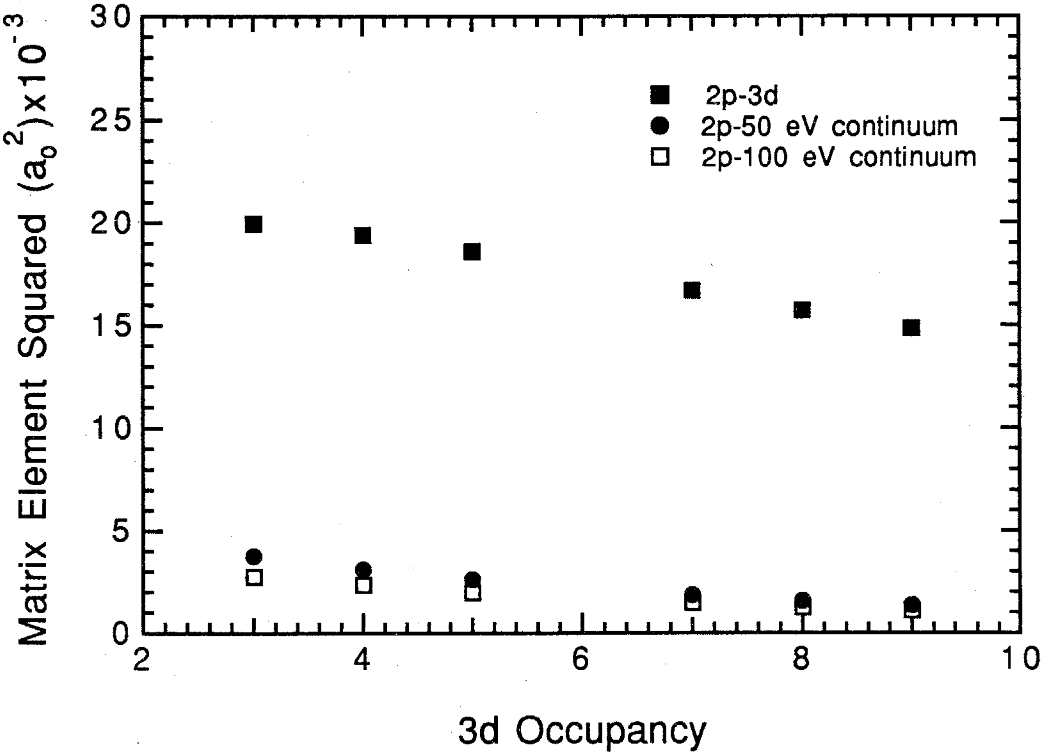

Figure 4.9. Squares of matrix elements for the *3d* transition metals.

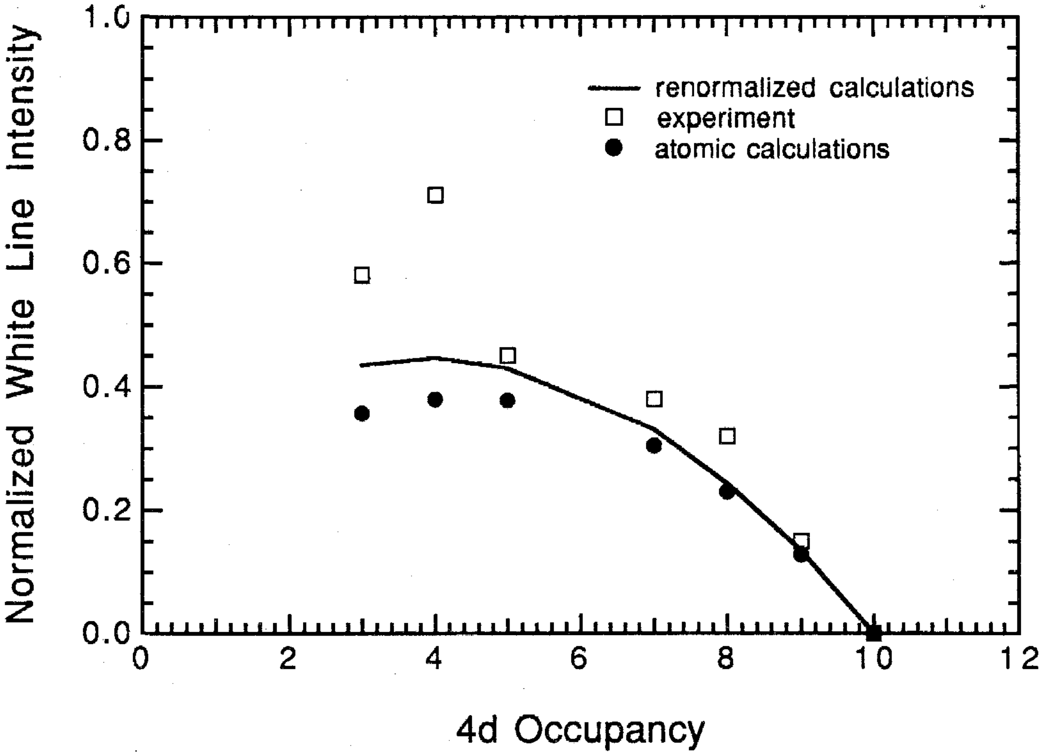

Figure 4.10. Comparison of calculated and experimental white line intensities for the 4*d* transition metals.

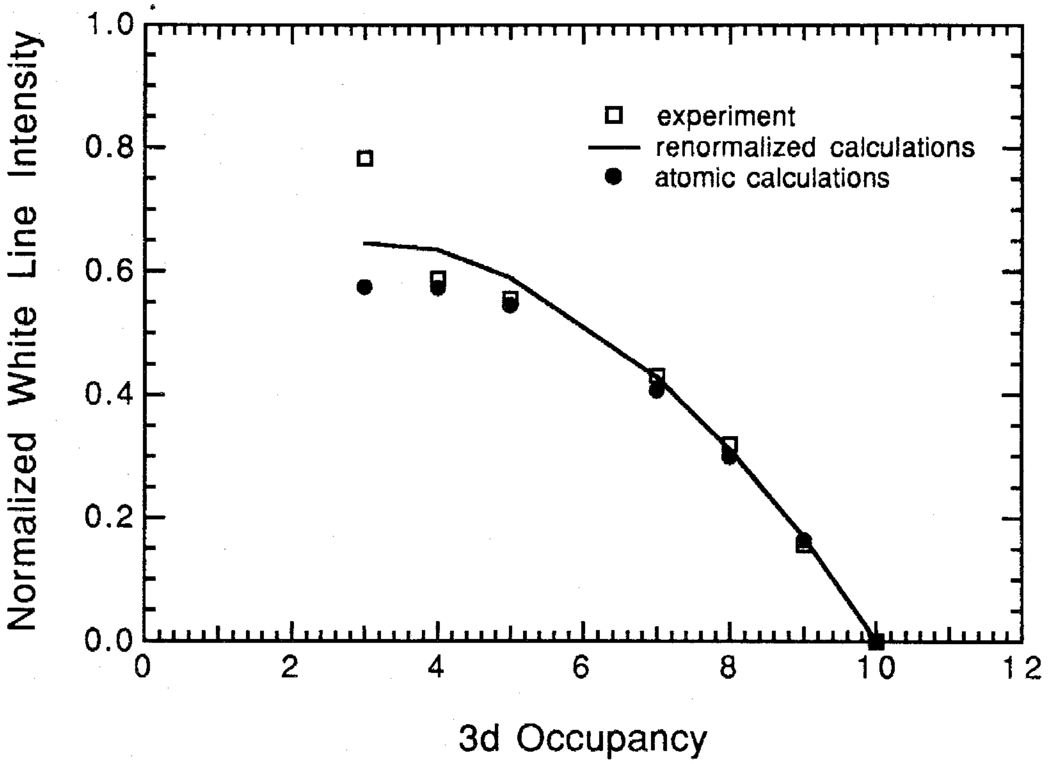

Figure 4.11. Comparison of calculated and experimental white line intensities for the 3*d* transition metals.

4.3 Discussion of Correlations

As shown in Figure 4.11, good agreement between calculations and experiment was obtained for the *3d* metals. Somewhat poorer agreement was obtained for the *4d* metals as shown in Figure 4.10. The poor agreement for the early *4d* transition metals may well be a result of the atomic nature of the calculations. Calculated absorption spectra from Müller et al. (1982) obtained from one-electron, solid-state calculations were in good agreement with the spectra presented here for Nb through Pd.

The agreement obtained for the *3d* metals is good enough to consider correcting the experimental data for the effects of the matrix elements, thereby obtaining a correlation similar to that of Figure 4.6 that is more appropriate for measuring changes in *d* occupancy. The correction involves dividing the experimental data points of Figure 4.6 by the matrix element contributions on the right hand side of Equation 4.7. These matrix element contributions, or correction factors, are shown in Table 4.1 and were calculated using the renormalized wave functions. The correction factor for copper was calculated using a *2p* to *3d* matrix element without a core hole as the *3d* states of copper are already filled.

Metal	Correction Factor
Ti	.092
V	.106
Cr	.118
Fe	.143
Co	.155
Ni	.169
Cu	.172

Table 4.1. Matrix-element correction factors for the 3*d* transition metals.

Figure 4.12 shows the normalized white line intensities for the 3*d* transition metals thus corrected. A linear fit to the data gives

$$I = 10.8\ (1-0.10n) \qquad (4.8).$$

To measure *d*-occupancy changes during alloying using this correlation, one first divides the normalized white line measurements by the appropriate correction factor from Table 4.1 and then applies Equation 4.8. This method further assumes, however, that the appropriate matrix elements do not change during alloying. Atomic calculations suggest that this is a reasonable assumption. For example, as discussed in Chapter 5, an EELS measurement based upon the correlation in Figure 4.6 suggests that

Cu 3*d* states become depleted by about 0.3 electrons/atom when forming amorphous CuZr. Atomic calculations show that the square of the 2*p* to 3*d* matrix element for the partially ionized atom differs by less than 3% from that of the neutral atom.

As mentioned in Chapter 1, previous white line studies that have correlated changes in *d* occupancy with changes in white line intensity have obtained the proportionality only for individual metals using *d* occupancies from band-structure calculations. This approach, however, suffers from uncertainties in isolating small white line intensities for the late transition metals as well as from inaccuracies in the band calculations. The approach presented here avoids these problems, as the proportionalitybetween white line area and *d* occupancy is not solely dependent upon one metal but is determined by analyzing the systematics across the entire series. Furthermore, it is useful to note that the previous studies simply would not allow measurements on copper alloys, since there is no white in the pure metal from which to develop the proportionality. Measurements using the approach developed here on various alloys (including copper alloys) are presented in the next chapter.

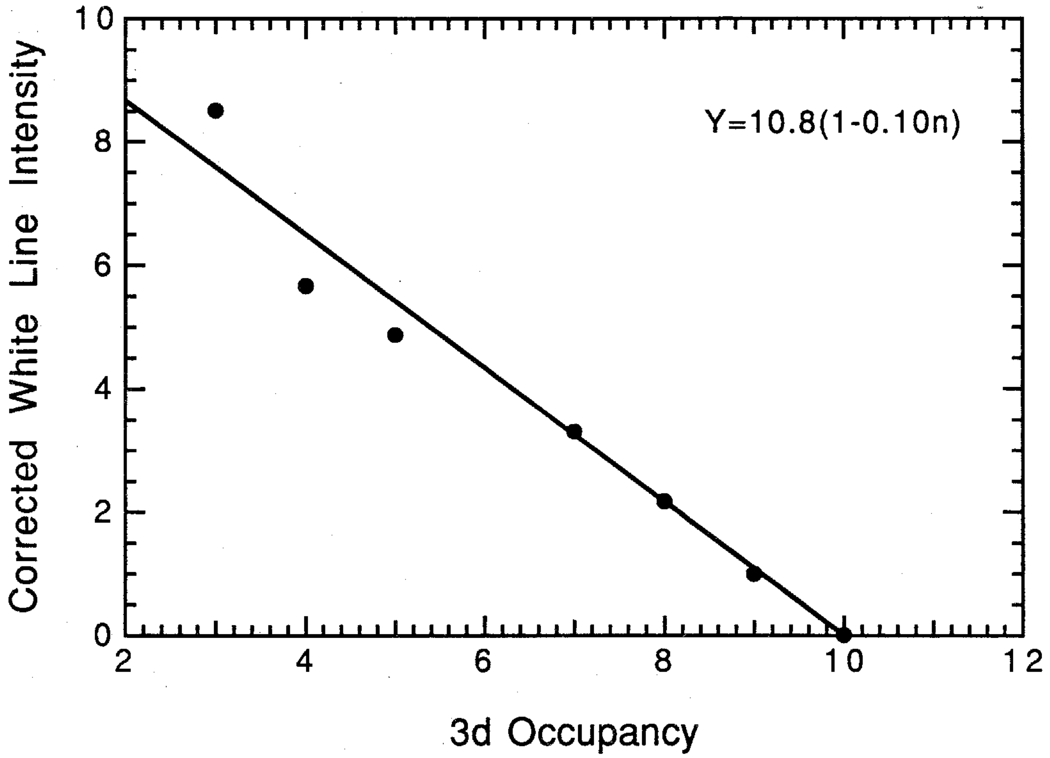

Figure 4.12. Plot of experimental white line intensity corrected for the variations of the matrix elements.

References

Ahn, C. C. and Rez, P., Ultramicroscopy 17, 105 (1985).

Cowan, R. D., The Theory of Atomic Structure and Spectra, University of California Press, Berkeley, p. 515 (1981).

Herman, F. and Skillman, S., Atomic Stucture Calculations, Prentice Hall, Englewood Cliffs (1963).

Hodges, L., Watson, R. E., and Ehrenreich, H., Phys. Rev. B 5 (10), 3953 (1972).

Horsley, J. A., J. Chem. Phys., 76 (3), 1451 (1982).

Leapman, R. D., Rez, P., and Mayers, D. F., J. Chem. Phys. 72 (2), 1232 (1980).

Manson, S. T., Phys. Rev. A 6, 1013 (1972).

Mansour, A. N., Cook, J. W., and Sayers, D. E., J. Phys. Chem. 88, 2330 (1984).

Mattheiss, L. F. and Dietz, R. E., Phys. Rev. B 22 (4), 1663 (1980).

Morrison, T. I., Brodsky, M. B., and Zaluzec, N.J., Phys. Rev. B 32 (5), 3107 (1985).

Müller, J. E., Jepsen, O., and Wilkins, J. W., Solid State Comm. 42(5), 365 (1982).

Okamoto, J. K., Pearson, D. H., Ahn, C. C., and Fultz, B., in Applications of Transmission EELS in Materials Science, The Metallurgical Society, Warrendale, PA, eds. M. M. Disko, C. C. Ahn, and B. Fultz (in press).

Pettifor, D. G., J. Phys. F 7 (4), 613 (1977).

Chapter 5 White Lines in Transition-Metal Alloys

In this chapter the results of the previous chapter are used to infer changes in the $3d$ occupancy at transition metal atoms in a number of alloys. Spectra obtained for these alloys as described in Chapter 3 are presented here and discussed in §5.1. A simple band theory of alloying between transition metals is discussed in §5.2 in conjunction with the measurements. A summary and conclusions are presented in §5.3.

5.1 Absorption Spectra from Alloys

A number of alloys were investigated in this study. Copper alloys were emphasized because their $3d$ band is full in the pure metal. Any enhancements of the white lines that were due to alloying would then be easily discernible. Iron-cobalt alloys of various concentrations were also studied, as iron d occupancy measurements were available for comparison from Mössbauer spectrometry studies. Several nickel alloys were also investigated.

Data obtained from amorphous CuZr and amorphous CuTi obtained with the parallel acquisition spectrometer are shown in Figures 5.1 and 5.2. A spectrum from pure Cu (dotted line) is shown in each graph for reference. The Cu spectra have been scaled to match those of the alloys beyond the L_2 white line. The enhancements of the white lines observed in the alloys indicate that some electrons have left Cu $3d$ states on average upon alloying. By determining the change in normalized white line intensity in the alloy (using the Cu spectrum to isolate the white lines) and applying Equation 4.3, one finds that approximately 0.3 electron/atom

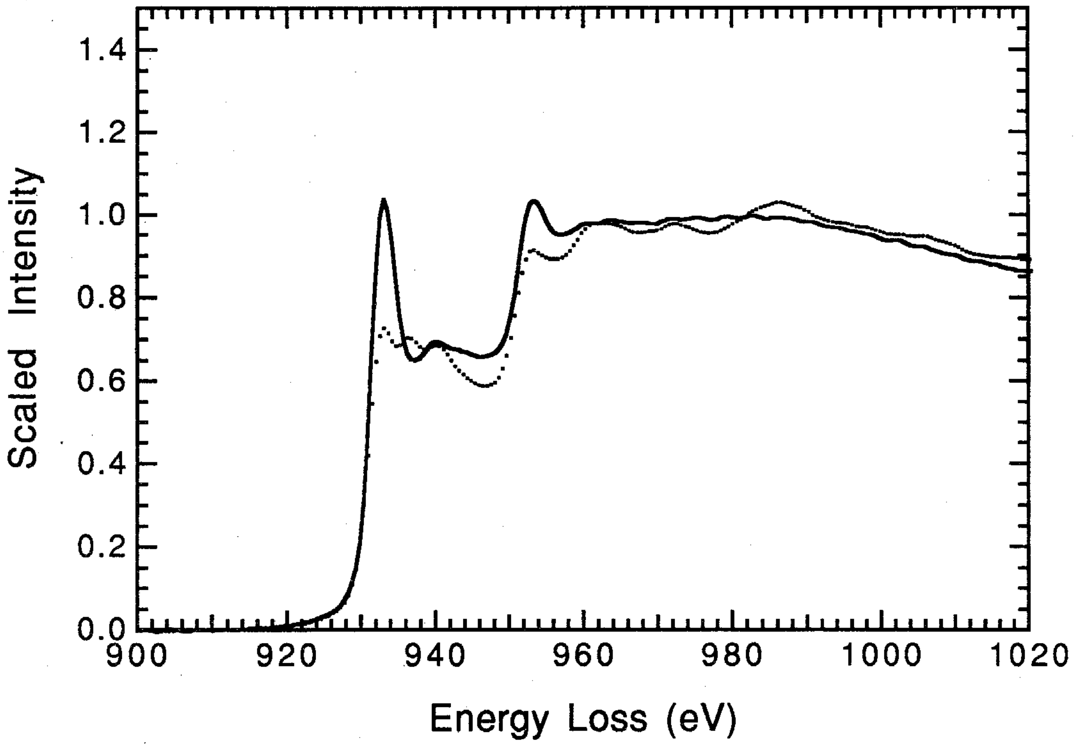

Figure 5.1. Copper $L_{2,3}$ edge for amorphous CuZr and pure Cu (dotted line).

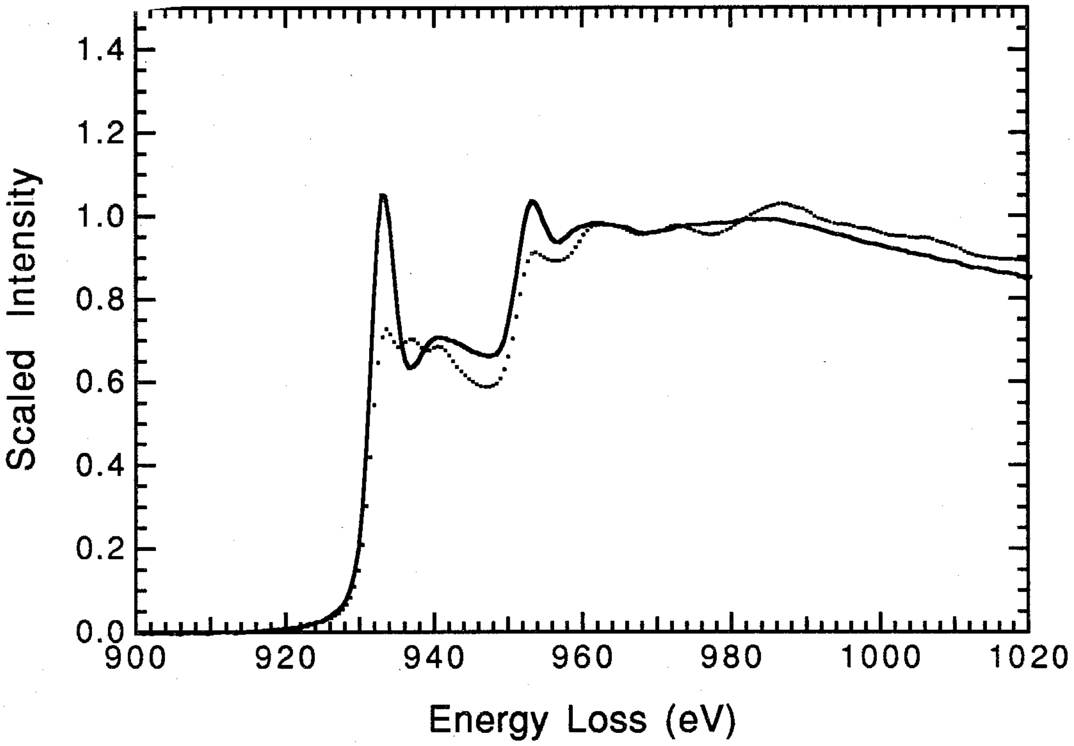

Figure 5.2. Copper $L_{2,3}$ edge for amorphous CuTi and pure Cu (dotted line).

has left the Cu 3*d* states in both alloys. The background structure in the pure Cu spectrum leads to some ambiguity in the appropriate scaling, however. Shifting the Cu spectrum up or down slightly by amounts representative of the structure variations yields an uncertainty of ± 0.1 electron/atom. In addition, applying the correction scheme of Table 4.1 and Equation 4.8 reduces these numbers by 47%. In either case, however, the measurement compares favorably with local density-of-states calculations of Manh et al. (1987). Their tight-binding calculations for amorphous CuZr predict a depletion of .31 electron/atom from copper 3*d* states that is due to alloying.

Data obtained from disordered fcc CuAu, CuPd, and CuPt are shown in Figures 5.3-5.5. There appears to be little difference between the alloy and the pure Cu spectra at the thresholds, although the scaling is again somewhat uncertain because of variations in the background structure of the spectra. The small enhancment in the L_3 white line in the CuPt spectrum corresponds to a depletion of about 0.05 electron/atom using Equation 4.3. It is worthwhile to note that density-of-states calculations for CuAu by Kokko et al. (1990) show the *d* band in the alloy to be filled. Also, calculations for disordered fcc CuPd by Winter et al. (1986) show the local density of *d* states at copper atoms to be full.

Data obtained from amorphous $Cu_{10}Zr_7$ and pure copper (dotted line), using the serial detection spectrometer, are shown in Figure 5.6. White lines were again observed in the alloy spectrum, indicating that the copper 3*d* states are slightly depleted because of alloying. Using Equation 4.3, this increased white line intensity corresponds to a reduction of

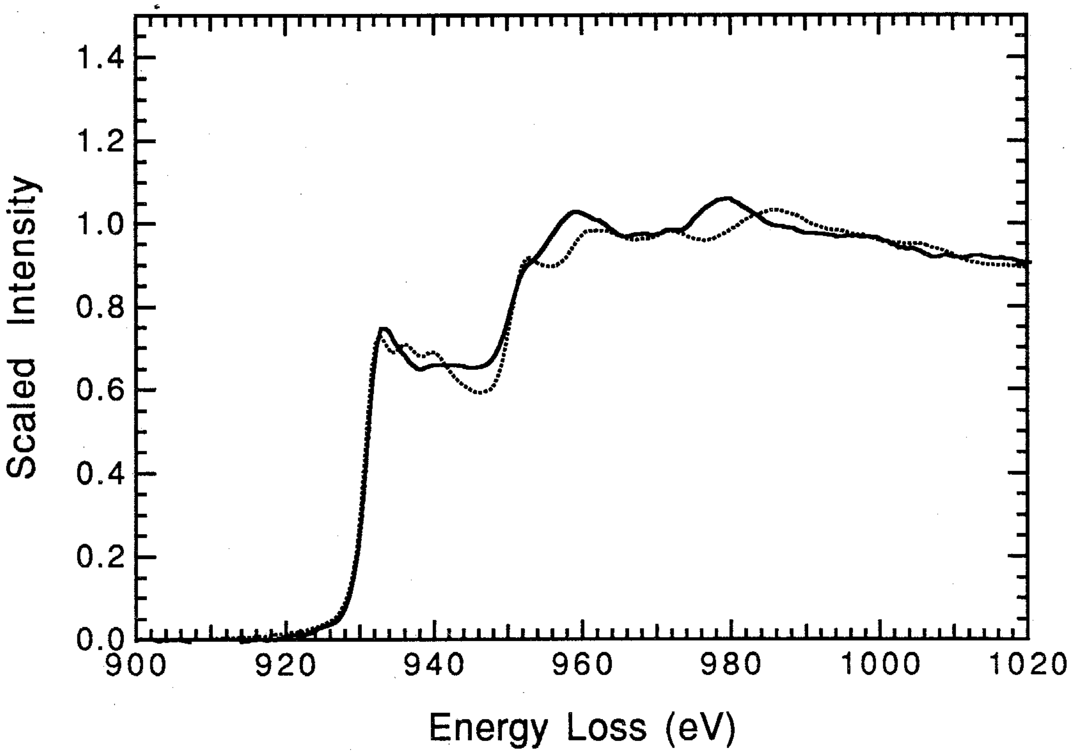

Figure 5.3. Copper $L_{2,3}$ edge for disordered fcc CuAu and pure Cu (dotted line).

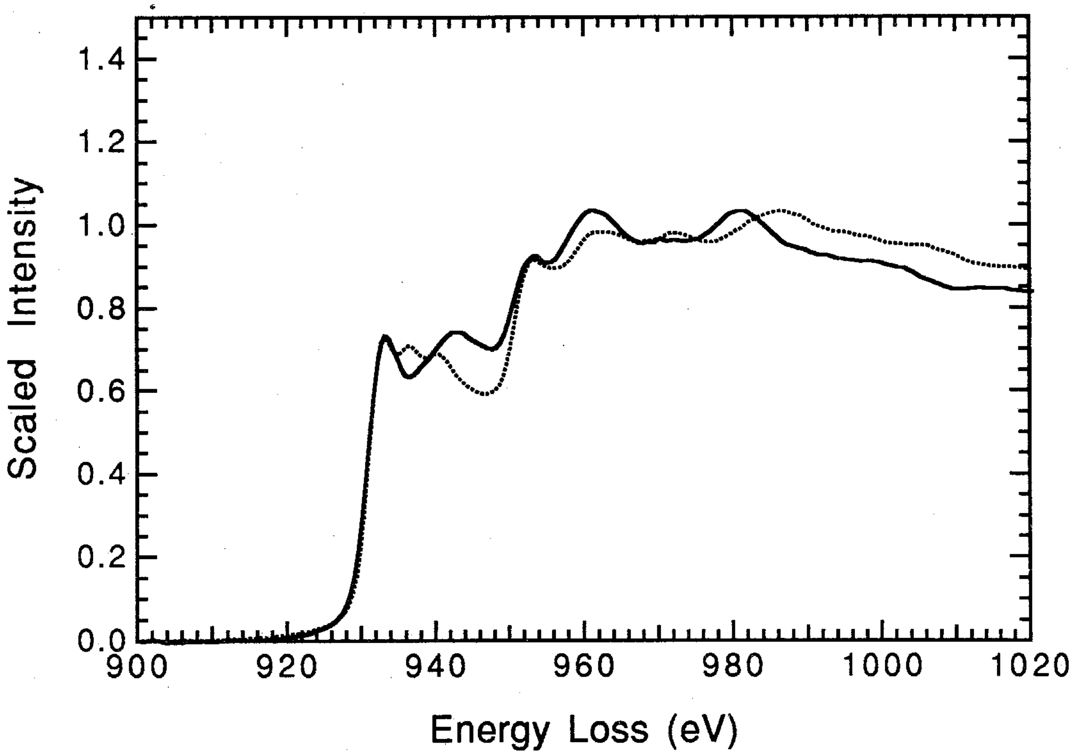

Figure 5.4. Copper $L_{2,3}$ edge for disordered fcc CuPd and pure Cu (dotted line).

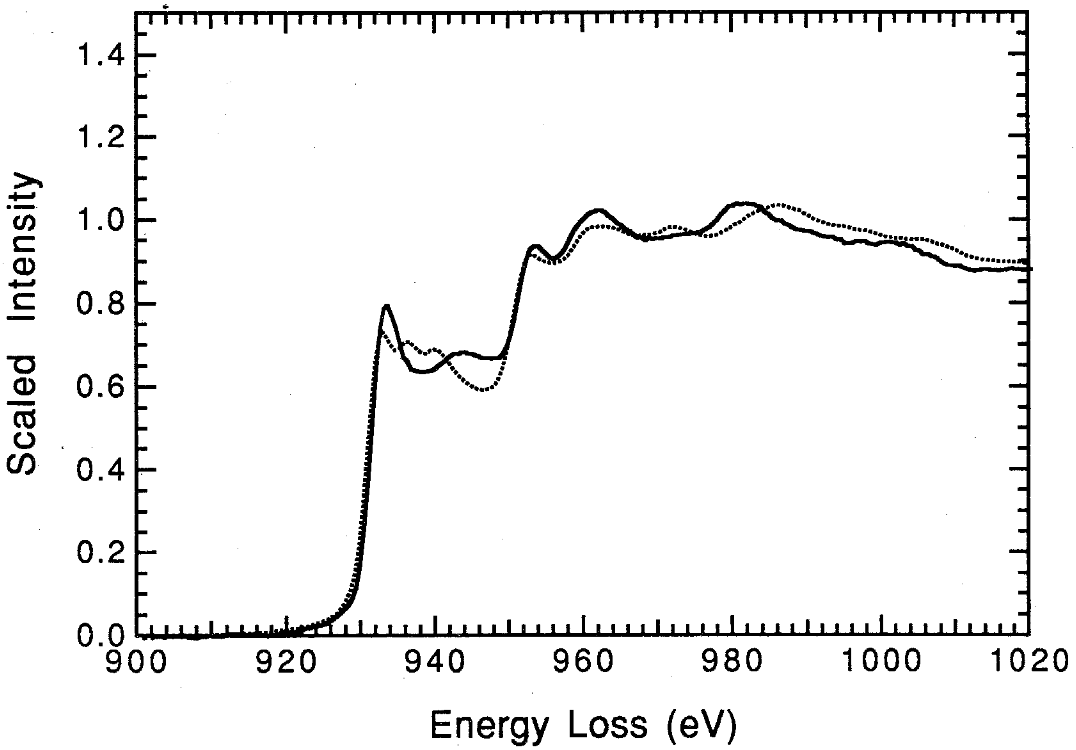

Figure 5.5. Copper $L_{2,3}$ edge for disordered fcc CuPt and pure Cu (dotted line).

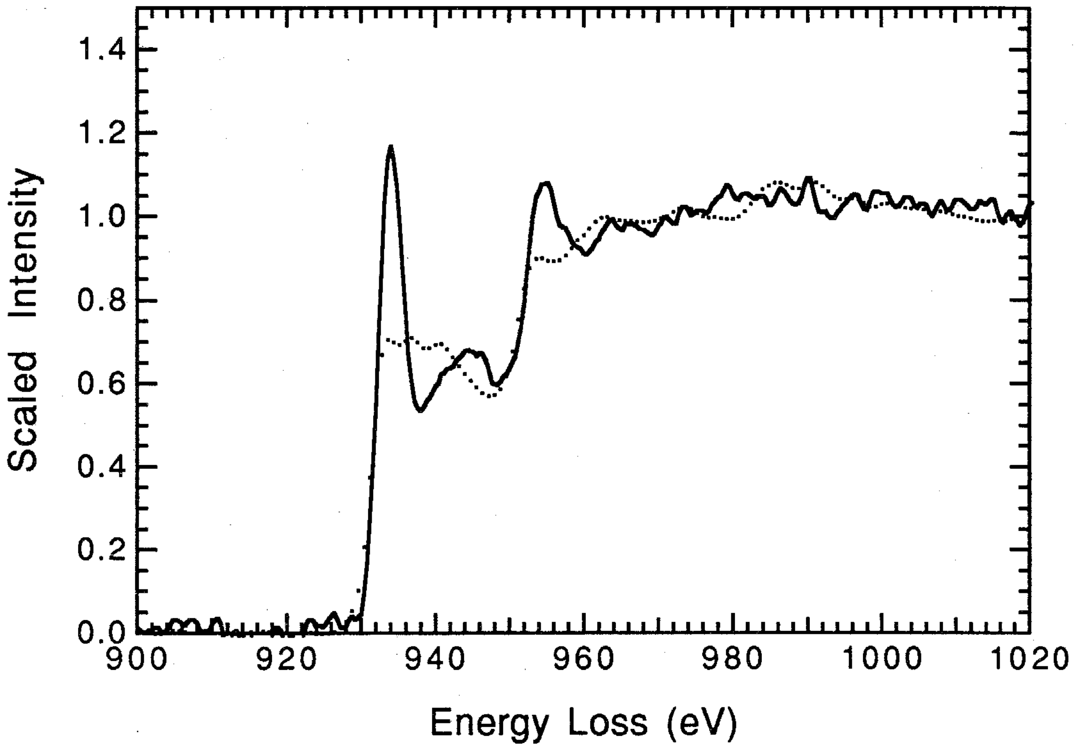

Figure 5.6. Copper $L_{2,3}$ edge for amorphous $Cu_{10}Zr_7$ and pure Cu (dotted line).

approximately 0.3 ± 0.1 electron/atom. The uncertainty in the measurement is again due to the uncertainty in scaling the Cu spectrum. Application of the matrix-element correction reduces this number by 47%.

Data were also obtained from crystalline $Cu_{10}Zr_7$. After obtaining a spectrum from the amorphous sample, the sample was heated in the electron microscope until it crystallized, and another spectrum was recorded from the same region. These data are presented in Figure 5.7. The small decrease in the white line intensity in the crystalline material (dotted spectrum) corresponds to an addition of 0.1 electron/atom compared to the amorphous alloy using Equation 4.3. For comparison, the crystallization enthalpy measured by DSC was 1.3 kcal/mole.

In addition, data were obtained from disordered and ordered Ni_3V using the serial-detection spectrometer. Again, the ordering treatment was induced by heating the sample in the electron microscope, and spectra were obtained from the same region of the specimen before and after ordering. Several spectra were recorded and processed individually in each case. A typical spectrum for disordered Ni_3V is shown in Figure 5.8 with a pure Ni (dotted) spectrum for reference. An average decrease in the white line intensity was found, corresponding to an addition of 0.05 ± 0.2 electron/atom to Ni 3*d* states through Equation 4.3. The uncertainty represents the sum of the scatter in the Ni_3V and Ni data. The matrix-element correction reduces this number by 45%. Typical spectra obtained before and after the heat treatment in the microscope are shown in Figure 5.9. The dotted line represents the spectrum from the ordered alloy. An average increase in the white line intensity was found compared to the

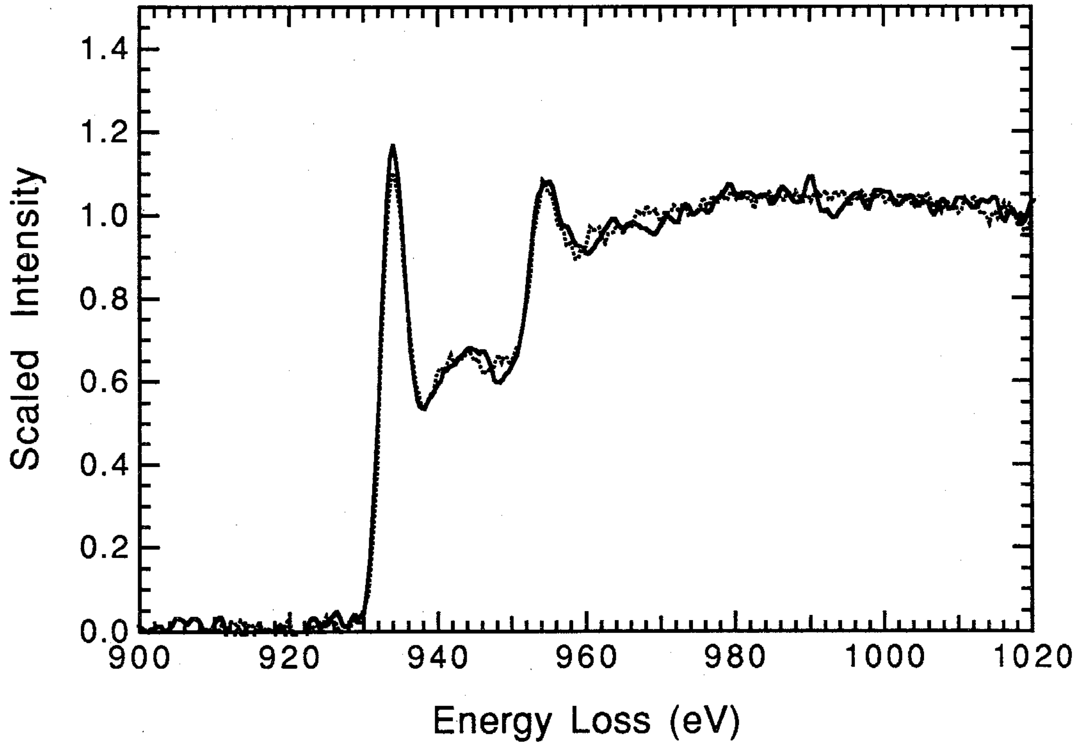

Figure 5.7. Copper $L_{2,3}$ edge for amorphous $Cu_{10}Zr_7$ and crystalline $Cu_{10}Zr_7$ (dotted line).

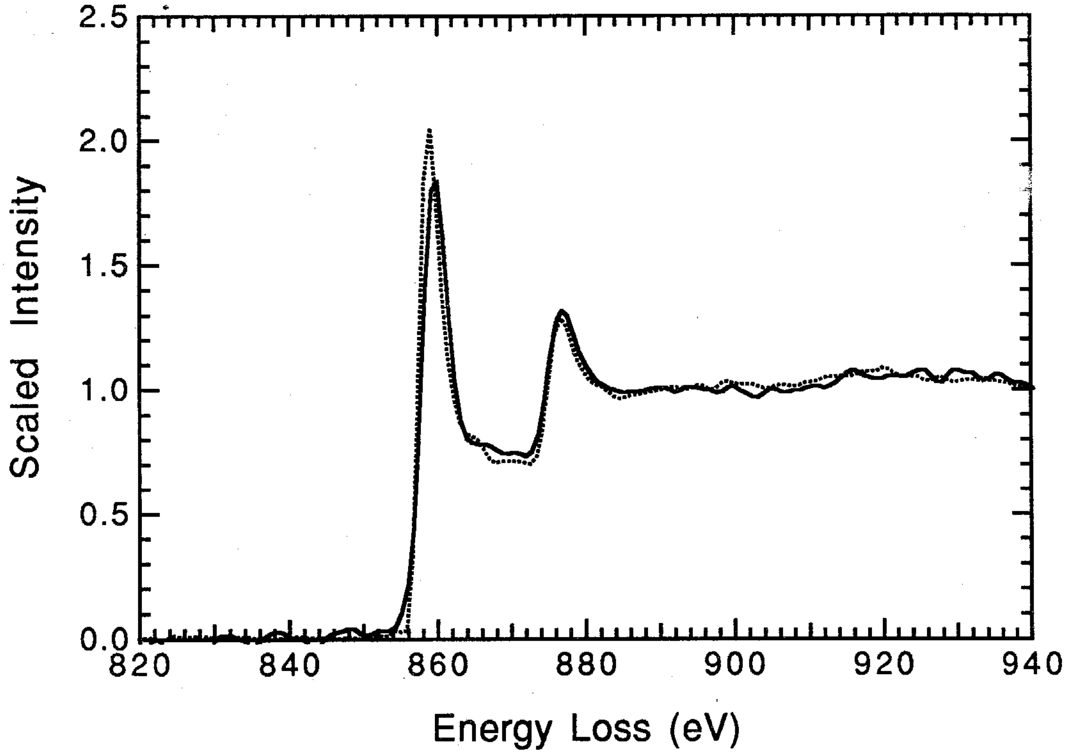

Figure 5.8. Nickel $L_{2,3}$ edge for disordered fcc Ni_3V and pure Ni (dotted line).

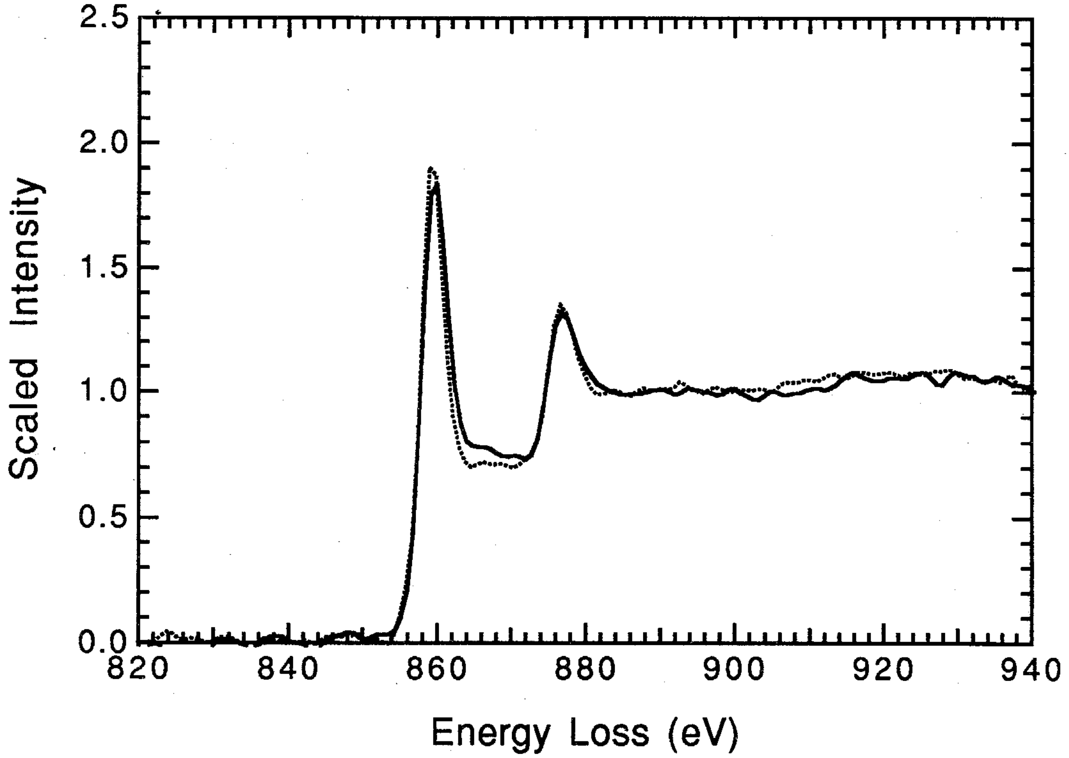

Figure 5.9. Nickel $L_{2,3}$ edge for disordered fcc Ni_3V and ordered Ni_3V (dotted line).

disordered alloy, corresponding to a depletion of 0.05 ± 0.2 electron/atom using Equation 4.3. For comparison the ordering enthalpy measured by DSC was 1.0 kcal/mole.

Data were also obtained from disordered Fe-Co alloys with Co concentrations of 9.4%, 30%, 50%, and 70%. Five spectra were obtained from each alloy sample as well as from pure Fe. Typical spectra for the disordered 50% alloy and pure Fe (dotted line) are shown in Figure 5.10. Spectra for the other alloy concentrations appear similar to that shown in Figure 5.10. Average values for the measured electron transfers using Equation 4.3 are presented in Table 5.1 along with Mössbauer spectrometry measurements of Hamdeh et al. (1989) and linear combination of atomic orbitals (LCAO) calculations of Richter and Eschrig (1988). The uncertainties in the EELS measurements reflect the scatter in the white line intensities observed for each set of spectra. General agreement is observed, given the uncertainty in the EELS measurements. In addition, two spectra were obtained from the 50% alloy after an ordering heat treatment in microscope. Typical spectra for the disordered and ordered (dotted line) 50% alloys are shown in Figure 5.11. An average increase in white line intensity was observed compared to the disordered alloy, corresponding to a depletion of 0.05 ± 0.3 electron/atom, using Equation 4.3. The matrix-element correction reduces this number by 35%. For comparison, the ordering enthalpy measured by DSC was 0.9 kcal/mole.

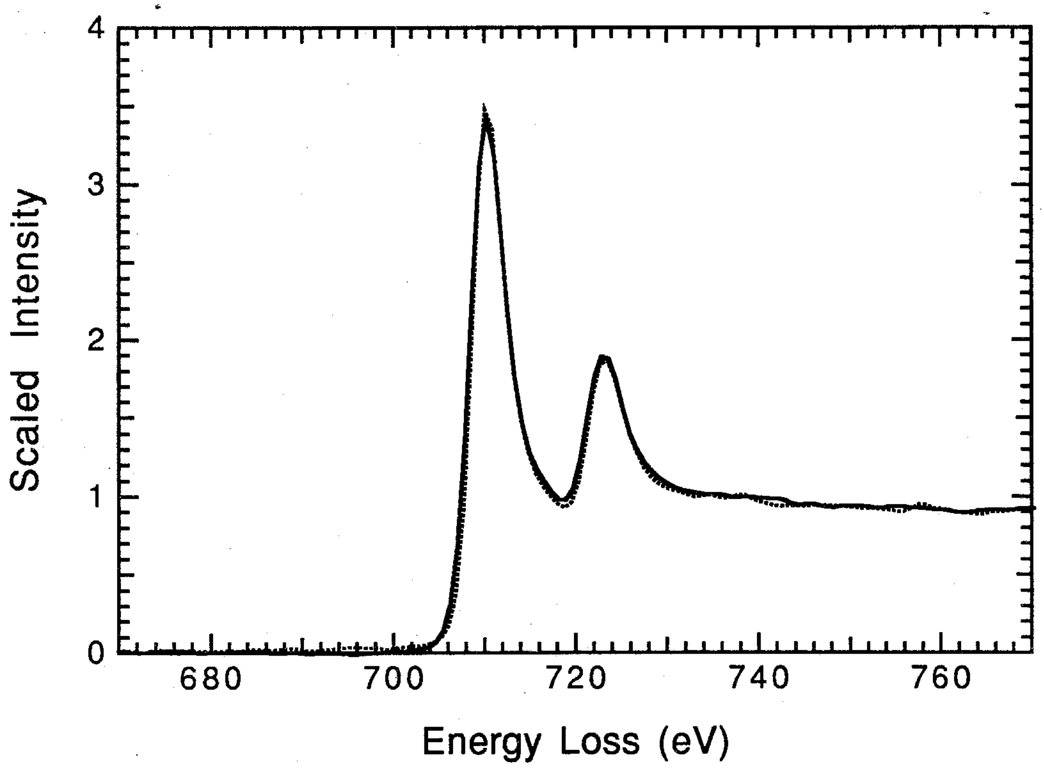

Figure 5.10. Iron $L_{2,3}$ edge for disordered bcc FeCo and pure Fe (dotted line).

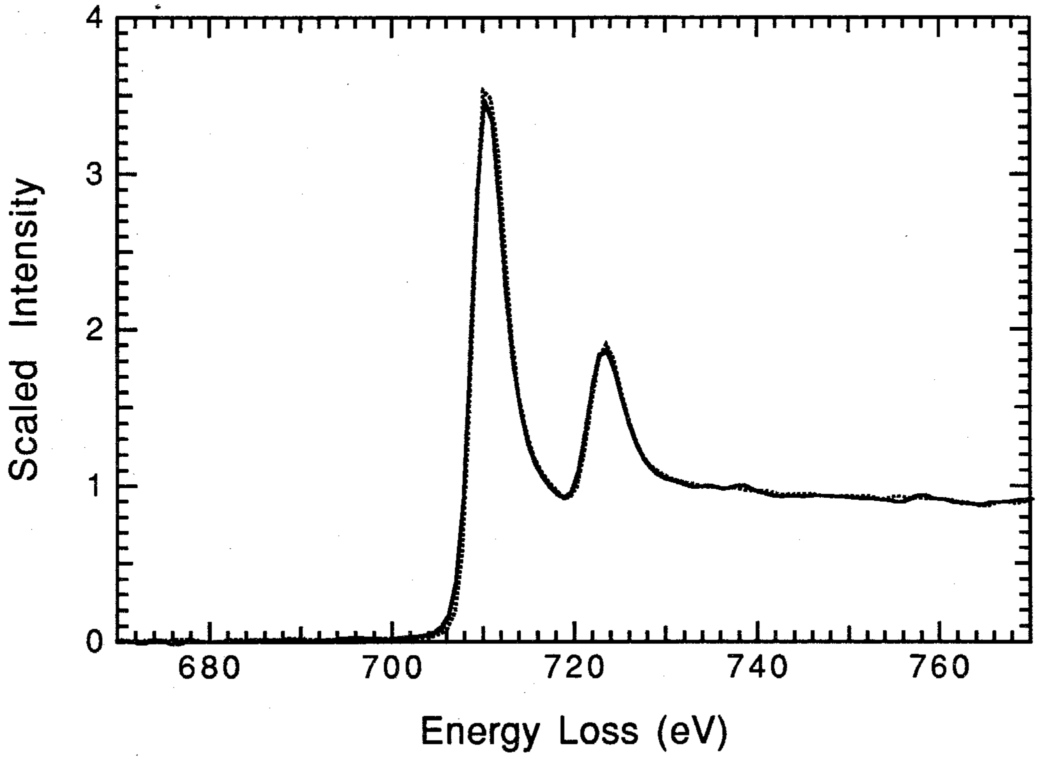

Figure 5.11. Iron $L_{2,3}$ edge for disordered bcc FeCo and ordered FeCo (dotted line).

% Co	EELS (uncorrected)	Hamdeh et al.	Richter et al.
9.4%	–.3 ± .4	+.07	——
30%	–.4 ± .4	+.20	+.1
50%	–.2 ± .4	+.12	+.1
70%	–.4 ± .4	+.04	+.1

Table 5.1. Changes in Fe *d* occupancy in Fe-Co alloys from EELS measurements, Mössbauer spectrometry measurements, and LCAO calculations. Applying the matrix element correction reduces the EELS measurements by 35%.

Lastly, data were obtained from Ni_3Al, using the parallel acquisition spectrometer. This spectrum is shown in Figure 5.12 with a Ni spectrum (dotted line) for reference. A small enhancement in the intensity was observed in the L_3 white line as well as in the shoulder of the white line. Ignoring the shoulder, the increased intensity corresponds to a depletion of 0.1 electron/atom from Ni 3*d* states. Including the shoulder, the value is 0.2 electron/atom. The matrix-element correction reduces these numbers by 45%. No published experimental or theoretical data were available for comparison.

These results show that EELS is sensitive to *d*-occupancy changes that result from alloying. Furthermore, the approach presented in Chapter 4 allows a quantitative measurement of these *d*-occupancy changes. For the alloys examined here, the measured changes in *d* occupancy upon alloying were in agreement with data from the literature

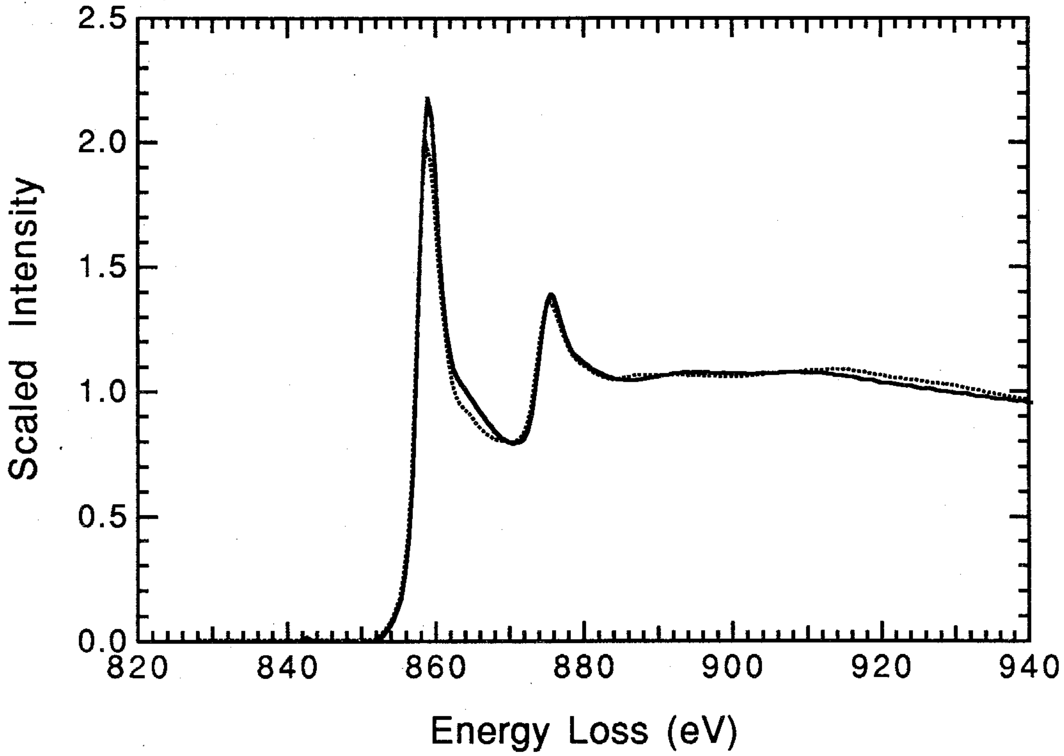

Figure 5.12. Nickel $L_{2,3}$ edge for Ni_3Al and pure Ni (dotted line).

where available. In addition, this technique may be useful for detecting *d*-occupancy changes during phase transformations in favorable circumstances. For the alloys investigated here, the *d*-occupancy changes due to crystallization and ordering were small, as were the corresponding crystallization and ordering enthalpies.

It is worthwhile to restate that these measurements reflect changes in electron densities *local* to a given atom species because the 2*p* electrons are atomiclike and the outer *d* states are tightly bound to a given atom. In addition, the measurements were made on the assumption that the 2*p* to 3*d* (or 4*d*) matrix elements remained constant during alloying. As mentioned in Chapter 4, atomic calculations suggest that this is a reasonable assumption for small *d*-occupancy changes.

It should also be noted that other techniques for probing *d*-electron densities may yield measurements different from those obtained by EELS. In ultraviolet photoelectron spectroscopy, for example, the relevant matrix elements clearly depend upon the entire spatial extent of the *d*-electron wave functions. The wave functions presented in Appendix 2, however, show that the 2*p* to 3*d* (or 4*d*)matrix elements of importance in white line studies depend only upon the overlap in the core region of the atom.

5.2 Heats of Formation and *d* Electrons

Aside from detailed band-structure calculations, there are two well-known models for predicting the heats of formation of alloys. The one that has received perhaps the most attention since its introduction is the semiempirical "macroscopic-atom" model of Miedema et al. (1973, 1975).

In this model, an alloy is regarded as being composed of Wigner-Seitz cells of the elemental metals A and B. There are two terms that contibute to the heat of formation in this model. The first is attractive and results from a flow of charge that is due to the difference in work functions of the metals. The second is repulsive and arises from the need to remove the discontinuity in the charge density across the Wigner-Seitz boundary. As noted by Pettifor (1987), the model lacks quantum mechanical justification and requires judicious choices for values of the work function and charge density terms for its predictive success.

An alternative model that has received considerable attention for transition metals is the rectangular *d* band model of alloying due to Pettifor (1978, 1979, 1983) based on the rectangular *d* band treatment of cohesion by Friedel (1969). Friedel suggested that in evaluating the cohesive energy that was due to the broadening of atomic *d*-electron energy levels into energy bands, one could approximate the actual *d*-electron density of states by a rectangular density of states as shown in Figure 5.13. The width and height of this rectangular density of states are given by W and 10/W, respectively, since there must be 10 total available states for *d* electrons. The lowest lying and highest lying of these energy-band states are generally called "bonding" and "antibonding," respectively, because of their relative positioning with respect to the (assumed degenerate) atomic energy level, E_d. The cohesive energy per atom in this simple band picture may be calculated by subtracting the total energy of the *d* electrons in the isolated atom from the total energy of the *d* electrons in the energy band of the solid. Assuming that the rectangular *d* band is

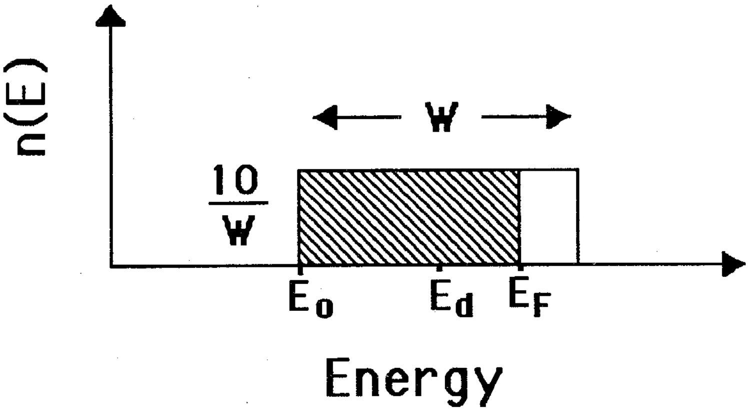

Figure 5.13. Rectangular energy band in the Friedel treatment of cohesion.

centered about the atomic energy level, E_d, one finds

$$E_{coh}\,(\text{per atom}) = \int_{E_0}^{E_F} n(E)\,E\,dE \; - \; N_d\,Ed \; = \; -\frac{N_d\,W}{20}\,(10 - Nd), \quad (5.1)$$

where
$$E_0 = E_d - \frac{W}{2} \;\text{ and }\; E_F = E_0 + \frac{N_d\,W}{10}. \quad (5.2)$$

A plot of the cohesive energies for the *4d* transition metals taken from Kittel (1976) are shown in Figure 5.14 along with those predicted by the Friedel model. An average band width of 7.5 eV for the *4d* series (Pettifor, 1977) was used to generate the solid curve. As shown in Figure 5.14, the Friedel treatment reproduces quite well the empirical trend in both shape and magnitude.

Although the actual *d* densities of states in transition metals are not rectangular, the integrated densities of states as a function of energy are nearly linear (Moruzzi et al., 1978), such as would be obtained through a rectangular band treatment. This agreement between the integral density of states accounts for the success of the rectangular band treatment. Although this model neglects cohesion resulting from the outer *s* electrons as well as the repulsive forces that clearly must be present to prevent the metallic lattice from collapsing, it nevertheless provides good motivation for addressing the *d* electrons in models of alloying between transition metals.

The Pettifor model for alloying between transition metals extends the Friedel treatment by joining the energy bands for the individual

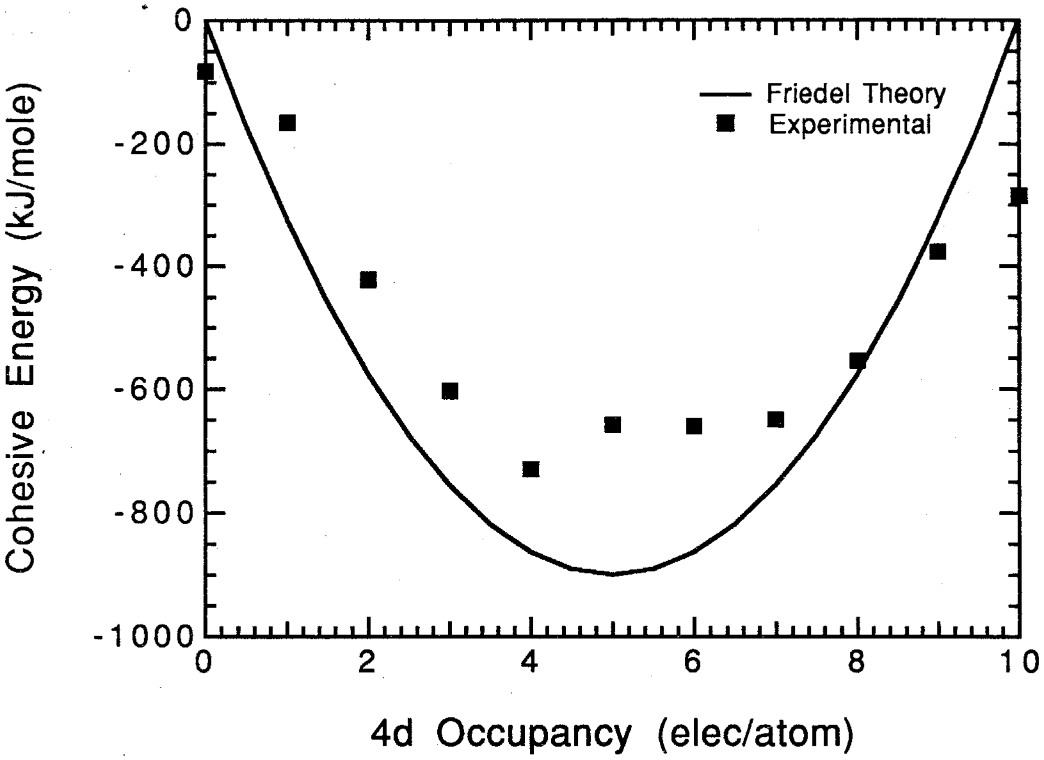

Figure 5.14. Cohesive energies for the *4d* transition metals. Predictions from the Friedel model are shown by the solid curve.

metals into a common alloy band as illustrated in Figure 5.15. Here E_A and E_B are the atomic energy levels that split into bands of width W_A and W_B respectively. The number of *d* electrons in each metal is given by N_A and N_B. When atoms in the metals mix to form a common rectangular band, the partial densities of states of the individual metal bands must deform to avoid unphysically large electron transfers when filling the common band. Pettifor has suggested skew rectangular partial densities of states as shown. To fix the parameter "a" that determines the slope of the partial density of states shown in Figure 5.15, Pettifor requires that E_A and E_B lie at the centers of gravity of their respective partial bands in the alloy. This constraint gives

$$a = \frac{3\Delta E}{W_{AB}}, \tag{5.3}$$

where $\Delta E = E_B - E_A$. The value of W_{AB} may be determined by requiring the second moment of the total density of states to be equal before and after alloying. This constraint gives

$$W^2{}_{AB} = \frac{1}{2}(W^2{}_A + W^2{}_B) + 3\Delta E^2. \tag{5.4}$$

The *d*-electron contribution to the alloy heat of formation is given by the total electronic energy in the alloy band minus the total electronic energy in the individual metal bands. These integrations yield

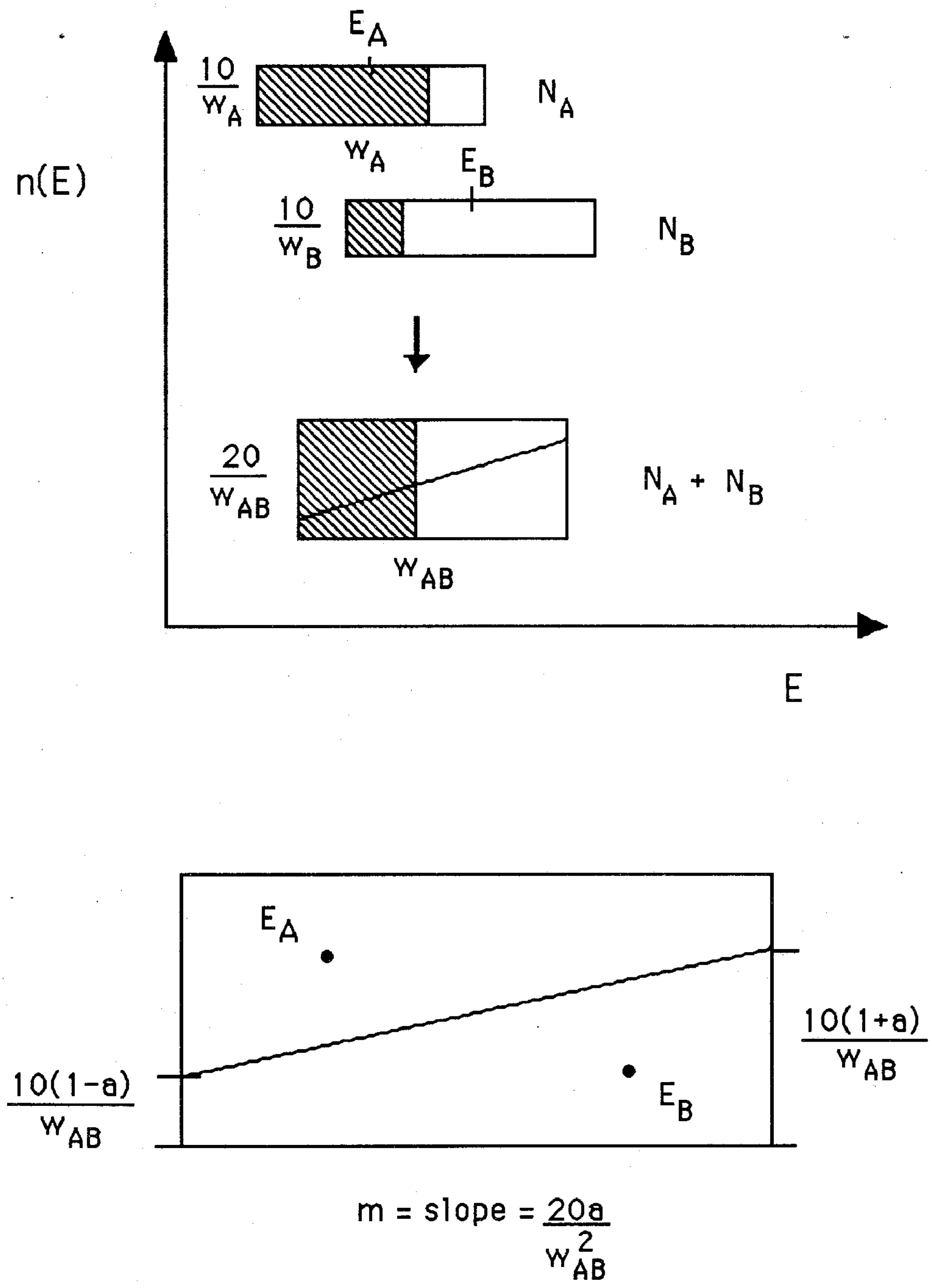

Figure 5.15. Rectangular energy band picture for alloying between two transition metals.

$$\Delta H = -\frac{1}{4}(\Delta N)(\Delta E) - \frac{1}{20}N_{ave}W_{AB}(10 - N_{ave}) + \frac{1}{40}N_B W_B(10\text{-}N_B) + \frac{1}{40}N_A W_A(10\text{-}N_A), \qquad (5.5)$$

where N_{ave} is the average number of *d* electrons and $\Delta N = N_B - N_A$. Note that this expression is independent of the form of the partial densities of states. This is expected because the total alloy density of states that determines the band energy is rectangular.

The electron transfer between the bands may be obtained by integrating the partial density of states for atom A in the final band and subtracting N_A. This gives

$$\Delta Q_A = \frac{\Delta N}{2} + \frac{3}{10}N_{ave}(10 - N_{ave})\frac{\Delta E}{W_{AB}}. \qquad (5.6)$$

Although Equations 5.5 and 5.6 indicate that ΔH and ΔQ are both proportional to ΔN and ΔE, they also show that ΔH cannot be written as a simple function of ΔQ. Thus, although one might expect ΔH to scale roughly with ΔQ, the equations do not suggest a simple proportionality.

Values of ΔH and ΔQ were calculated, using Equations 5.5 and 5.6 for some of the alloys discussed in the previous section. The results of these calculations are shown in Table 5.2. Energies are given in eV, heats of formation are given in kcal/mole, and electron transfers are in electrons/atom. Miedema heats of formation (ΔH_M) compiled by de Boer et al. (1988) are shown for comparison as are other heat-of-formation measurements (ΔH_{EXP}) from the literature. Bandwidths for Cu, Pd, Fe, and Co were determined from density-of-states calculations by Moruzzi et al. (1978). The bandwitdths for Ti, Zr, and Pt were taken from Mattheiss (1964); Pettifor (1977); and Mattheiss and Deitz (1980) respectively. In addition, E_A and E_B are the atomic energy levels from the Hartree-Slater calculations, using $d^{N-1}s^1$ configurations.

As shown in Table 5.2, the model predicts the correct sign for the heat of formation when ΔN is small, but fails when ΔN is large. In addition, the model generally overestimates the heats of formation and the electron transfers compared to their experimental values. In the case of CuAu, the model fails completely as both constituents have full *d* bands. It should be noted, however, that ΔH is quite sensitive to the input band parameters. For example, reducing the difference between E_A and E_B by 20% for CuZr (leaving the other parameters unchanged) yields a heat of formation of about –3 kcal/mole, a value close to that observed experimentally. This sensitivity, however, combined with the inaccuracies of the input parameters, makes the model of questionable use for accurately predicting heats of formation of alloys. It does, however, provide an interesting picture of alloying between transition metals and suggests that ΔH should scale roughly with ΔQ. This scaling behavior, however, was not observed between the *d*-occupancy measurements and the experimental heats of formation. For example, although CuPd has a larger heat of formation than CuZr and CuTi, it showed no electron transfer, whereas CuZr and CuTi both showed a depletion of about 0.2 electron/atom from Cu atoms. Such discrepancies are not surprising

Alloy	N_A, N_B	E_A, E_B	W_A, W_B	ΔH	ΔQ_A	ΔH_M	ΔH_{EXP}
CuZr	10, 3	–6.5, –3.3	4.0, 7.8	+5.4	–0.9	–8.1	–2.2 [a]
CuTi	10, 3	–6.5, –3.3	4.0, 5.2	+2.5	–0.5	–3.1	–2.3 [a]
CuPd	10, 9	–6.5, –7.8	4.0, 5.5	–8 .0	–0.9	–4.8	–2.6 [b]
CuPt	10, 9	–6.5, –8.2	4.0, 7.2	–8.0	–0.9	–4.3	–1.6 [c]
CuAu	10, 10			0	0	–2.0	–1.8 [c]
FeCo	7, 8	–5.2, –5.4	6.1, 5.9	–0.5	+0.3	–0.2	–1.6 [c]

[a] Kleppa and Watanabe (1982).

[b] Steiner and Hüfner (1981).

[c] Kubaschewski and Catterall (1956).

Table 5.2. Heats of formation and electron transfers calculated from the Pettifor model. Band widths, Miedema heats of formation, and heats of formation from the literature are also shown. Energies are in eV, and heats of formation are in kcal/mole.

given the simple nature of the model and the fact that it ignores *s* electrons completely.

5.3 Summary and Conclusions

I have presented an analysis of the white lines found at the L_2 and L_3 absorption edges for the 3*d* and 4*d* transition metals. Plots of the white line intensity normalized to the trailing background were shown to reflect the linear filling of the *d* states across both transition series. In addition, the correlations between normalized white line intensity and *d* occupancy provided a method for measuring changes in *d* occupancy that were due to alloying and solid-state phase transformations.

The normalized white line intensity was modeled using atomic wave functions from Hartree-Slater calculations. Although these calculations deviated from the experimental data for the early 4*d* transition metals, the agreement for the 3*d* series permitted a correction of the white line intensity correlation for the effects of the matrix elements. Measurements of *d*-occupancy changes that were due to alloying using both the corrected and uncorrected correlations were in agreement with calculations from the literature.

In addition, measurements of *d*-occupancy changes that were due to alloying were not simply proportional to the corresponding heats of formation, although a simple *d*-band model of alloying suggests that electron transfers and heats of formation should roughly scale. The discrepancy is not surprising given the simple nature of the model and the fact that it ignores *s* electrons entirely.

References for Chapter 5

de Boer, F. R., Boom, R., Mattens, W. C. M., Miedema, A. R., and Niessen, A. K., Cohesion in Metals: Transition Metal Alloys, North-Hollond, Amsterdam (1988).

Friedel. J., in The Physics of Metals, I - Electrons, ed. J. M. Ziman, Cambridge University Press, Cambridge, pp. 340-408 (1969).

Hamdeh, H. H., Fultz, B., Pearson, D. H., Phys. Rev. B 39 (16), 11233 (1989).

Kittel, C., Introduction to Solid State Physics, 6th. Ed., John Wiley & Sons, New York, 55 (1986).

Kleppa, O. J. and Watanabe, S., Metallurgical Trans. 13B, 391 (1982).

Kokko, K., Ojala, E., Mansikka, K., J. Phys.: Cond. Mat. 2, 4587 (1990).

Kubaschewski, O. and Catterall, J. A., Thermochemical Data of Alloys, Pergamon Press, New York, pp. 41, 65 (1956).

Manh, D. N., Mayou, D., Cyrot-Lackmann, F., and Pasturel, A., J. Phys. F 17, 1309 (1987).

Mattheiss, L. F., Phys. Rev. 134 (4A), A970 (1964).

Mattheiss, L. F. and Dietz, R. E., Phys. Rev. B 22 (4), 1663 (1980).

Miedema, A. R., de Boer, F. R., and de Chatel, P. F., J. Phys. F 3, 1558 (1973).

Miedema, A. R., Boom, R., de Boer, F. R., J. Less Com. Met. 41, 283 (1975).

Moruzzi, V. L., Janak, J. F., and Williams, A. R., Calculated Electronic Properties of Metals, Pergamon Press Inc., New York (1978).

Pettifor, D. G., J. Phys. F 7 (4), 613 (1977).

Pettifor, D. G., Solid State Comm. 28, 621 (1978).

Pettifor, D. G., Phys. Rev. Lett. 42, 846 (1979).

Pettifor, D. G., in Physical Metallurgy, eds. R. W. Cahn and P. Haasen, Elsevier, Amsterdam, pp. 73-152 (1983).

Pettifor, D. G., in Solid State Physics, Vol. 40, eds. H. Ehrenreich, D. Turnbull, and F. Seitz, Academic Press, Orlando, pp. 43-92 (1987).

Richter, R. and Eschrig, H., J. Phys. F 18, 1813 (1988).

Steiner, P. and Hüfner, S., Acta. Metall. 29, 1885 (1981).

Winter, H., Durham, P. J., Temmerman, W. M., and Stocks, G. M., Phys. Rev. B 33(4), 2370 (1986).

Appendix 1 $L_{2,3}$ Edge Spectra for the 3*d* and 4*d* Transition Metals

In the following pages, deconvoluted and background subtracted $L_{2,3}$ edge spectra are presented for the 3*d* and 4*d* transition metals. These data have been processed as described in Chapter 3.

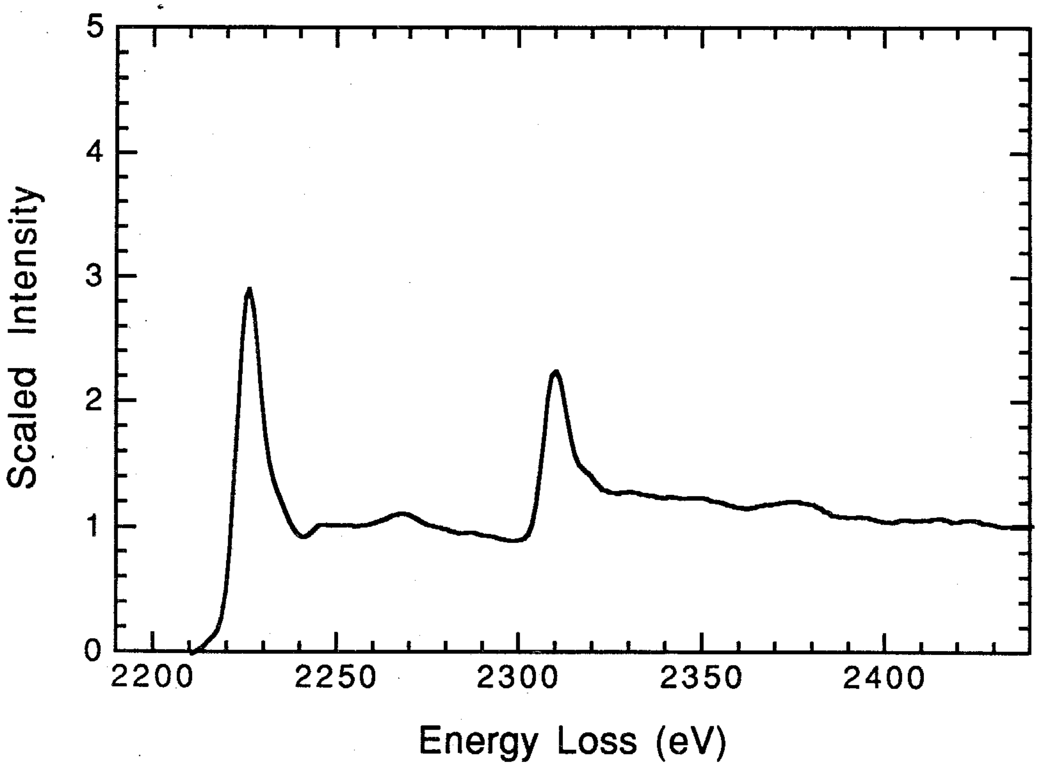

Figure A1.1. $L_{2,3}$ spectrum for zirconium.

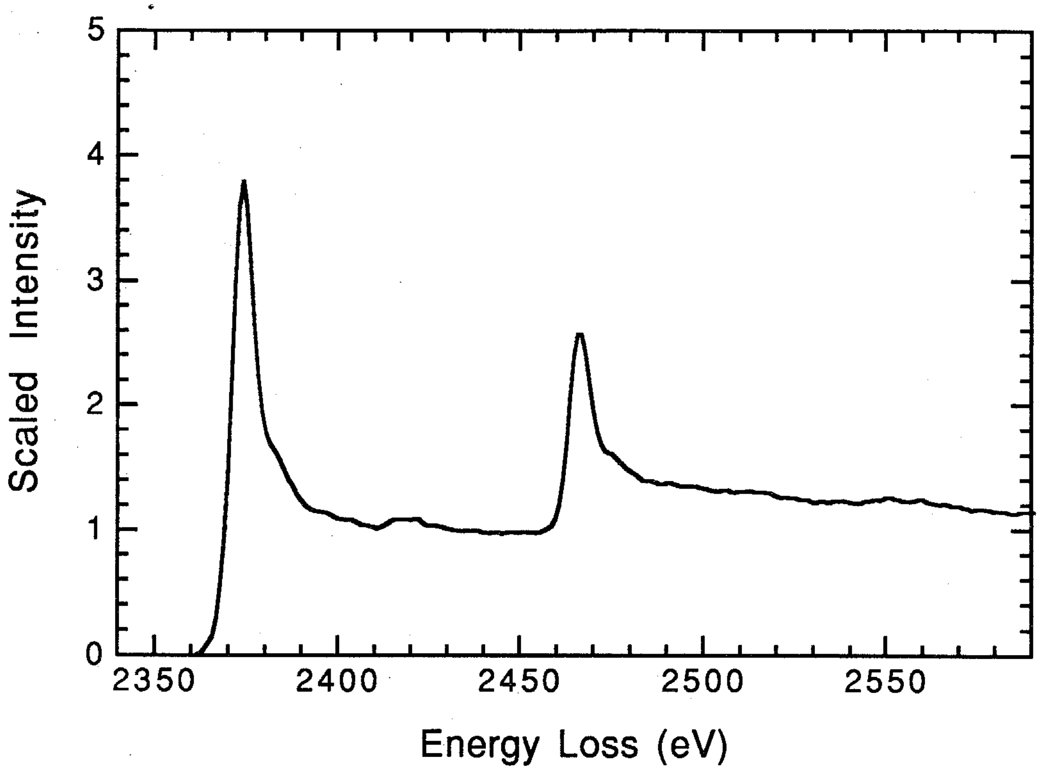

Figure A1.2. $L_{2,3}$ spectrum for niobium.

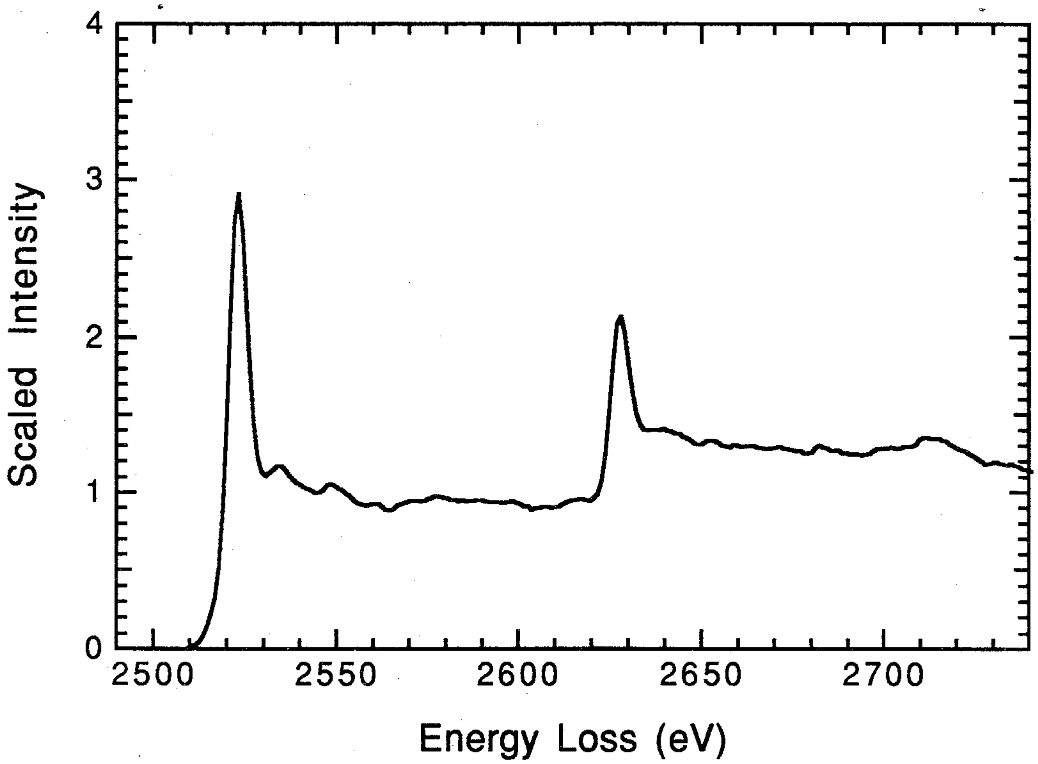

Figure A1.3. $L_{2,3}$ spectrum for molybdenum.

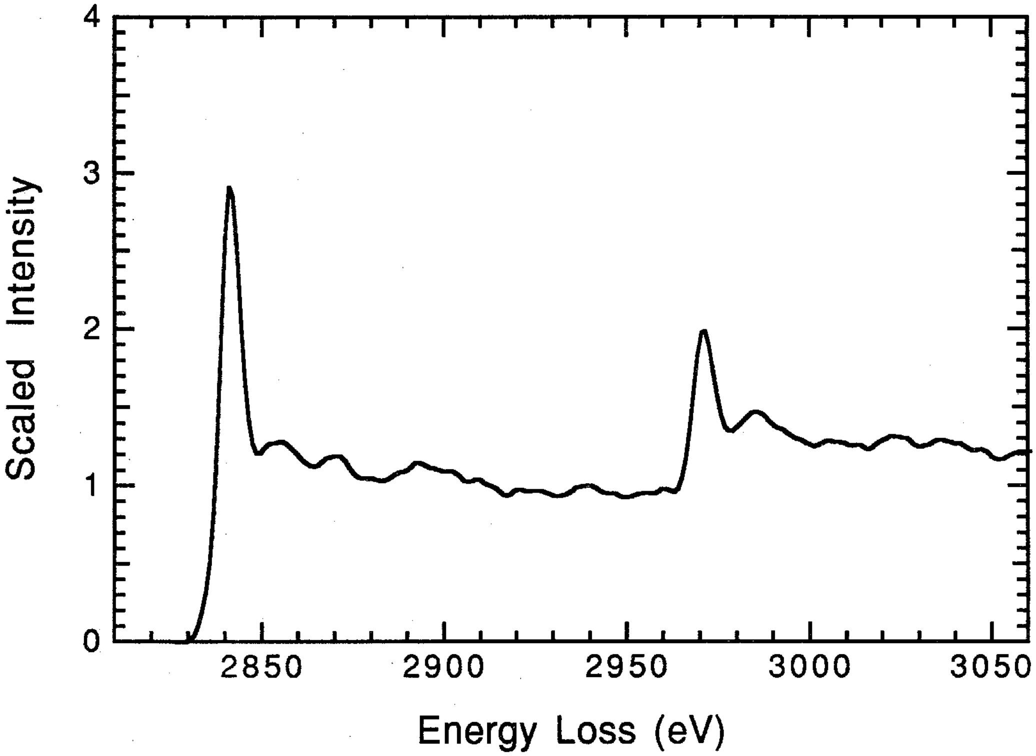

Figure A1.4. $L_{2,3}$ spectrum for ruthenium.

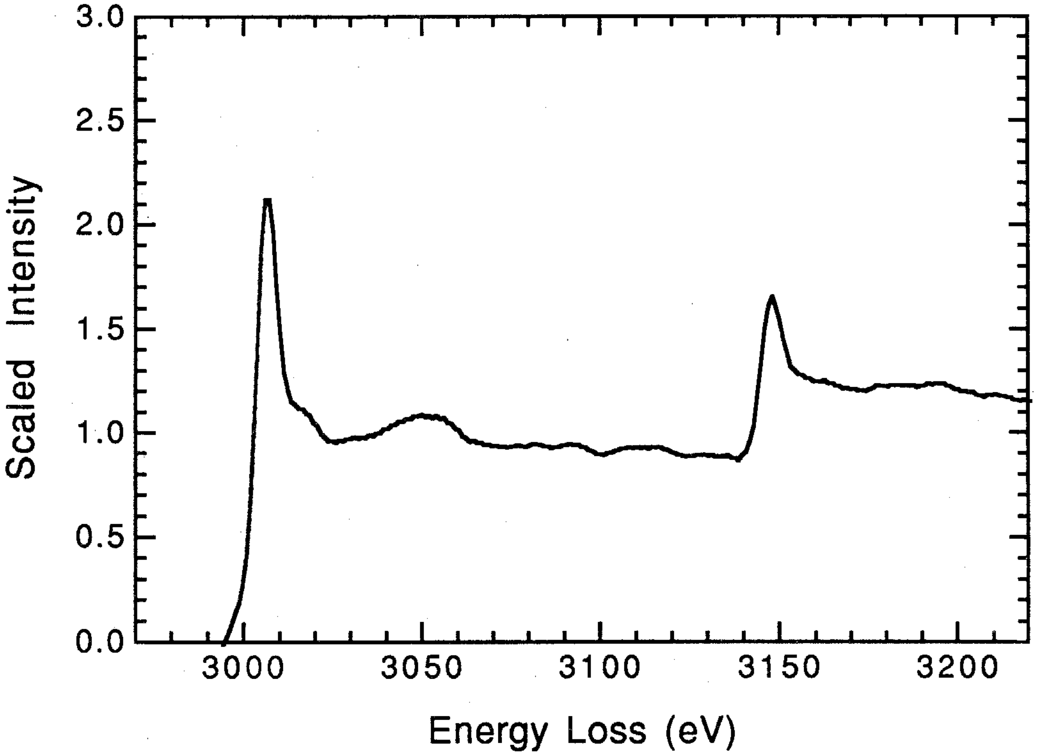

Figure A1.5. $L_{2,3}$ spectrum for rhodium.

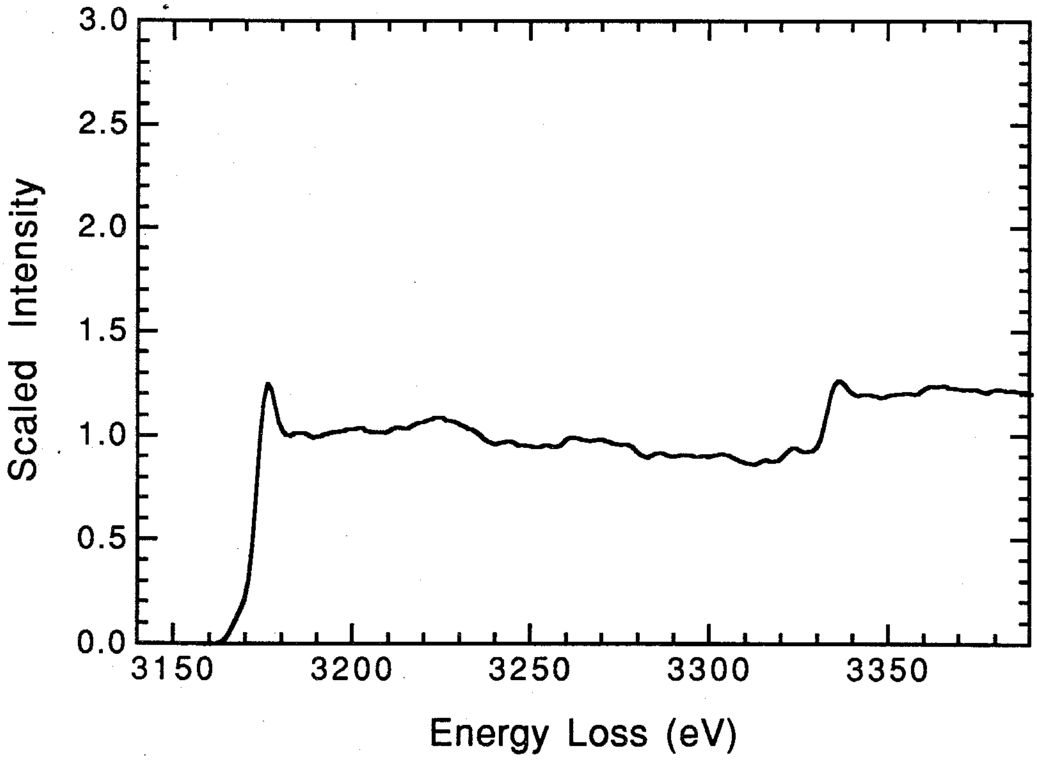

Figure A1.6. $L_{2,3}$ spectrum for palladium.

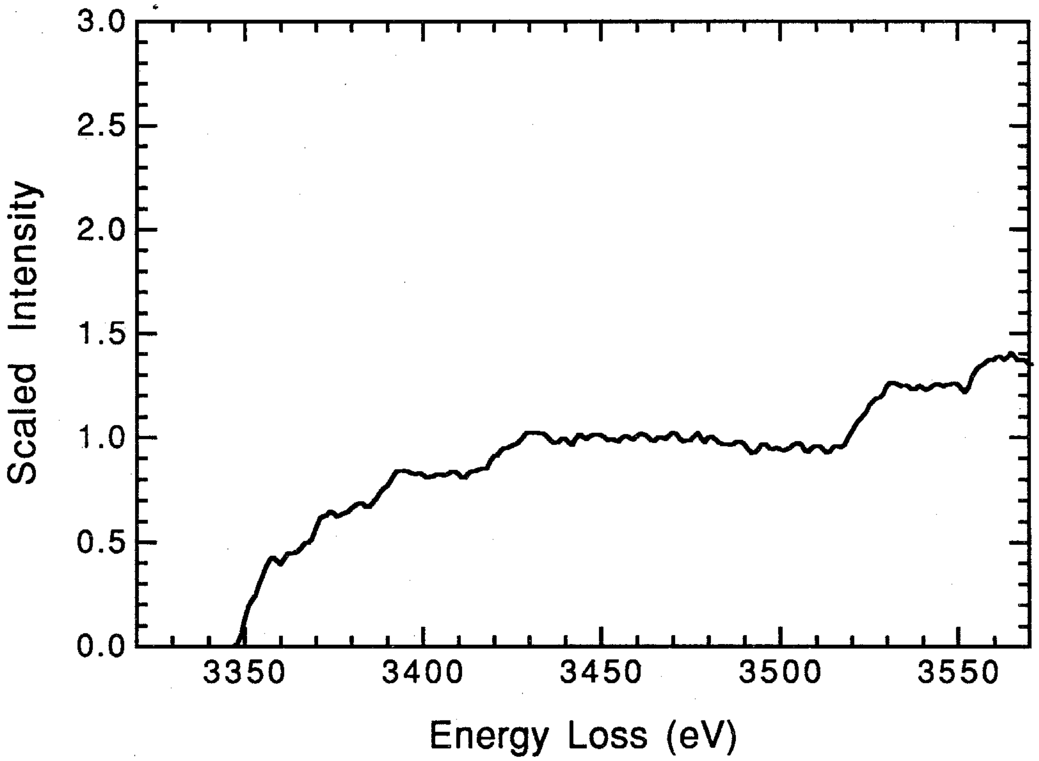

Figure A1.7. $L_{2,3}$ spectrum for silver.

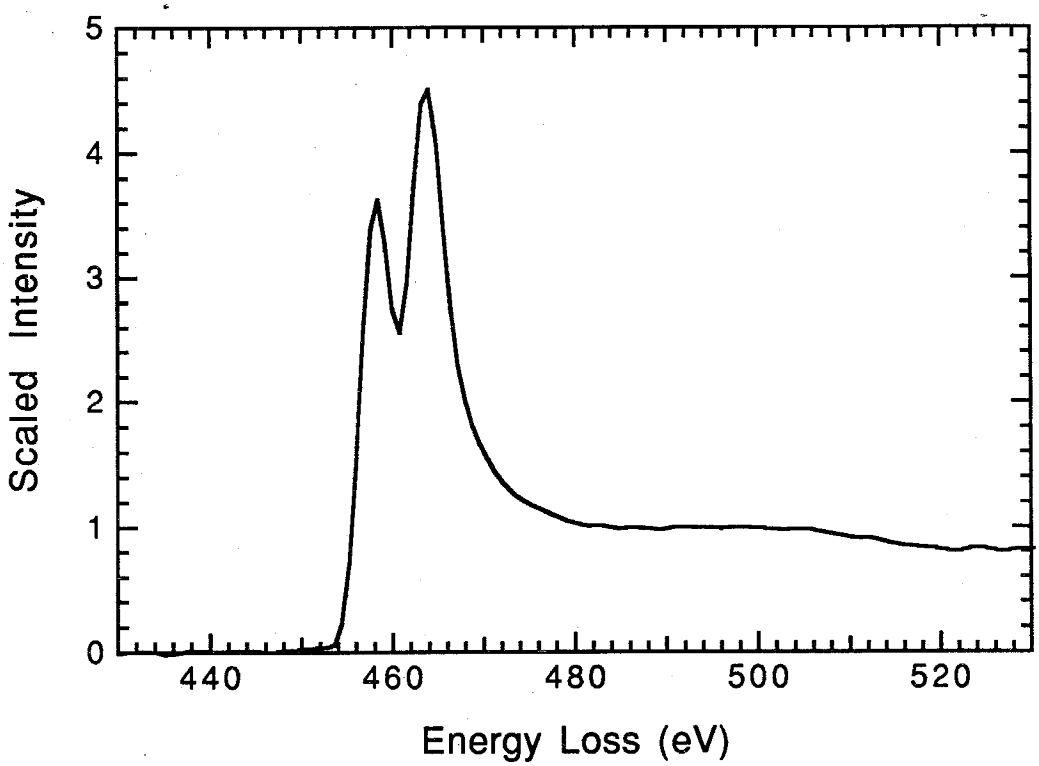

Figure A1.8. $L_{2,3}$ spectrum for titanium.

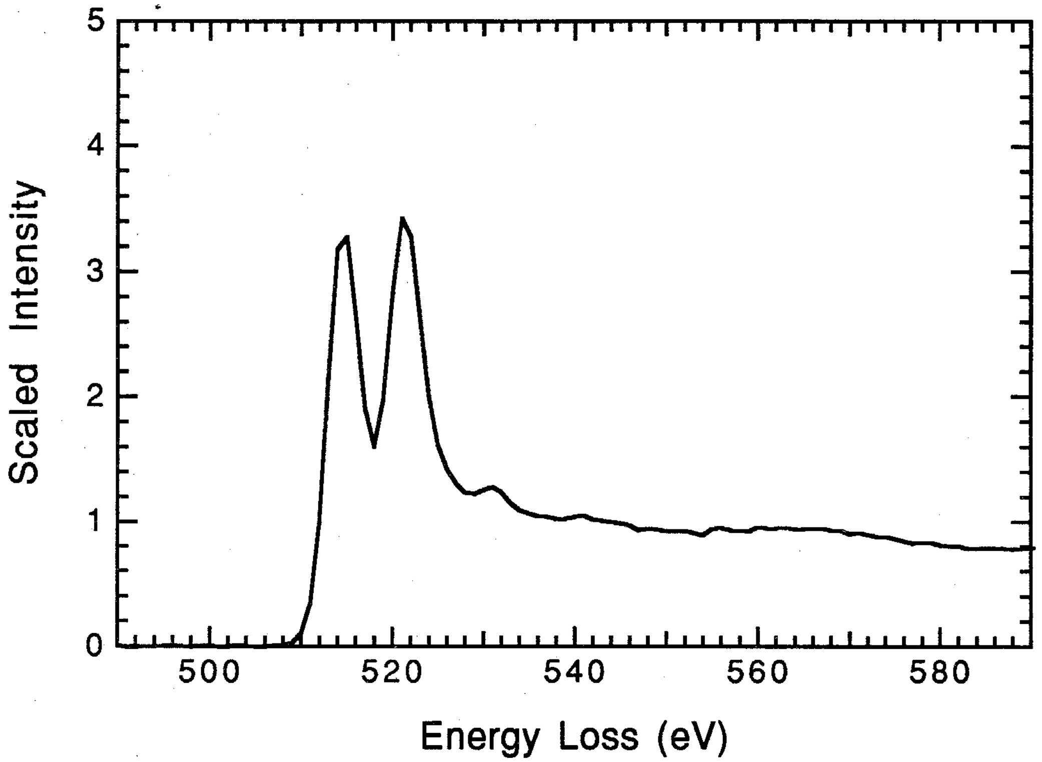

Figure A1.9. $L_{2,3}$ spectrum for vanadium.

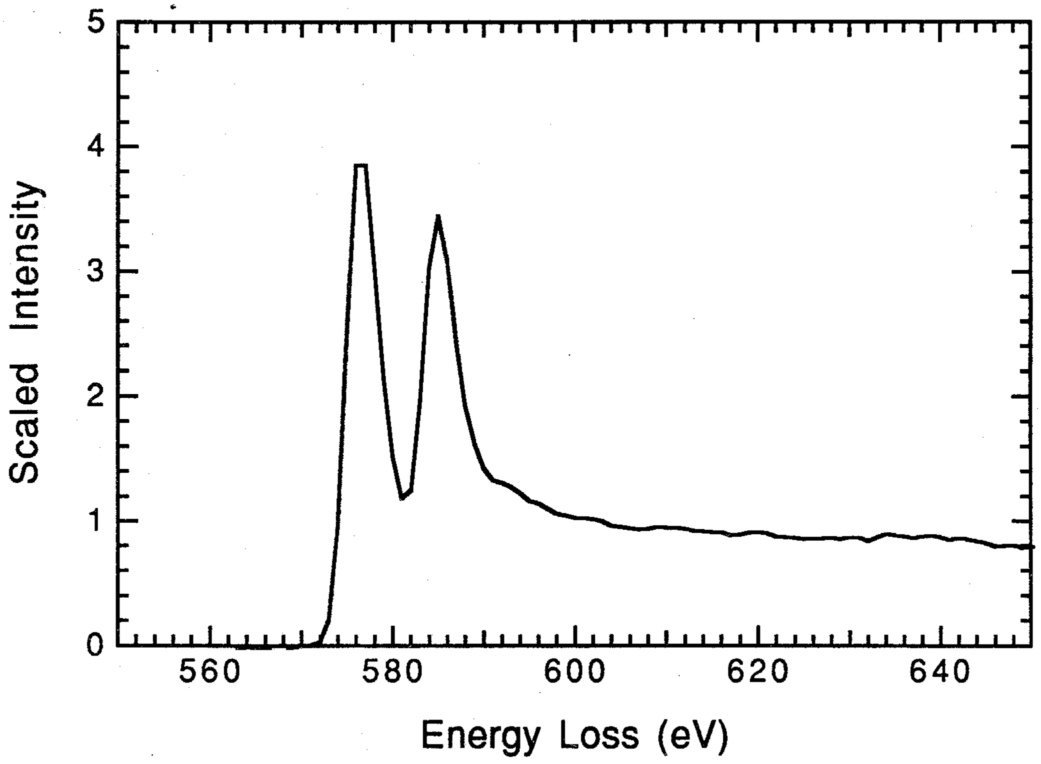

Figure A1.10. $L_{2,3}$ spectrum for chromium.

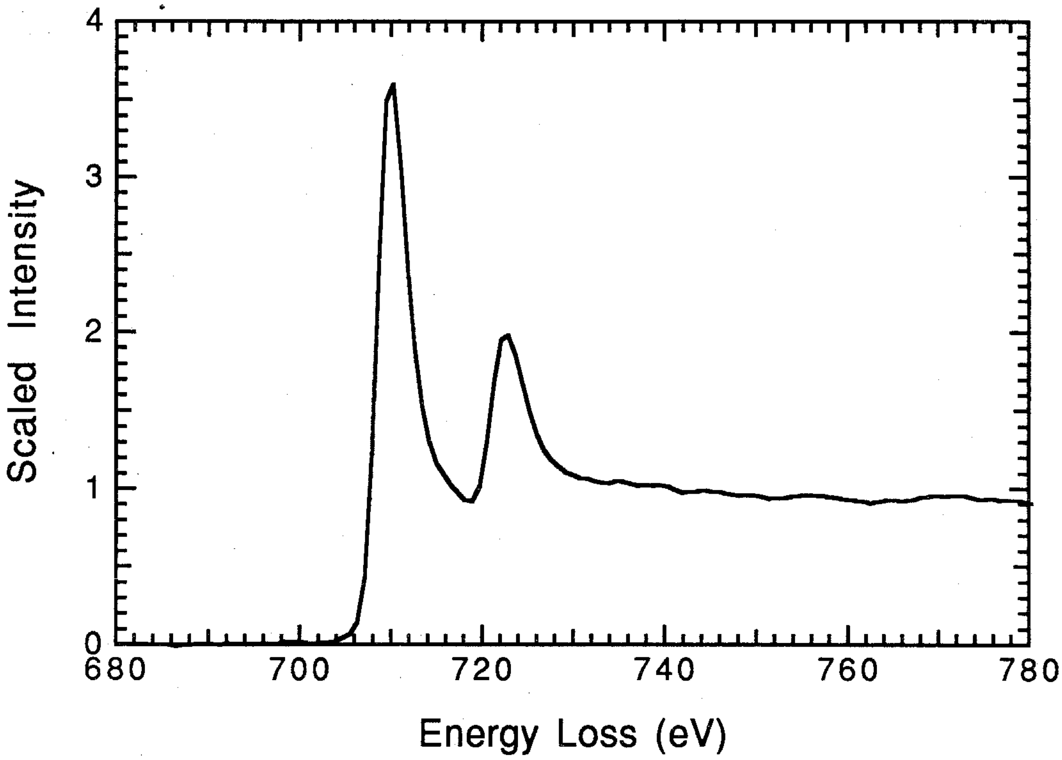

Figure A1.11. $L_{2,3}$ spectrum for iron.

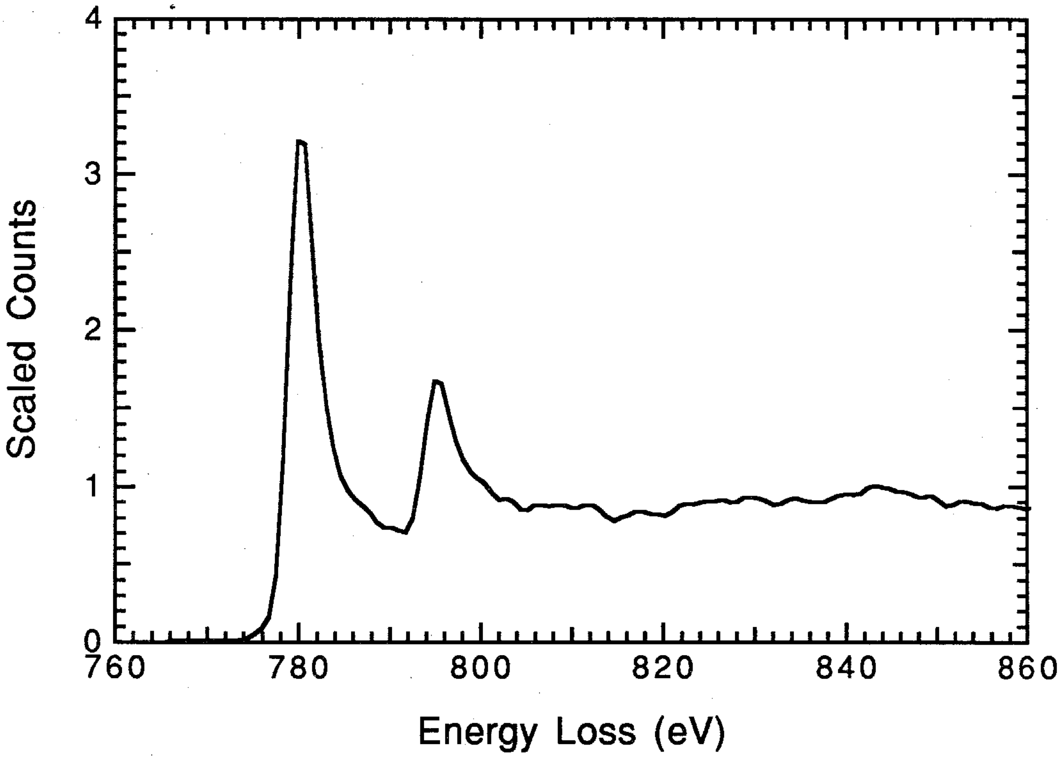

Figure A1.12. $L_{2,3}$ spectrum for cobalt.

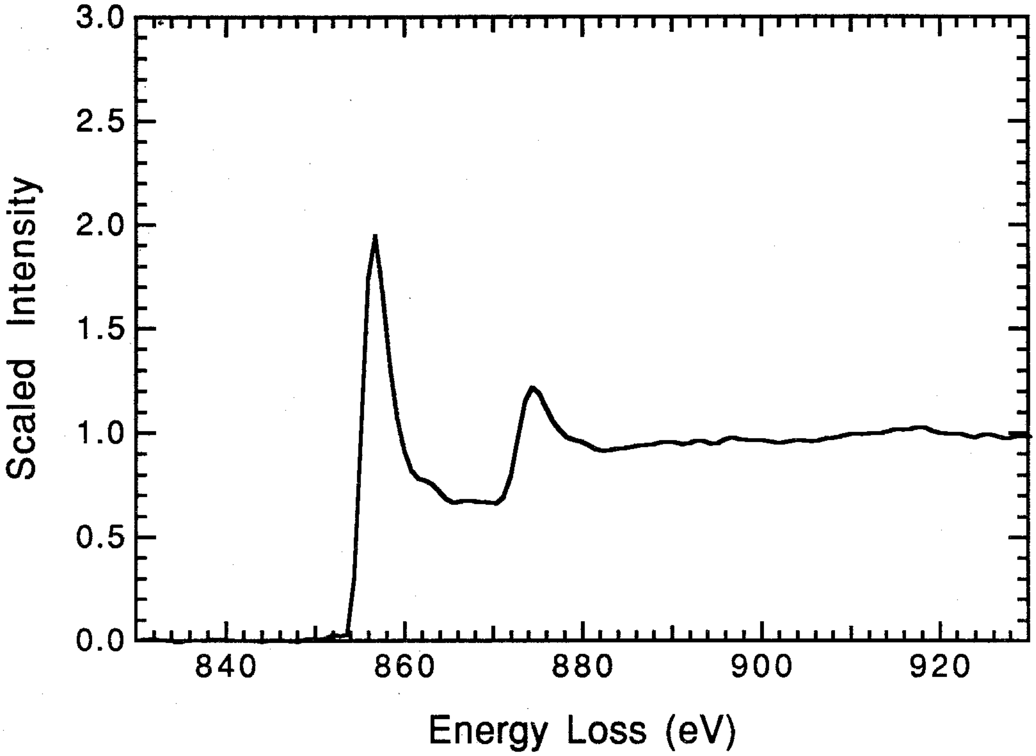

Figure A1.13. $L_{2,3}$ spectrum for nickel.

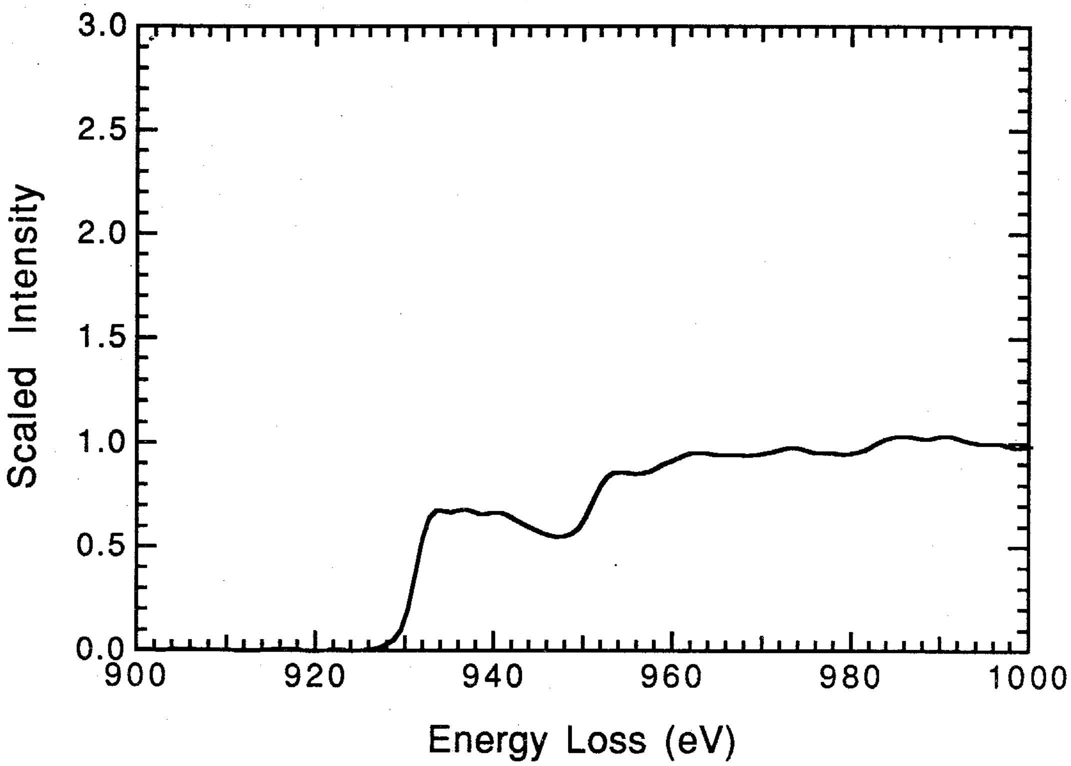

Figure A1.14. $L_{2,3}$ spectrum for copper.

Appendix 2 Hartree-Slater Calculations

The Hartree-Slater method of atomic-structure calculations is well documented (Hartree, 1957; Herman and Skillman, 1963). I will briefly describe the nature of the calculation and typical computer input/output.

The time-independent Schrödinger equation for a Z electron atom assuming a nucleus of infinite mass and ignoring all but Coulomb interactions is written as

$$\left\{\sum_{i=1}^{Z}\left\{\frac{\mathbf{p}_i^2}{2m}-\frac{Ze^2}{r_i}\right\}+\sum_{i>j}\frac{e^2}{|\mathbf{r}_i-\mathbf{r}_j|}\right\}\Psi(\mathbf{r}_1,\mathbf{r}_2,\ldots,\mathbf{r}_n)$$

$$= E\,\Psi(\mathbf{r}_1,\mathbf{r}_2,\ldots,\mathbf{r}_n). \qquad \text{(A2.1)}$$

Here, $\mathbf{p}_i$ is the momentum operator, Ψ is the wave function of the atom, and $\mathbf{r}_i$ denotes the position vectors of the electrons. In the Hartree approximation, Ψ is approximated by a product of one-electron wave functions, i.e.,

$$\Psi(\mathbf{r}_1,\mathbf{r}_2,\ldots,\mathbf{r}_n) = \phi_1(\mathbf{r}_1)\phi_2(\mathbf{r}_2)\ldots\phi_z(\mathbf{r}_z). \qquad \text{(A2.2)}$$

Minimizing the Hamiltonian through the variational principle yields Z one-electron equations which may be simplified by assuming that each electron moves in a static potential due to the other Z-1 electrons. These Z one-electron equations may be separated according to the usual angular and radial parts. The ϕ_i are then given by

$$\phi_i = R_{nl}(r)\, Y_{lm}(\theta,\phi), \qquad \text{(A2.3)}$$

where $R_{nl}(r)$ is a radial wave function and $Y_{lm}(\theta,\phi)$ is a spherical harmonic. The radial equations to be solved are

$$\left\{ -\frac{d^2}{dr^2} + \frac{l(l+1)}{r^2} + V(r) \right\} P_{nl}(r) = E_{nl}\, P_{nl}(r), \qquad \text{(A2.4)}$$

where $P_{nl}(r) = r\, R_{nl}(r)$. In this equation E and V(r) are measured in units of Rydbergs and r is measured in Bohr units. In addition, V(r) is the sum of the nuclear Coulomb potential and the average Coulomb potential of the electrons. The treatment thus far, however, ignores exchange, i.e., that the total wave function should be antisymmetric. In the Hartree-Slater method, exchange is taken into account in an approximate manner by including in V(r) a free-electron exchange potential which is proportional to the cube root of the electronic charge density. The code used in this study incorporated a Kohn-Sham exchange potential, which is simply the free-electron exchange potential multiplied by 2/3. In addition, since the Hartree-Slater treatment assumes a spherically-symmetric static potential, Coulomb-correlation effects are ignored.

At sufficiently large values of r, the nuclear potential and the total electronic Coulomb potential cancel. In addition, the exchange potential goes to zero since the charge density goes to zero, and therefore the entire potential goes to zero. The treatment is therefore flawed, since an electron at large r should see the nuclear potential screened by the other N-1 electrons, i.e., the electron should not act upon itself. The code of Herman and Skillman remedies this problem by forcing the potential to have the correct asymptotic form.

The average, electronic Coulomb potential embedded in V(r) depends on the spherically averaged, total, electronic charge density. Since both this potential and the one-electron wave functions are unknown, the problem must be solved self-consistently. This is accomplished in the code by first solving the one-electron radial equations using a trial potential and trial energy eigenvalues. The potential is then recalculated from the total charge density obtained from the previous solution, and the process is repeated until self-consistency is obtained. The numerical integration techniques are described in detail in Herman and Skillman (1963).

Input and output files for a nickel atom with a core hole are presented in Tables A2.1 and A2.2 in the pages following this discussion. The input and output files are organized as follows:

INPUT

lines 1-4: heading, control parameters, and integration grid parameters

lines 5-15: normalized starting potential

line 16: Z, number of core states, number of valence states, ionicity

lines 17-23: atomic configuration (label, angular momentum numbers, occupation number, eigenvalue estimates)

lines 24-25: termination parameters

OUTPUT

line 1: heading

line 2: Z, radial grid parameters, number of grid points

lines 3-27: output potential as -V(r)*r/2

line 28: label output wave function #1, angular momentum number, occupation, 0.5*energy eigenvalue

lines 29-53: output wave function #1 as r*R(r)

line 54: label output wave function #2, angular momentum number, occupation, 0.5*energy eigenvalue

lines 55-79: output wave function #2 as r*R(r)

Wave functions generated for atoms of the 3*d* and 4*d* transition series are presented in Figures A2.1 through A2.12. These wave functions were generated using excited-state configurations as described in Chapter 4.

As mentioned in Chapter 4, I wrote a computer code to generate continuum wave functions using the self-consistent potentials from the Herman-Skillman code. These wave functions were obtained through numerical integration of Equation A2.4 by the Numerov method (Hartree, 1957) where E is now the continuum energy. For equations such as A2.4 of the form

$$y'' = F(r)\, y, \qquad \text{(A2.5)}$$

the finite difference formula reads

$$y_{j+1} - 2y_j + y_{j-1} = (\delta^2)\{F_j y_j + \frac{1}{12}(F_{j+1}y_{j+1} - 2F_j y_j + F_{j-1}y_{j-1})\}, \qquad \text{(A2.6)}$$

where δ is the distance between consecutive y_j. Thus, an integration over a linear grid of spacing δ may be carried out if y is known at the first two grid points.

These two starting values for P(r) (or y in A2.6) may be determined using the first few terms of a series solution for A2.4 at small r. At small enough r, V(r) is simply the nuclear potential, and the function F(r) in A2.6 is given by

$$F(r) = \frac{l(l+1)}{r^2} - \frac{2\,Z}{r} - E. \qquad \text{(A2.7)}$$

The factor of 2 on the potential arises when the Schrödinger equation is written in reduced form, where P(r) = r*R(r). A series solution of the form

$$P(r) = r^b \sum_{n=0}^{\infty} a_n r^n \qquad \text{(A2.8)}$$

yields b=l+1 and the following first three coefficients:

$$a_1 = -\frac{Z\,a_0}{(l+1)} \qquad \text{(A2.9)}$$

$$a_2 = \frac{a_0}{(2l+3)}\left\{\frac{Z^2}{(l+1)} - \frac{E}{2}\right\} \qquad \text{(A2.10)}$$

$$a_3 = \frac{a_0}{6\,(l+1)\,(l+2)\,(2l+3)} \left\{Z\,E\,(3l+4) - 2\,Z^3\right\}. \qquad \text{(A2.11).}$$

The value of a_0 may be arbitrarily chosen as unity since the wave function is normalized following the integration.

The program initially calculates a wave function using a linear grid spacing of 0.002 Bohr radii. A second wave function is then calculated using a grid spacing of 0.001 Bohr radii. These wave functions are then normalized to an amplitude of $\pi^{-1/2}\,E^{-1/4}$ at forty Bohr radii (essentially infinity) and compared with each other to verify that the integrations are accurate. Maximum differences between the two wave functions calculated in this manner were typically 0.1% of the maximum amplitude. Continuum wave functions for ions of the *3d* and *4d* series are presented in Figures A2.1 through A2.12.

Input and output files for generating a continuum wave function of energy 50 eV and l=2 are shown in Tables A2.3 and A2.4, respectively. In addition to calculating the continuum wave function, the code also reads in the associated *2p* wave function and calculates its dipole integral with the continuum function. The input and output files are organized as follows:

INPUT

line 1: heading

line 2: Z, radial grid parameters, number of input radial grid points

lines 3-30: self-consistent potential

line 31: 2*p* wave function heading, angular momentum number, occupation, 0.5*energy eigenvalue

lines 32-59: 2*p* wave function

OUTPUT

line 1: linear output grid spacing in Bohr units, maximum difference between wave functions

line 2: dipole integral (twice)

lines 3+: tabular output of normalized, continuum wave function

A copy of the continuum code is presented at the end of this appendix.

```
NICKEL
0.667
 0.0010 0.0500  2  3
   0.0001  0.0001  441   0 100   1   0
1.00000 0.98990 0.97960 0.96930 0.95890 0.94850 0.93830 0.92820 0.91930 0.90850
0.89900 0.88030 0.86230 0.84500 0.82830 0.81210 0.79660 0.78160 0.76720 0.75330
0.73990 0.71450 0.69070 0.66830 0.64710 0.62690 0.60770 0.58930 0.57180 0.55510
0.53910 0.50900 0.48120 0.45530 0.43120 0.40890 0.38810 0.36880 0.35090 0.33410
0.31840 0.28950 0.26360 0.24040 0.21960 0.20100 0.18440 0.16970 0.15660 0.14500
0.13460 0.11720 0.10320 0.09180 0.08250 0.07470 0.06820 0.06260 0.05800 0.05400
0.05050 0.04490 0.04050 0.03700 0.03440 0.03000 0.02500 0.02500 0.02500 0.02500
0.02500 0.02500 0.02500 0.02500 0.02500 0.02500 0.02500 0.02500 0.02500 0.02500
0.02500 0.02500 0.02500 0.02500 0.02500 0.02500 0.02500 0.02500 0.02500 0.02500
0.02500 0.02500 0.02500 0.02500 0.02500 0.02500 0.02500 0.02500 0.02500 0.02500
0.02500 0.02500 0.02500 0.02500 0.02500 0.02500 0.02500 0.02500 0.02500 0.02500
 28.  7  0 0.00
  1S 100  2. -600.70
  2S 200  2. -110.15
  2P 210  5.  -90.02
  3S 300  2.  -30.63
  3P 310  6.  -15.71
  3D 320 10.    -.50
  4S 400  1.    -.10
-1.
2.
```

Table A2.1. Computer input file for the Herman-Skillman program.

```
Nickel
   28.00   0.001000   0.050000      192
0.2789914E+02 0.2789395E+02 0.2788848E+02 0.2788274E+02 0.2787669E+02 0.2787034E+02 0.2786365E+02 0.2785662E+02
0.2784923E+02 0.2784145E+02 0.2783327E+02 0.2782467E+02 0.2781563E+02 0.2780611E+02 0.2779611E+02 0.2778558E+02
0.2777451E+02 0.2776286E+02 0.2775061E+02 0.2773772E+02 0.2772416E+02 0.2770990E+02 0.2769490E+02 0.2767912E+02
0.2766253E+02 0.2764507E+02 0.2762671E+02 0.2760740E+02 0.2758709E+02 0.2756572E+02 0.2754325E+02 0.2751962E+02
0.2749477E+02 0.2746864E+02 0.2744116E+02 0.2741227E+02 0.2738189E+02 0.2734996E+02 0.2731639E+02 0.2728112E+02
0.2724405E+02 0.2720510E+02 0.2716419E+02 0.2712121E+02 0.2707609E+02 0.2702870E+02 0.2697896E+02 0.2692677E+02
0.2687201E+02 0.2681459E+02 0.2675437E+02 0.2669125E+02 0.2662512E+02 0.2655586E+02 0.2648335E+02 0.2640745E+02
0.2632807E+02 0.2624506E+02 0.2615832E+02 0.2606771E+02 0.2597311E+02 0.2587441E+02 0.2577148E+02 0.2566418E+02
0.2555240E+02 0.2543602E+02 0.2531493E+02 0.2518899E+02 0.2505809E+02 0.2492212E+02 0.2478093E+02 0.2463441E+02
0.2448244E+02 0.2432487E+02 0.2416158E+02 0.2399244E+02 0.2381731E+02 0.2363606E+02 0.2344856E+02 0.2325467E+02
0.2305429E+02 0.2284730E+02 0.2263361E+02 0.2241314E+02 0.2218587E+02 0.2195176E+02 0.2171083E+02 0.2146308E+02
0.2120857E+02 0.2094731E+02 0.2067932E+02 0.2040459E+02 0.2012308E+02 0.1983471E+02 0.1953939E+02 0.1923704E+02
0.1892759E+02 0.1861100E+02 0.1828729E+02 0.1795655E+02 0.1761891E+02 0.1727458E+02 0.1692379E+02 0.1656682E+02
0.1620395E+02 0.1583544E+02 0.1546154E+02 0.1508249E+02 0.1469843E+02 0.1430947E+02 0.1391570E+02 0.1351726E+02
0.1311433E+02 0.1270723E+02 0.1229640E+02 0.1188246E+02 0.1146616E+02 0.1104825E+02 0.1062944E+02 0.1021025E+02
0.9790981E+01 0.9371815E+01 0.8952934E+01 0.8534689E+01 0.8117722E+01 0.7703032E+01 0.7291972E+01 0.6886183E+01
0.6487513E+01 0.6097897E+01 0.5719260E+01 0.5353407E+01 0.5001939E+01 0.4666187E+01 0.4347167E+01 0.4045559E+01
0.3761708E+01 0.3495808E+01 0.3247477E+01 0.3016225E+01 0.2801399E+01 0.2602211E+01 0.2417794E+01 0.2247248E+01
0.2089663E+01 0.1944162E+01 0.1809890E+01 0.1686046E+01 0.1571886E+01 0.1466688E+01 0.1369796E+01 0.1280625E+01
0.1198558E+01 0.1123074E+01 0.1053686E+01 0.9899960E+00 0.9316005E+00 0.8779552E+00 0.8285437E+00 0.7829071E+00
0.7406237E+00 0.7012888E+00 0.6645465E+00 0.6300653E+00 0.5975127E+00 0.5666138E+00 0.5371078E+00 0.5087411E+00
0.4812762E+00 0.4545363E+00 0.4283673E+00 0.4026217E+00 0.3771830E+00 0.3520167E+00 0.3270885E+00 0.3024260E+00
0.2780425E+00 0.2540258E+00 0.2304772E+00 0.2011554E+00 0.1809151E+00 0.1607460E+00 0.1414533E+00 0.1231850E+00
0.1061839E+00 0.9044025E-01 0.7607326E-01 0.6321725E-01 0.5174765E-01 0.4176010E-01 0.3308054E-01 0.2573173E-01
 2P    1    5.00   -32.27
0.6393490E-03 0.7072150E-03 0.7825640E-03 0.8660878E-03 0.9585281E-03 0.1060678E-02 0.1173380E-02 0.1297531E-02
0.1434080E-02 0.1584178E-02 0.1749255E-02 0.1930908E-02 0.2130912E-02 0.2351244E-02 0.2594104E-02 0.2861942E-02
0.3157488E-02 0.3483669E-02 0.3843546E-02 0.4240454E-02 0.4678038E-02 0.5160285E-02 0.5691549E-02 0.6276691E-02
0.6921121E-02 0.7630785E-02 0.8412209E-02 0.9272534E-02 0.1021952E-01 0.1126167E-01 0.1240824E-01 0.1366939E-01
0.1505627E-01 0.1658101E-01 0.1825687E-01 0.2009831E-01 0.2212108E-01 0.2434235E-01 0.2678077E-01 0.2945667E-01
0.3239210E-01 0.3561098E-01 0.3913927E-01 0.4300507E-01 0.4723877E-01 0.5187320E-01 0.5694378E-01 0.6248867E-01
0.6854892E-01 0.7516862E-01 0.8239502E-01 0.9027871E-01 0.9887368E-01 0.1082375E+00 0.1184312E+00 0.1295198E+00
0.1415719E+00 0.1546597E+00 0.1688592E+00 0.1842501E+00 0.2009152E+00 0.2189406E+00 0.2384153E+00 0.2594308E+00
0.2820803E+00 0.3064584E+00 0.3326602E+00 0.3607804E+00 0.3909118E+00 0.4231448E+00 0.4575657E+00 0.4942543E+00
0.5332830E+00 0.5747141E+00 0.6185982E+00 0.6649707E+00 0.7138495E+00 0.7652326E+00 0.8190938E+00 0.8753806E+00
0.9340099E+00 0.9948655E+00 0.1057794E+01 0.1122601E+01 0.1189049E+01 0.1256855E+01 0.1325686E+01 0.1395157E+01
0.1464834E+01 0.1534227E+01 0.1602798E+01 0.1669955E+01 0.1735060E+01 0.1797434E+01 0.1856362E+01 0.1911098E+01
0.1960883E+01 0.2004947E+01 0.2042533E+01 0.2072904E+01 0.2095363E+01 0.2109272E+01 0.2114068E+01 0.2109283E+01
0.2094563E+01 0.2069685E+01 0.2034569E+01 0.1989295E+01 0.1934113E+01 0.1869444E+01 0.1795886E+01 0.1714210E+01
0.1625347E+01 0.1530376E+01 0.1430509E+01 0.1327049E+01 0.1221354E+01 0.1114822E+01 0.1008843E+01 0.9047590E+00
0.8038301E+00 0.7071961E+00 0.6158490E+00 0.5306087E+00 0.4521050E+00 0.3807681E+00 0.3168267E+00 0.2603151E+00
0.2110868E+00 0.1688363E+00 0.1331263E+00 0.1034176E+00 0.7910168E-01 0.5953230E-01 0.4405513E-01 0.3203333E-01
0.2286850E-01 0.1601614E-01 0.1099493E-01 0.7391789E-02 0.4861986E-02 0.3125714E-02 0.1961975E-02 0.1201031E-02
0.7161652E-03 0.4154543E-03 0.2341538E-03 0.1280321E-03 0.6780474E-04 0.3470268E-04 0.1700334E-04-0.1423524E-05
–0.9911290E-07-0.5069822E-08-0.3134225E-10 0.1013431E-10 0.7118306E-13-0.1045987E-13 0.2637792E-15-0.5160609E-17
0.8985497E-19-0.7367197E-21-0.8859952E-23 0.4678755E-25 0.6473762E-27-0.4981788E-28-0.3544814E-29-0.1805091E-30
–0.6893620E-33 0.3551768E-33 0.3989437E-36-0.3068023E-36 0.8526707E-38 0.0000000E+00 0.0000000E+00 0.0000000E+00
0.0000000E+00 0.0000000E+00 0.0000000E+00 0.0000000E+00 0.0000000E+00 0.0000000E+00 0.0000000E+00 0.0000000E+00
0.0000000E+00 0.0000000E+00 0.0000000E+00 0.0000000E+00 0.0000000E+00 0.0000000E+00 0.0000000E+00 0.0000000E+00
```

Table A2.2. Computer output file from the Herman-Skillman program.

```
Nickel
   28.00  0.001000  0.050000    216
  50.0000  2   0.0050
0.2789914E+02 0.2789395E+02 0.2788848E+02 0.2788274E+02 0.2787669E+02 0.2787034E+02 0.2786365E+02 0.2785662E+02
0.2784923E+02 0.2784145E+02 0.2783327E+02 0.2782467E+02 0.2781563E+02 0.2780611E+02 0.2779611E+02 0.2778558E+02
0.2777451E+02 0.2776286E+02 0.2775061E+02 0.2773772E+02 0.2772416E+02 0.2770990E+02 0.2769490E+02 0.2767912E+02
0.2766253E+02 0.2764507E+02 0.2762671E+02 0.2760740E+02 0.2758709E+02 0.2756572E+02 0.2754325E+02 0.2751962E+02
0.2749477E+02 0.2746864E+02 0.2744116E+02 0.2741227E+02 0.2738189E+02 0.2734996E+02 0.2731639E+02 0.2728112E+02
0.2724405E+02 0.2720510E+02 0.2716419E+02 0.2712121E+02 0.2707609E+02 0.2702870E+02 0.2697896E+02 0.2692677E+02
0.2687201E+02 0.2681459E+02 0.2675437E+02 0.2669125E+02 0.2662512E+02 0.2655586E+02 0.2648335E+02 0.2640745E+02
0.2632807E+02 0.2624506E+02 0.2615832E+02 0.2606771E+02 0.2597311E+02 0.2587441E+02 0.2577148E+02 0.2566418E+02
0.2555240E+02 0.2543602E+02 0.2531493E+02 0.2518899E+02 0.2505809E+02 0.2492212E+02 0.2478093E+02 0.2463441E+02
0.2448244E+02 0.2432487E+02 0.2416158E+02 0.2399244E+02 0.2381731E+02 0.2363606E+02 0.2344856E+02 0.2325467E+02
0.2305429E+02 0.2284730E+02 0.2263361E+02 0.2241314E+02 0.2218587E+02 0.2195176E+02 0.2171083E+02 0.2146308E+02
0.2120857E+02 0.2094731E+02 0.2067932E+02 0.2040459E+02 0.2012308E+02 0.1983471E+02 0.1953939E+02 0.1923704E+02
0.1892759E+02 0.1861100E+02 0.1828729E+02 0.1795655E+02 0.1761891E+02 0.1727458E+02 0.1692379E+02 0.1656682E+02
0.1620395E+02 0.1583544E+02 0.1546154E+02 0.1508249E+02 0.1469843E+02 0.1430947E+02 0.1391570E+02 0.1351726E+02
0.1311433E+02 0.1270723E+02 0.1229640E+02 0.1188246E+02 0.1146616E+02 0.1104825E+02 0.1062944E+02 0.1021025E+02
0.9790981E+01 0.9371815E+01 0.8952934E+01 0.8534689E+01 0.8117722E+01 0.7703032E+01 0.7291972E+01 0.6886183E+01
0.6487513E+01 0.6097897E+01 0.5719260E+01 0.5353407E+01 0.5001939E+01 0.4666187E+01 0.4347167E+01 0.4045559E+01
0.3761708E+01 0.3495808E+01 0.3247477E+01 0.3016225E+01 0.2801399E+01 0.2602211E+01 0.2417794E+01 0.2247248E+01
0.2089663E+01 0.1944162E+01 0.1809890E+01 0.1686046E+01 0.1571886E+01 0.1466688E+01 0.1369796E+01 0.1280625E+01
0.1198558E+01 0.1123074E+01 0.1053686E+01 0.9899960E+00 0.9316005E+00 0.8779552E+00 0.8285437E+00 0.7829071E+00
0.7406237E+00 0.7012888E+00 0.6645465E+00 0.6300653E+00 0.5975127E+00 0.5666138E+00 0.5371078E+00 0.5087411E+00
0.4812762E+00 0.4545363E+00 0.4283673E+00 0.4026217E+00 0.3771830E+00 0.3520167E+00 0.3270885E+00 0.3024260E+00
0.2780425E+00 0.2540258E+00 0.2304772E+00 0.2011554E+00 0.1809151E+00 0.1607460E+00 0.1414533E+00 0.1231850E+00
0.1061839E+00 0.9044025E-01 0.7607326E-01 0.6321725E-01 0.5174765E-01 0.4176010E-01 0.3308054E-01 0.2573173E-01
 2P   1   5.00  -32.27
0.6393490E-03 0.7072150E-03 0.7825640E-03 0.8660878E-03 0.9585281E-03 0.1060678E-02 0.1173380E-02 0.1297531E-02
0.1434080E-02 0.1584178E-02 0.1749255E-02 0.1930908E-02 0.2130912E-02 0.2351244E-02 0.2594104E-02 0.2861942E-02
0.3157488E-02 0.3483669E-02 0.3843546E-02 0.4240454E-02 0.4678038E-02 0.5160285E-02 0.5691549E-02 0.6276691E-02
0.6921121E-02 0.7630785E-02 0.8412209E-02 0.9272534E-02 0.1021952E-01 0.1126167E-01 0.1240824E-01 0.1366939E-01
0.1505627E-01 0.1658101E-01 0.1825687E-01 0.2009831E-01 0.2212108E-01 0.2434235E-01 0.2678077E-01 0.2945667E-01
0.3239210E-01 0.3561098E-01 0.3913927E-01 0.4300507E-01 0.4723877E-01 0.5187320E-01 0.5694378E-01 0.6248867E-01
0.6854892E-01 0.7516862E-01 0.8239502E-01 0.9027871E-01 0.9887368E-01 0.1082375E+00 0.1184312E+00 0.1295198E+00
0.1415719E+00 0.1546597E+00 0.1688592E+00 0.1842501E+00 0.2009152E+00 0.2189406E+00 0.2384153E+00 0.2594308E+00
0.2820803E+00 0.3064584E+00 0.3326602E+00 0.3607804E+00 0.3909118E+00 0.4231448E+00 0.4575657E+00 0.4942543E+00
0.5332830E+00 0.5747141E+00 0.6185982E+00 0.6649707E+00 0.7138495E+00 0.7652326E+00 0.8190938E+00 0.8753806E+00
0.9340099E+00 0.9948655E+00 0.1057794E+01 0.1122601E+01 0.1189049E+01 0.1256855E+01 0.1325686E+01 0.1395157E+01
0.1464834E+01 0.1534227E+01 0.1602798E+01 0.1669955E+01 0.1735060E+01 0.1797434E+01 0.1856362E+01 0.1911098E+01
0.1960883E+01 0.2004947E+01 0.2042533E+01 0.2072904E+01 0.2095363E+01 0.2109272E+01 0.2114068E+01 0.2109283E+01
0.2094563E+01 0.2069685E+01 0.2034569E+01 0.1989295E+01 0.1934113E+01 0.1869444E+01 0.1795886E+01 0.1714210E+01
0.1625347E+01 0.1530376E+01 0.1430509E+01 0.1327049E+01 0.1221354E+01 0.1114822E+01 0.1008843E+01 0.9047590E+00
0.8038301E+00 0.7071961E+00 0.6158490E+00 0.5306087E+00 0.4521050E+00 0.3807681E+00 0.3168267E+00 0.2603151E+00
0.2110868E+00 0.1688363E+00 0.1331263E+00 0.1034176E+00 0.7910168E-01 0.5953230E-01 0.4405513E-01 0.3203333E-01
0.2286850E-01 0.1601614E-01 0.1099493E-01 0.7391789E-02 0.4861986E-02 0.3125714E-02 0.1961975E-02 0.1201031E-02
0.7161652E-03 0.4154543E-03 0.2341538E-03 0.1280321E-03 0.6780474E-04 0.3470268E-04 0.1700334E-04-0.1423524E-05
-0.9911290E-07-0.5069822E-08-0.3134225E-10 0.1013431E-10 0.7118306E-13-0.1045987E-13 0.2637792E-15-0.5160609E-17
0.8985497E-19-0.7367197E-21-0.8859952E-23 0.4678755E-25 0.6473762E-27-0.4981788E-28-0.3544814E-29-0.1805091E-30
-0.6893620E-33 0.3551768E-33 0.3989437E-36-0.3068023E-36 0.8526707E-38 0.0000000E+00 0.0000000E+00 0.0000000E+00
0.0000000E+00 0.0000000E+00 0.0000000E+00 0.0000000E+00 0.0000000E+00 0.0000000E+00 0.0000000E+00 0.0000000E+00
0.0000000E+00 0.0000000E+00 0.0000000E+00 0.0000000E+00 0.0000000E+00 0.0000000E+00 0.0000000E+00 0.0000000E+00
```

A2.3. Computer input file for the continuum wave function program.

```
0.3200000E-01   -0.3742832E-03
0.3655345E-01    0.3555345E-01
NICKEL
100.0000 .2
0.0000000E+00  0.0000000E+00
0.3200000E-01  0.2207376E-02
0.6400000E-01  0.1337088E-01
0.9600001E-01  0.3463111E-01
0.1280000E+00  0.6359622E-01
0.1600000E+00  0.9695385E-01
0.1920000E+00  0.1315692E+00
0.2240000E+00  0.1648803E+00
0.2560000E+00  0.1949776E+00
0.2880000E+00  0.2205576E+00
0.3200000E+00  0.2408285E+00
0.3520000E+00  0.2554014E+00
0.3840000E+00  0.2641894E+00
0.4160000E+00  0.2673234E+00
0.4480000E+00  0.2650870E+00
0.4800000E+00  0.2578670E+00
0.5120000E+00  0.2461148E+00
0.5440000E+00  0.2303164E+00
0.5760000E+00  0.2109698E+00
0.6080000E+00  0.1885696E+00
0.6400000E+00  0.1635963E+00
0.6720001E+00  0.1365104E+00
0.7040001E+00  0.1077492E+00
0.7360001E+00  0.7772587E-01
0.7680001E+00  0.4682956E-01
0.8000000E+00  0.1542647E-01
0.8320000E+00 -0.1613901E-01
0.8640000E+00 -0.4754314E-01
0.8960000E+00 -0.7848173E-01
0.9280000E+00 -0.1086694E+00
0.9600000E+00 -0.1378388E+00
0.9920000E+00 -0.1657408E+00
0.1024000E+01 -0.1921440E+00
0.1056000E+01 -0.2168348E+00
0.1088000E+01 -0.2396183E+00
0.1120000E+01 -0.2603181E+00
0.1152000E+01 -0.2787768E+00
0.1184000E+01 -0.2948571E+00
0.1216000E+01 -0.3084415E+00
0.1248000E+01 -0.3194331E+00
```

Table A2.4. Computer output file from the continuum wave function program. Only the first page of output is shown.

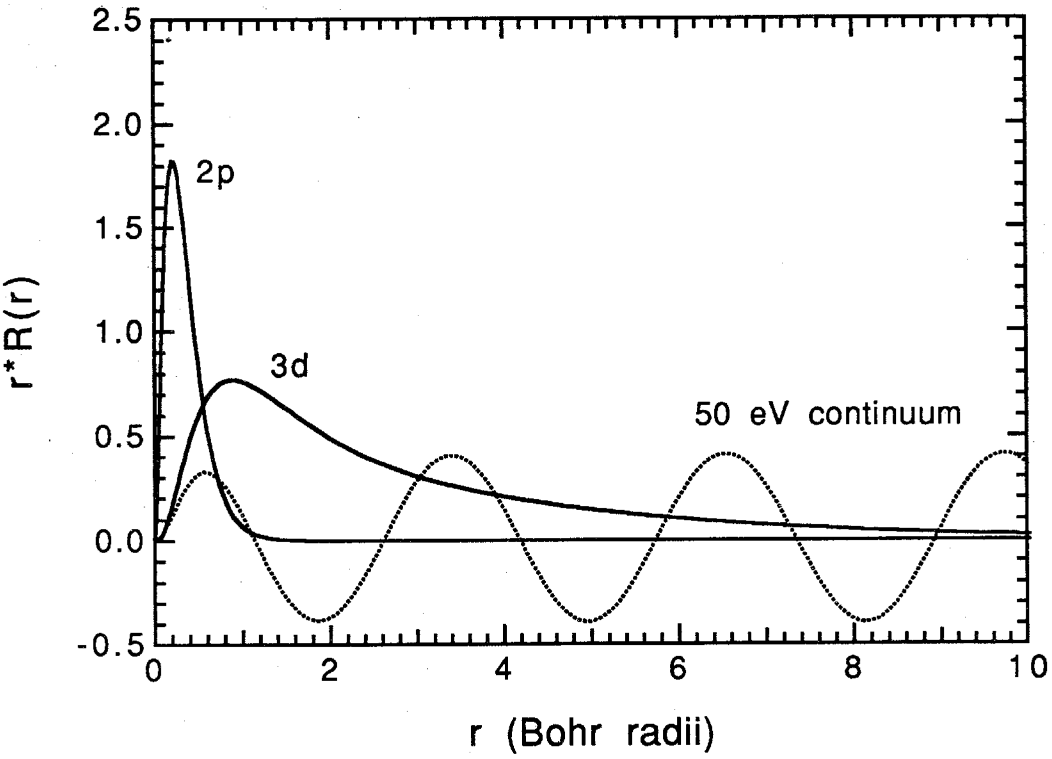

Figure A2.1. Atomic wave functions for titanium.

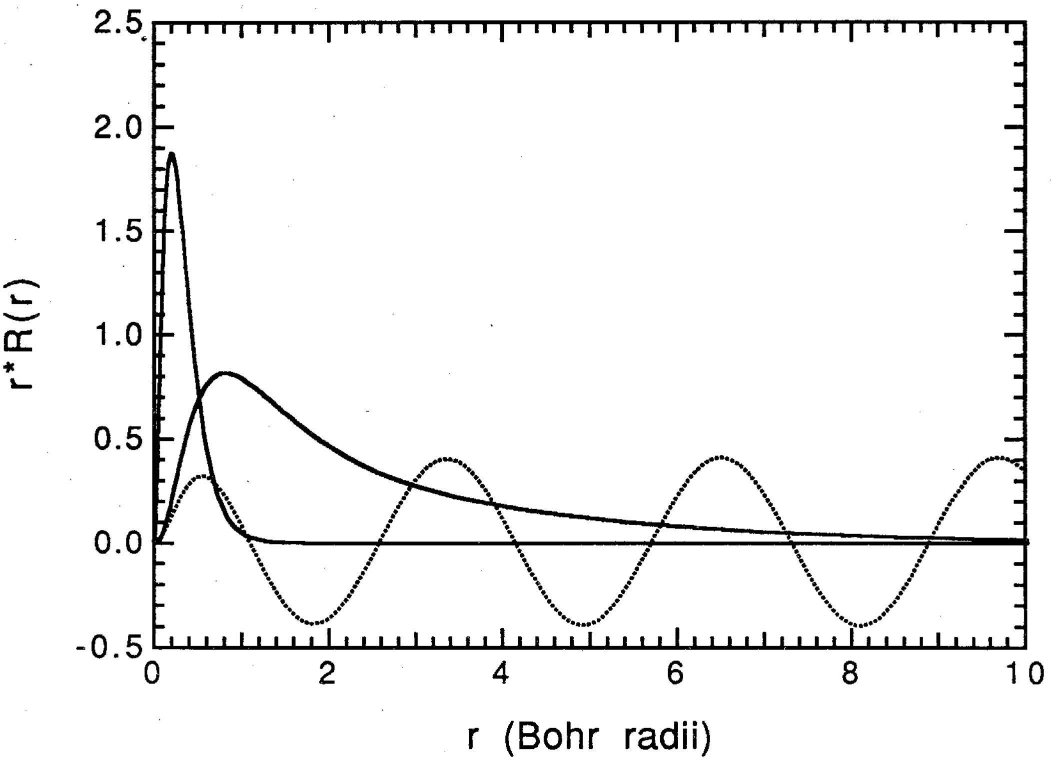

Figure A2.2. Atomic wave functions for vanadium.

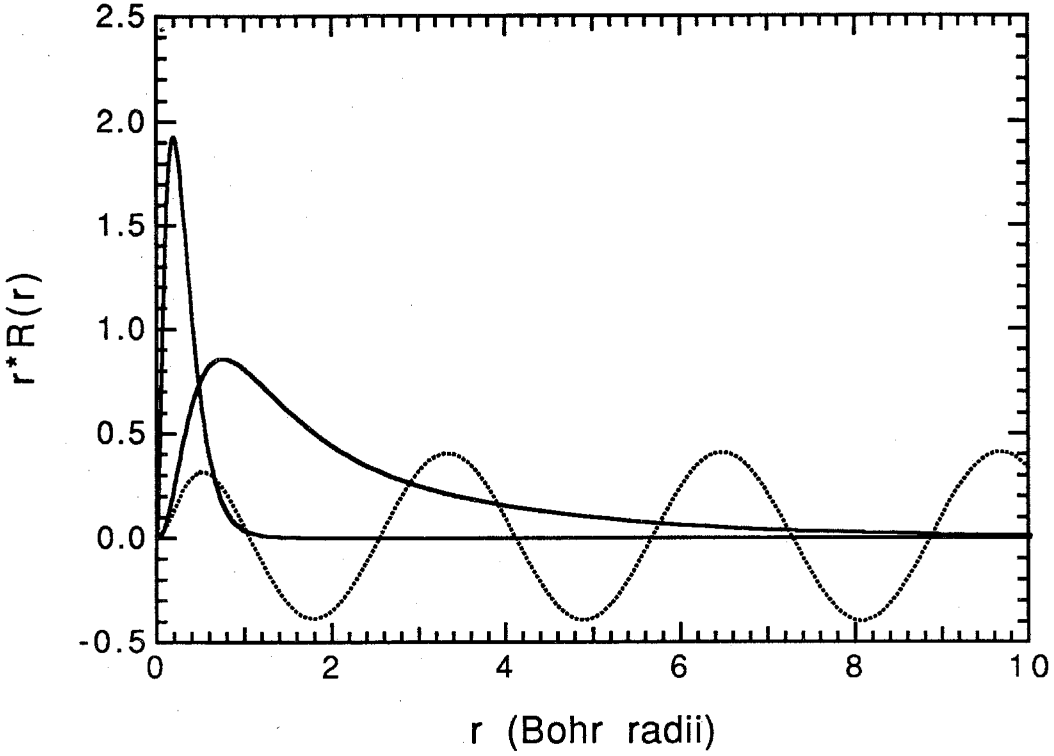

Figure A2.3. Atomic wave functions for chromium.

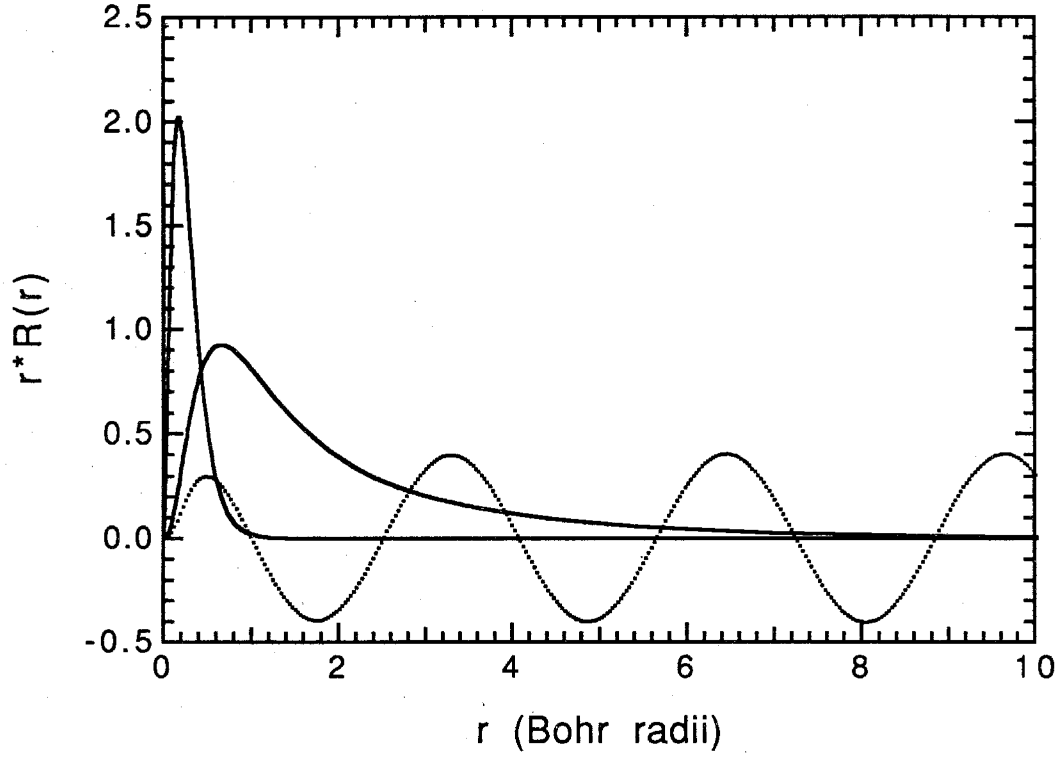

Figure A2.4. Atomic wave functions for iron.

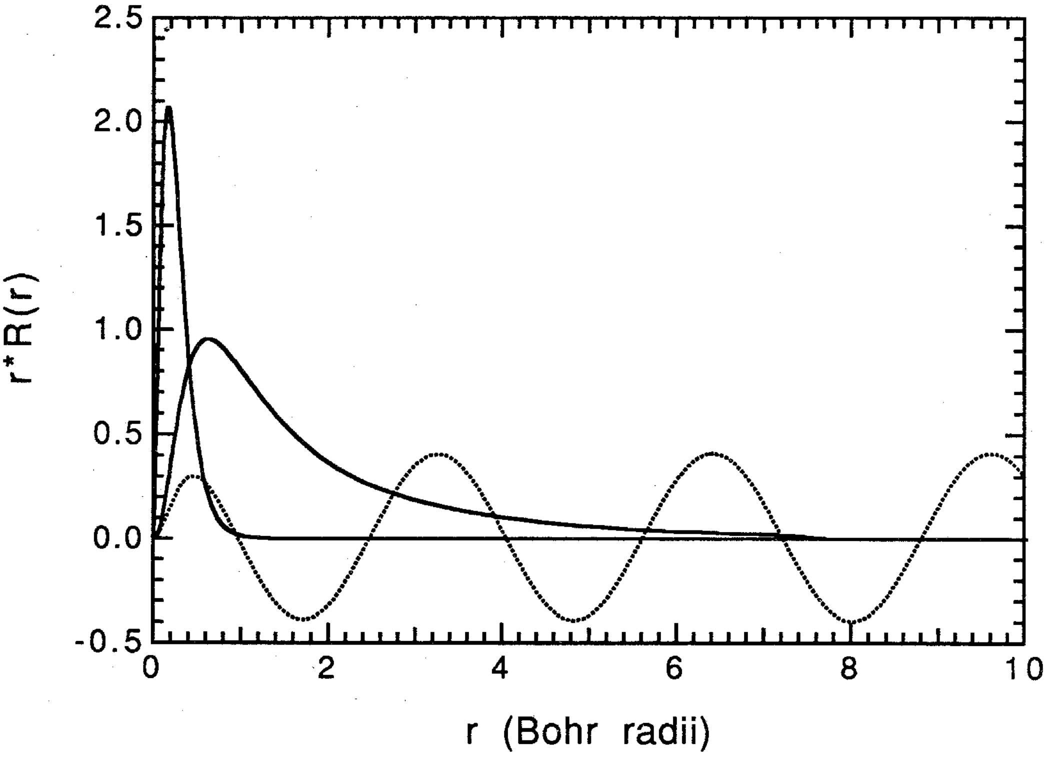

Figure A2.5. Atomic wave functions for cobalt.

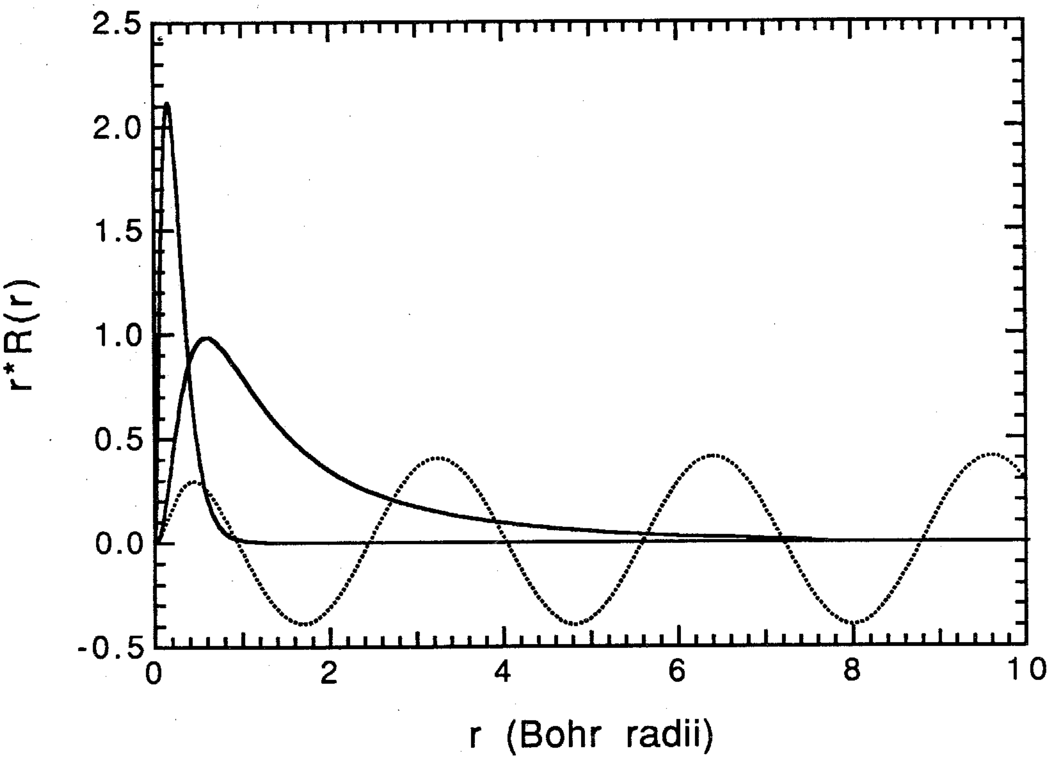

Figure A2.6. Atomic wave functions for nickel.

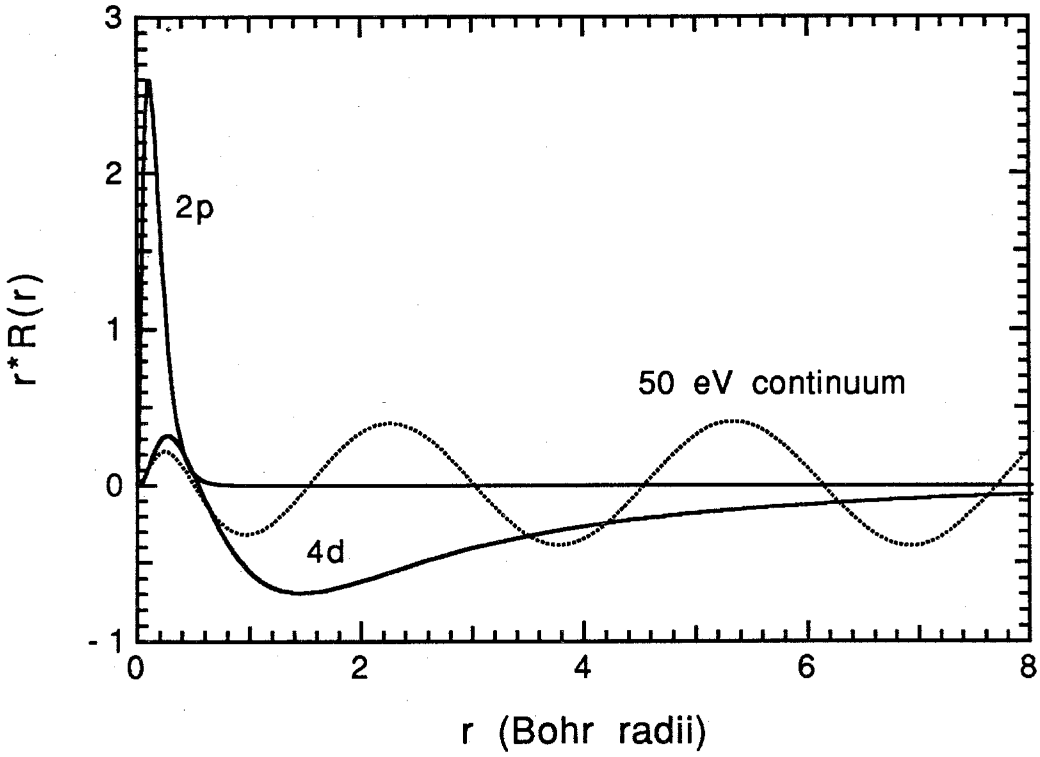

Figure A2.7. Atomic wave functions for zirconium.

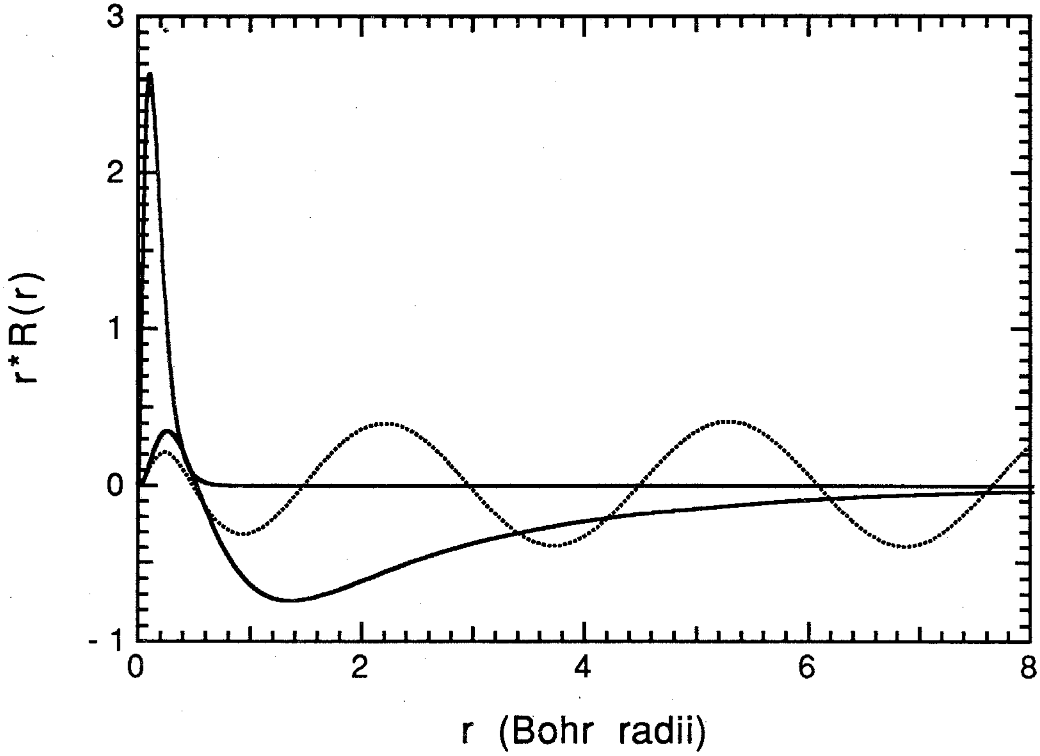

Figure A2.8. Atomic wave functions for niobium.

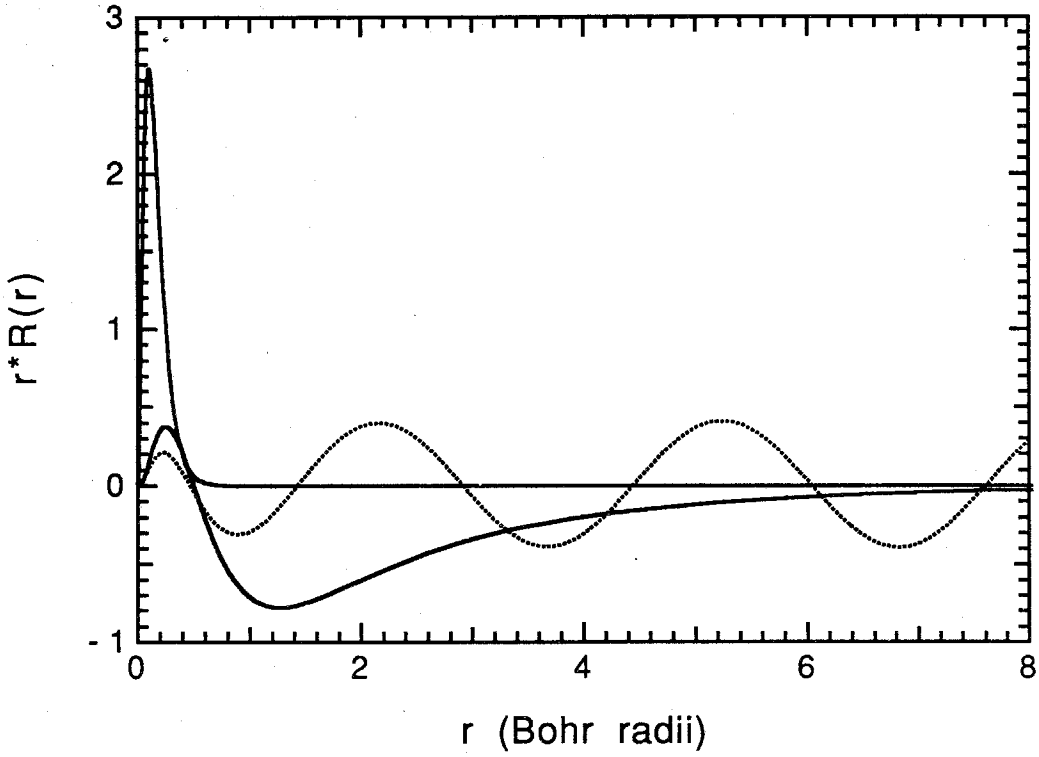

Figure A2.9. Atomic wave functions for molybdenum.

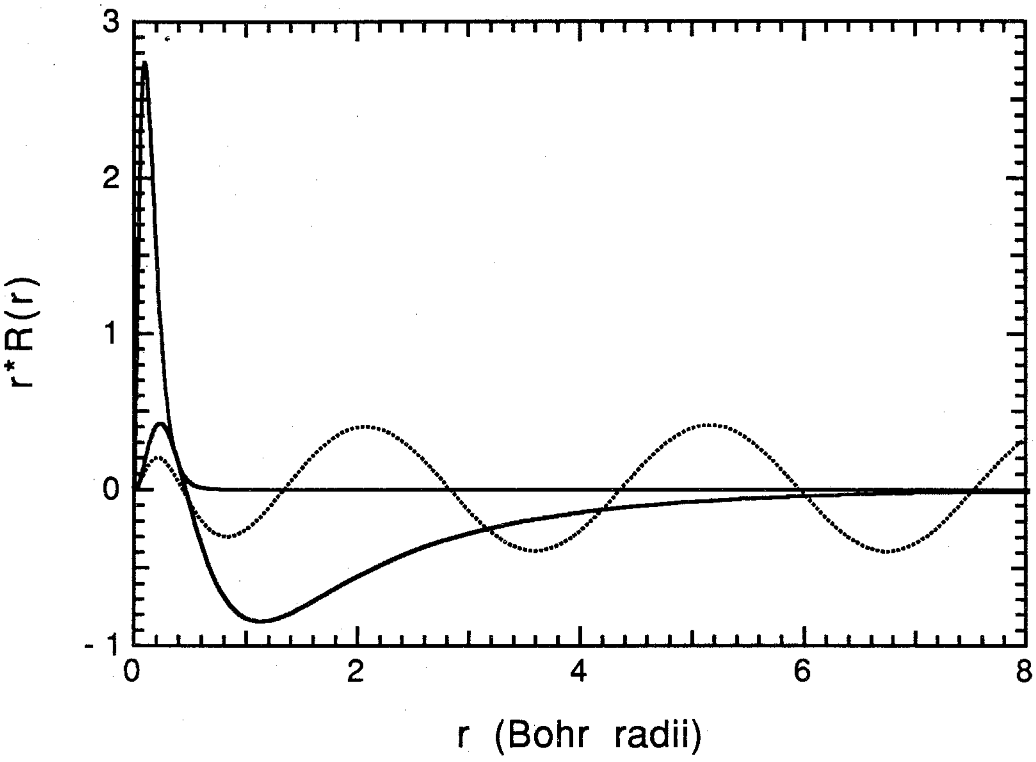

Figure A2.10. Atomic wave functions for ruthenium.

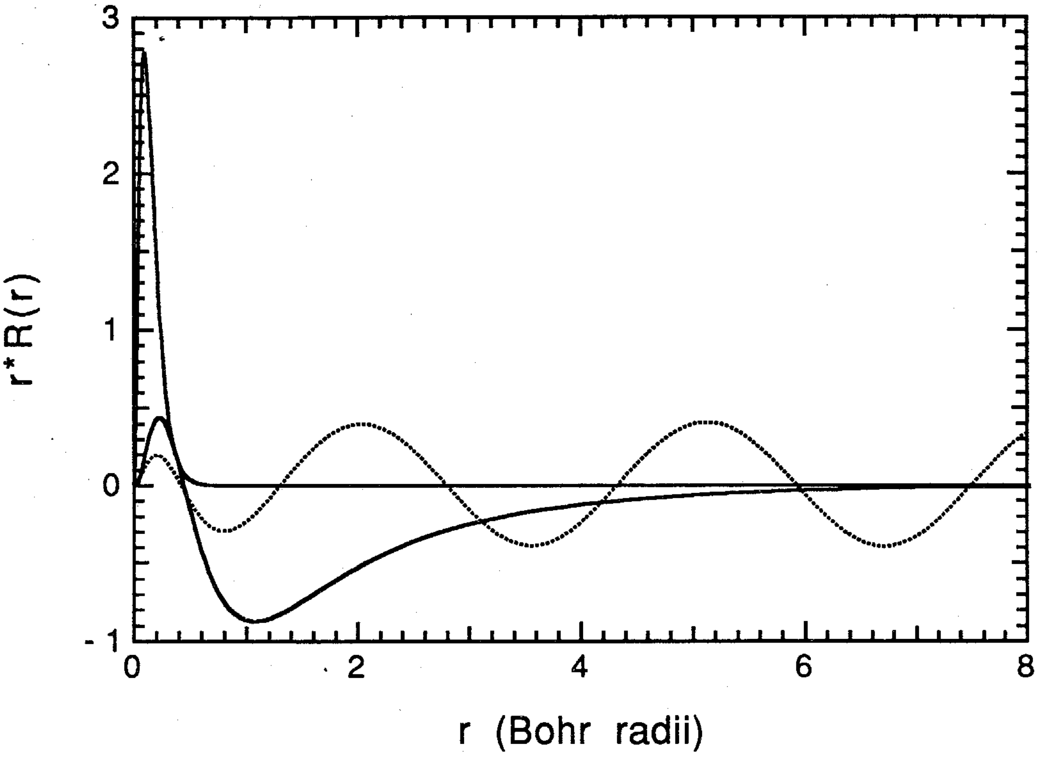

Figure A2.11. Atomic wave functions for rhodium.

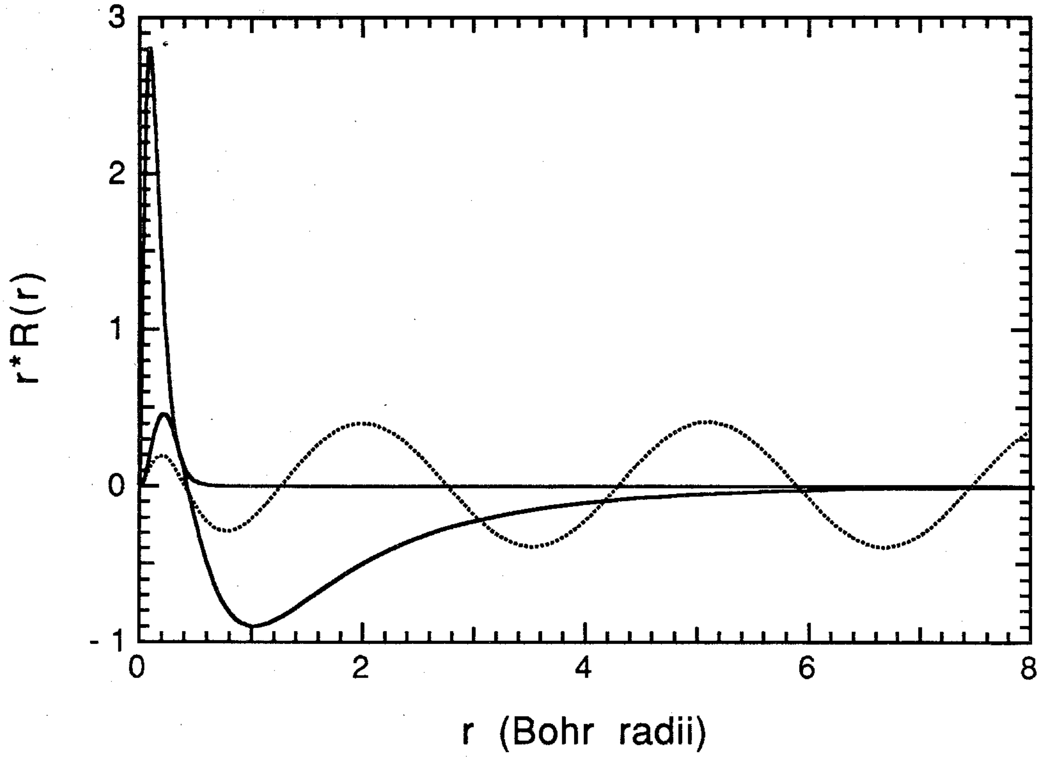

Figure A2.12. Atomic wave functions for palladium.

```
      PROGRAM MAIN
C     THIS PRGRAM READS A SELF CONSISTENT POTENTIAL AND A CORE WAVE
C     FUNCTION OBTAINED FROM A HARTREE SLATER CALCULATION AND
C     CALCULATES A CONTINUUM WAVE FUNCTION AND ITS DIPOLE INTEGRAL WITH
THE CORE
C     WAVE FUNCTION.  THE INPUT FILE IS AS FOLLOWS:
C     LINE 1:  TITLE
C     LINE 2:  Z,R1,H1,NG (EXPONENTIAL GRID PARAMETERS)
C     LINE 3:  ENERGY, ANG MOM NUMBER, DESIRED PRECISION (CONTINUUM FUNC)
C     LINE 4+  POTENTIAL ON EXP GRID
C           CORE HEADING, ANG MOM #, OCCUPATION #, ENERGY
C           CORE WAVE FUNC ON EXP GRID
C     THE RADIAL GRID IS GIVEN BY R=R1*EXP((N-1)*H1).   NOTE THAT THE
C     POTENTIAL IS GIVEN IN TABULAR FORMAT 8 COLUMNS WIDE AND IS
C     THE MODIFIED HARTREE-SLATER POTENTIAL IS GIVEN AS R*V(R)/2.
C
C
      REAL*4 R(400),VR(400),IA(400),V2R(400),YCOR(400)
      REAL*8 RLIN(50000),VRLIN(50000),YR(50000),YY(50000),F(50000)
      REAL*8 Y2R(50000),YCORN(50000),Y2COR(400),PROD,DIP,ZZ,AA,BB,CC
      REAL*4 HH,WAVL,MAX,H12,H56,MAXDIF,DIFF,E,EV,Z,R1,H1,QN1,EBI
      INTEGER L,NG,ROWS,NUM,NMAX,L1,M
      CHARACTER TAB
      CHARACTER*10 TITLE
      CHARACTER*6 LAB1
C
      TAB=CHAR(9)
C
C     READ TITLE
      READ(1,15)TITLE
   15 FORMAT(A10)
C     READ ATOM NUM, R1 AND H1 GRID PARAMS,# GRID POINTS
      READ(1,17)Z,R1,H1,NG
   17 FORMAT(F12.2,2F12.6,I10)
C     READ CONTINUUM ENERGY, ANG MOM #, AND DESIRED PRECISION
      READ(1,20)EV,L
   20 FORMAT(F9.4,I5)
      E=EV/13.6058
C
C     INITIALIZE YY ARRAY TO ZERO
      DO 73 I=1,50000
      YY(I)=0.0
   73 CONTINUE
C
C     READ INPUT POTENTIAL ON RADIAL LOG GRID
      ROWS=NG/8
      DO 300 J=1,ROWS
      READ(1,100) (IA(I), I=1,8)
  100 FORMAT(8E14.7)
```

```
      DO 200 I=1,8
      N=8*(J-1)+I
      R(N)=R1*EXP((N-1)*H1)
      VR(N)=-IA(I)*2/R(N)
 200  CONTINUE
 300  CONTINUE
C
C   READ CORE WAVE FUNCTION HEADING AND THEN WAVE FUNCTION
      READ(1,302)LAB1,L1,QN1,EBI
 302  FORMAT(A6,I5,2F10.2)
      READ(1,100)(YCOR(N),N=1,NG)
C
C   DO SPLINE FIT TO INPUT POTENTIAL
      CALL SPLINE(R,VR,NG,1.E31,1.E31,V2R)
C
C   PROVIDE PARAMETERS FOR INITIAL LINEAR GRID
      HH=0.002
      RMAX=R1*EXP((NG-1)*H1)
   2  NMAX=INT(RMAX/HH)
C
C   EVALUATE POTENTIAL ON LINEAR GRID USING SPLINT SUBROUTINE
      DO 350 I=2,NMAX
      X=HH*(I-1)
      CALL SPLINT(R,VR,V2R,NG,X,Y)
      VRLIN(I)=Y
 350  CONTINUE
C
C   EVALUATE WAVE FUNCTION BY NUMEROV METHOD
C
      H12=HH*HH/12
      H56=HH*HH*5/6
C   PROVIDE STARTING YR VALUES, CAN'T USE R(1)=0 GRID POINT BECAUSE
C   F(1) IS INFINITE, USE YR VALUES FROM SERIES SOLUTION FOR SMALL R
      ZZ=IA(1)
      AA=-ZZ/(L+1)
      BB=(ZZ*ZZ/(L+1)-0.5*E)/(2*L+3)
      CC=(ZZ*E*(3*L+4)-2*ZZ*ZZ*ZZ)/(6*(L+1)*(L+2)*(2*L+3))
      YR(1)=0.0
      YR(2)=(HH**(L+1))*(1+AA*HH+BB*HH**2+CC*HH**3)
      YR(3)=((2*HH)**(L+1))*(1+AA*2*HH+BB*(2*HH)**2+CC*(2*HH)**3)
      RLIN(1)=0.0
      DO 410 N=2,NMAX
      RLIN(N)=(N-1)*HH
      F(N)=-(E-VRLIN(N)-(L*(L+1))/(RLIN(N)*RLIN(N)))
 410  CONTINUE
      DO 450 N=3,NMAX-1
      A=(YR(N)*(2+H56*F(N)))-(YR(N-1)*(1-H12*F(N-1)))
      YR(N+1)=A/(1-H12*F(N+1))
 450  CONTINUE
```

```
C
C   NORMALIZE WAVE FUNCTION OVER LAST CYCLE TO AN AMPLITUDE OF
C   1/((PI^.5)*(E^.25)) WHERE E IS IN RYDBERGS
C   NOTE:  ONE CYCLE OF PLANE WAVE = 2*PI = ROOT(ENERGY)*WAVE LENGTH
C   FIND NUMBER OF POINTS TO SAMPLE ONE WAVE LENGTH
     WAVL=2*3.1416/SQRT(E)
     NUM=INT(WAVL/HH)
C   FIND MAX OF LAST "NUM" SEGMENTS AND NORMALIZE
     MAX=YR(NMAX-NUM)
     DO 470 I=NMAX-NUM+1,NMAX
     IF (YR(I).GT.MAX) THEN
      MAX=YR(I)
     ENDIF
 470 CONTINUE
     DO 475 N=1,NMAX
     YR(N)=YR(N)/(MAX*SQRT(3.1416)*SQRT(SQRT(E)))
 475 CONTINUE
C
C   CALCULATE NEW WAVEFUNCTION FOR HH=0.001 AND COMPARE TO PREVIOUS
C   WAVE FUNCTION TO ESTIMATE PRECISION
C
     IF (HH.EQ.0.001) THEN
       GOTO 482
     ENDIF
     DO 480 I=1,NMAX
     YY(I)=YR(I)
 480 CONTINUE
     HH=0.001
     GOTO 2
C
 482 MAXDIF=0.0
     DO 490 I=1,INT(NMAX/4)
     DIFF=YR(2*I-1)-YY(I)
     IF (DIFF*DIFF.GT.MAXDIF*MAXDIF) THEN
      MAXDIF=DIFF
     ENDIF
 490 CONTINUE
C
 486  FORMAT(E14.7,A1,E14.7)
C
C   CALCULATE DIPOLE INTEGRAL USING TRAPEZOIDAL RULE
C
 491 DIP=0.0
     CALL SPLINE(R,YCOR,NG,1.E31,1.E31,Y2COR)
     DO 522 I=2,NMAX
     X=HH*(I-1)
     CALL SPLINT(R,YCOR,Y2COR,NG,X,Y)
     YCORN(I)=Y
 522 CONTINUE
```

```
C
      DO 524 N=1,NMAX-1
      PROD=RLIN(N+1)*YCORN(N+1)*YR(N+1)+RLIN(N)*YCORN(N)*YR(N)
      DIP=DIP+PROD*HH/2
 524  CONTINUE
C
C    WRITE THE WAVE FUNCTION Y(R) IN TAB FORMAT LINEAR DISPLAY GRID
C    WITH SPACING 0.04
      M=INT(0.04/HH)
      WRITE(9,486)HH,TAB,MAXDIF
      WRITE(9,486)DIP,TAB,DIP
      WRITE(9,15)TITLE
      WRITE(9,20)EV,L
      DO 492 N=1,INT(NMAX/M)
      I=(N)*M+1
      WRITE (9,486)RLIN(I),TAB,YR(I)
 492  CONTINUE
C
C
      STOP
      END
C
C
C    SPLINE SUBROUTINE FROM NUMERICAL RECIPES
C
      SUBROUTINE SPLINE(X,Y,N,YP1,YPN,Y2)
      PARAMETER (MMAX=50000)
      DIMENSION X(N),Y(N),Y2(N),U(MMAX)
      IF (YP1.GT..99E30) THEN
       Y2(1)=0.
       U(1)=0.
      ELSE
       Y2(1)=-0.5
       U(1)=(3./(X(2)-X(1)))*((Y(2)-Y(1))/(X(2)-X(1))-YP1)
      ENDIF
      DO 11 I=2,N-1
       SIG=(X(I)-X(I-1))/(X(I+1)-X(I-1))
       P=SIG*Y2(I-1)+2.
       Y2(I)=(SIG-1.)/P
       U(I)=(6.*((Y(I+1)-Y(I))/(X(I+1)-X(I))-(Y(I)-Y(I-1))
     *    /(X(I)-X(I-1)))/(X(I+1)-X(I-1))-SIG*U(I-1))/P
  11  CONTINUE
      IF (YPN.GT..99E30) THEN
       QN=0.
       UN=0.
      ELSE
       QN=0.5
       UN=(3./(X(N)-X(N-1)))*(YPN-(Y(N)-Y(N-1))/(X(N)-X(N-1)))
      ENDIF
```

```
      Y2(N)=(UN-QN*U(N-1))/(QN*Y2(N-1)+1.)
      DO 12 K=N-1,1,-1
       Y2(K)=Y2(K)*Y2(K+1)+U(K)
 12   CONTINUE
      RETURN
      END
C
C     SPLINT SUBROUTINE FROM NUMERICAL RECIPES
C
      SUBROUTINE SPLINT(XA,YA,Y2A,N,X,Y)
      DIMENSION XA(N),YA(N),Y2A(N)
      KLO=1
      KHI=N
  1   IF (KHI-KLO.GT.1) THEN
       K=(KHI+KLO)/2
       IF(XA(K).GT.X)THEN
        KHI=K
       ELSE
        KLO=K
       ENDIF
      GOTO 1
      ENDIF
      H=XA(KHI)-XA(KLO)
      IF (H.EQ.0.) PAUSE 'Bad XA input.'
      A=(XA(KHI)-X)/H
      B=(X-XA(KLO))/H
      Y=A*YA(KLO)+B*YA(KHI)+
     *     ((A**3-A)*Y2A(KLO)+(B**3-B)*Y2A(KHI))*(H**2)/6.
      RETURN
      END
```

References for Appendix 2

Hartree, D. R., The Calculation of Atomic Structures, John Wiley & Sons, New York (1957).

Herman, F. and Skillman, S., Atomic Structure Calculations, Prentice Hall, Englewood Cliffs (1963).